Wind Turbine Emulation Based on the Accurate Control of Servomotors

Mark Dales

A thesis submitted to the University of Huddersfield in partial fulfilment of the requirements for the degree of Doctor of Philosophy

June 2018

Abstract

The objective of this work is the creation of a novel Wind Turbine Emulation (WTE) technique to support the needs of a new generation of multi-bladed vertical-axis wind turbine (VAWT) designs aimed at the urban environment. The scheme, presented in this thesis, uses Computational Fluid Dynamics (CFD) data, from the analysis of such devices, as the basis of its operation.

CFD methods are used for the analysis of wind turbine performance but CFD models do not incorporate physical system inertial response or provide a physical test bed. WTE must, therefore, continue to play a role in the support of wind turbine design, research and development. Ongoing work, on enhancing wind turbine designs for use in the urban environment, is leading towards the use of complex, drag-based, multi-bladed, vertical-axis devices to deal with the problems inherent in the urban situation. Current WTE systems are found to be incapable of modelling the complex torque output of these devices adequately, since they are based on the use of a steady-state model modulated by an approximating analytical function. The WTE technique developed in this thesis uses CFD profiles mapped to a two-dimensional array to generate torque coefficient values in real time. Initially a standard inertia-compensation scheme, based on an acceleration observer, is used, but testing shows that this method is inadequate due to the requirement for a low-pass filter in the feedback path. To achieve the performance necessary to accurately model the output from a multi-bladed VAWT, a novel inertia-compensation scheme is designed and implemented. The improved technique eliminates the filter induced performance degradation by dynamically manipulating z-plane pole positions based on real-time observation of system stiffness and incorporating an adaptive 'lag-lead' pre-filter at the input to the torque compensation control loop. System behaviour is approximated by an s-plane model and pole manipulation is achieved by dynamic modulation of the wind turbine (WT) moment of inertia quantity used in the feedback path.

Tests show that the novel inertia compensation scheme meets the requirements for accurate emulation of VAWT performance. Mean torque and power output tests confirm that, for all profiles used, the output accurately reflects those predicted by the original CFD analyses. Time and frequency domain analyses of generator load current signals confirm that the technique facilitates the analysis of generator output signals on a WTE test bed for the development of fault diagnosis and Condition Based Maintenence (CBM) strategies.

Acknowledgements

I wish to thank the many friends, colleagues and relatives who have provided support and encouragement during this endeavour, in particular:

Dr. Peter Mather, my academic supervisor, for advice, encouragement and support throughout the entire project.

Dr. Violeta Holmes, my line manager and colleague, for encouragement and advice regarding the LabVIEW environment.

Prof. Ian Glover, Head of Department, for support and encouragement.

Dr. Kyoo-Seon Park, for the provision of the wind turbine data necessary to complete this project.

Dennis Town, Technical Support Manager, for his considerable assistance and expertise in the creation of the test bed.

David Bray, Electrical Technician Team Leader, and Martin Webster, Senior Electronics Technician, for support with electronic aspects of the project.

Richard Midlam, Senior Power Electronics Technician, for his interest and willingness to share his extensive practical knowledge of industrial drive systems.

Anver Dadhiwala, Senior IT Technician, for his invaluable help in setting up the Real-Time LabVIEW platform.

Karen Dales, my wife, for her unfailing support, understanding, patience and encouragement.

Copyright Statement

i. The author of this thesis (including any appendices and/or schedules to this thesis) owns any copyright in it (the 'Copyright') and he has given The University of Huddersfield the right to use such Copyright for any administrative, promotional, educational and/or teaching purposes.

ii. Copies of this thesis, either in full or in extracts, may be made only in accordance with the rules of the University Library. Details of these regulations may be obtained from the Librarian. This page must form part of any such copies made.

iii. The ownership of any patents, designs trade marks and any or all other intellectual property rights except for the Copyright (the 'Intellectal Property Rights') and any reproductions of copyright works, for example graphs and tables ('Reproductions'), which may be described in the thesis, may not be owned by the author and may be owned by third parties. Such Intellectual Property Rights and Reproductions cannot be and must not be made available for use without the prior written permission of the owner(s) of the relevant Property Rights and/or Reproductions.

Glossary of Terms and Symbols

Term	Definition
ADC	Analogue to Digital Converter
ADMD	After Diversity Maximum Demand
ALF	Annual Load Factor
CBM	Condition Based Maintenance
CFD	Computational Fluid Dynamics
DAC	Digital to Analogue Converter
DAQ	Data AcQuisition device
DER	Distributed Energy Resource
DMF	Deviation Mitigation Filter
EMF	Electro Motive Force
EV	Electric Vehicle
FBSOA	Forward Biased Safe Operating Area
FIT	Feed In Tariff
FSM	Finite State Machine
HAWT	Horizontal Axis Wind Turbine
HV	High Voltage

Term	Definition
LCD	Liquid Crystal Display
LPF	Low Pass Filter
LV	Low Voltage
MOSFET	Metal Oxide Field Effect Transistor
PC	Personal Computer
PV	PhotoVoltaic
RT	Real Time
RTOS	Real Time Operating System
SCADA	Supervisory Control and Data Acquisition
TDMS	Technical Data Management Streaming
TSR	Tip Speed Ratio (Symbol λ)
UI	User Interface
VAWT	Vertical Axis Wind Turbine
WECS	Wind Energy Conversion System
WT	Wind Turbine
WTE	Wind Turbine Emulation

Symbol	Definition
W	Energy
A	WT aperture
A	Amplifier gain
ρ	Air density
R	WT Rotor radius
θ	WT rotor angular position
ω	WT angular velocity
α	Terrain Constant
$\dot{\omega}$, α	WT angular acceleration
V_w	Wind velocity
n	Gearbox ratio
J_{wt}	WT moment of inertia
J'_{wt}	WT moment of inertia referred to gearbox output
J_g	Generator moment of inertia
J_{sm}	Servomotor moment of inertia
J_T	WT system total moment of inertia
J'_T	WT system total moment of inertia referred to gearbox output
J_S	WTE system total moment of inertia
α, β	Digital filter coefficients
T, Δt	Digital system sample time delay
τ_f	Filter time constant

Symbol	Definition
V_g	Generator voltage
V_L	Load voltage
I_g	Generator current
I_L	Load current
C_p	Performance (Power) coefficient
C_t	Torque coefficient
λ	Tip Speed Ratio (TSR)
σ	WT rotor solidity
T_{ad}	Aerodynamic torque
T'_{ad}	Aerodynamic torque referred to gearbox output
T_g	Generator electromagnetic torque
T'_g	Generator electromagnetic torque referred to gearbox input
T_{comp}	Compensating torque
T_{sm}	Servomotor torque
T_{sp}	Setpoint torque
T_{rotor}	WT rotor torque
P_{rotor}	WT rotor power
P_w	Power in the wind
k	System loading stiffness
k_{wind}	Generator windage constant
K_m	Generator machine constant

Symbol	Definition
T_j	Junction temperature
R_{th}	Thermal resistance
E	Generator EMF
I_a	Armature current
I_{ds}	Drain-Source current
V_a	Armature voltage
V_{gc}	Gate-Common voltage
V_{gs}	Gate-Source voltage
z	WT blade count
ψ	Rotor position w.r.t tower

Contents

List of Figures

List of Tables

Chapter 1

Introduction

1.1 Background

Recent rapid developments in Wind Energy Conversion Systems (WECS) have been driven by concerns that pollution from fossil fuel based CO_2, described as a greenhouse gas, is leading to damaging climate change. In the UK, measures to combat this threat are being implemented under the Climate Change Act (2008) [1] which was passed to meet the requirements of the European Union (EU) 20:20:20 initiative [2]. This has put in place targets to reduce greenhouse gas emissions across the EU by 20 % and increase energy efficiency savings by 20 % by the year 2020. Targets for each nation state differed with the overall renewable energy target for the UK required to rise from 2.25 % in 2008 to 15 % by the year 2020 [3]. All energy utilising sectors were included in this figure, however, renewable electricity generation was required to increase approximately six fold to provide 30 % from renewable sources by 2020. Progress towards the electricity generation target is currently on track with figures from the UK government's Energy Trends Report, showing that 30 % of the UK's generated electricity came from renewable sources during the third quarter of 2017 [4]. Offshore and onshore WECS contributed 5.3 % and 7.5 % respectively to UK total electricity generation.

1.2 Wind Energy Conversion Systems

In 2008, UK onshore and offshore installed wind capacities totalled 2986 MW and 588 MW respectively [5]. By the second quarter of 2017 the corresponding figures had increased to 12219 MW and 5671 MW [6]. The average rating of UK offshore and onshore wind turbines installed during 2017 was 6 MW and 2.5 MW respectively [7]. All offshore, and large onshore turbines are Horizontal Axis Wind Turbines (HAWT) with automatic blade pitch control to optimise performance at varying wind speeds. HAWTs also incorporate yaw control to maintain orientation for maximum efficacy as wind direction changes. These complex, high value assets are located in remote and often onerous environments, so monitoring via Supervisory Control and Data Acquisition (SCADA) systems is necessary. Expensive, complex instrumentation is generally employed to monitor near-real-time performance and facilitate Condition Based Maintenance (CBM) and incipient fault prediction. Offshore WTs have high 'Annual Load Factors' (ALF) which is the ratio of actual annual energy supplied by a generation scheme over a 'standard year', to that which would be produced were it to operate at its rating continuously. ALF is a key parameter when considering the economic viability of an installation and is heavily dependant on site location; typically offshore systems operate at an ALF of about 40 % and onshore at about 25 % [4]. CBM plays a key role in maintaining the ALFs of these systems and thus contributes to their economic operation.

Not all land based wind energy is derived from large, complex installations with high ALFs. The Energy Act 2008 [8] originally provided for a system of Feed In Tariffs (FITs) to encourage the deployment of a range of renewable electrical energy technologies including Small Wind (between 1.5 kW and 15 kW) and Micro Wind (less than 1.5 kW). Small Wind systems have been taken up widely by businesses and a few domestic customers.

These are typically, but not exclusively, HAWTs and such turbines can be seen throughout the UK particularly on open agricultural land where turbulence and rapidly changing wind direction are not an issue. Despite the financial incentives, the viability of such installations depends on the ALF which is contingent on site conditions. Changes to the UK FIT regime in 2012 have had the effect of encouraging larger, commercial, installations while the deployment rate for small and micro-wind systems has fallen [9]. In 2014, UK manufacturers of micro and small-wind turbines were exporting about 50 % of output [10] but there is concern that UK based production viability will be affected by the demise of the on-grid home market. Micro-wind has an established off-grid market, however, the uptake for use in on-grid urban situations, peaked in 2007 and has fallen since mainly due to the low ALF figures. A field trial, carried out in 2009, determined that the highest ALF for a micro WT deployed in UK urban areas was 7.4 % with the average being 3 % [11]. It was concluded that poor ratings were due mainly to a lack of proper surveying leading to inappropriate siting. It is also the case that the WTs deployed were not well adapted for the urban situation. To put these figures into perspective the average ALF for a well sited PhotoVoltaic (PV) installation in the UK during 2016 was 10.3 % [12]. Significant barriers to the future deployment of urban wind are, low FIT incentives and low ALFs for current turbine configurations.

1.3 The Urban Situation

It is recognised that wind energy is available in the urban environment and there are advantages to its capture. Like urban PV generation, micro-wind is a Distributed Energy Resource (DER) and such systems have the potential to become a disruptive technology within established Low-Voltage (LV) distribution networks. Existing LV networks were designed to accomodate uni-directional energy flow towards the customer. Cable cross-

sections are chosen to minimise cost while maintaining the voltage at customers' terminals within statutory limits. To achieve this, substation voltage is set close to the upper voltage limit. As DER penetration of the LV network increases, excess generation, in times of affluence, will cause unwanted voltage rises and necessitate the curtailment of local distributed generation, which is effectively 'lost'. Another target within the EU 20:20:20 initiative, however, is the reduction of CO_2 emissions associated with transport including private cars. Governments have announced future restrictions on petrol and diesel vehicles prompting major motor manufacturers to signal an intent to concentrate on hybrid and Electric Vehicles (EVs) [13]. This will lead to growing numbers of simultaneously charging EVs in urban locations and will, therefore, become an inceasingly disruptive technology. The viability of widespread EV uptake rests on the provision of infrastructure for convenient charging. Urban LV networks are designed on the principle of load diversity and it has been estimated that the After Diversity Maximum Demand (ADMD) for an average domestic dwelling can be $1.5\,kW$ based on 100 households [14]. For households with an EV, ADMD rises to $3.73\,kW$, with the EV component of that demand showing very little diversity. A Nissan Leaf car, for example, with a $30\,kWh$ battery, when charged at the lowest rate from a domestic $13\,A$ socket outlet, can draw about $2\,kW$ for up to 15 hours depending on the initial state of charge [15]. If most electricity customers have at least one such vehicle then it is certain that there will be long periods when the majority are on charge. These are not then diverse loads, and LV cable ratings will be exceeded causing local substation fuses to operate and supplies to be interrupted. In the longer term, distribution cables and joints subject to regular excessive thermal loads, have reduced life expectancy and reliability. Unless electrical energy can be sourced, and stored, close to the point of use, network reinforcement will be necessary. This is not, however, a straightforward option, as increasing the LV network rating will require extensive, and expensive, excavation of highways and private driveways. It would also be necessary to install higher

rated distribution transformers and possibly reinforce sections of the High-Voltage (HV) network. These considerations have the potential to significantly enhance the economic viability of DERs including local energy storage and micro-wind. PV is already a well established technology and clearly has a contribution to make. Energy generation from this source is restricted to daylight hours, however, and is curtailed in the winter months and in cloudy conditions. Urban wind has the potential to provide energy at these times as well as increasing total energy capture.

The deployment of WECS to capture energy in urban situations is desirable provided designs with adequate performance can be achieved. Built-up areas, however, pose particular difficulties due mainly to turbulent air flows that are prone to rapid and frequent direction changes caused by adjacent structures and ground topography [16]. HAWT yawing mechanisms do not always react quickly enough to maintain optimum orientation and, under high wind conditions, the integrity of turbine mountings, and the resilience of structures to which they are attached, is also an issue. These considerations have led to renewed interest in Vertical Axis Wind Turbine (VAWT) utilisation in the urban environment [17]. Recent VAWT designs, intended to increase performance in the urban situation, have high blade counts and often incorporate static air guidance systems. Such designs have complex aerodynamic torque characteristics that cannot be modelled adequately using analytical functions. Multi-bladed VAWTs are also more susceptible to blade faults [18]. Furthermore, it is pointed out, that to incorporate CBM into urban VAWT-generator designs, it is necessary to model accurately the complex aerodynamic driving torque under all normal and faulty conditions. Computational Fluid Dynamics (CFD) techniques are now routinely used for such modelling and examples can be seen in the literature [19][20]. CFD techniques, for use with VAWTs, are constantly being refined and improved by the comparison of analyses with physical experimental results [21][22][23]. CFD analyses, therefore, pro-

vide a sound basis for novel WT design and the analysis of existing systems.

1.4 Motivation

CBM is used to ensure that the economic viability of a WT is maintained by maximising its ALF. To support CBM, based on the analysis of generator output signals affected by aerodynamic torque 'fault signatures', for example, CFD models are not sufficient in themselves. Fault detection algorithms rely on accurate spectral analyses, so models must account for the mechanical system frequency response. CFD methods provide input, rather than output rotor torque information, because the inertial response of turbines to torque fluctuations is not simulated. Wind Turbine Emulation (WTE) is an established technology that addresses this issue and is used to assist with the design and development of WT technology. WTE systems physically simulate the predicted behaviour of wind turbines on a test bed and typically incorporate inertial behaviour. Such systems have been applied to HAWT and VAWT designs, with the simplest emulators using a mean, or steady state, torque model. Dynamic aerodynamic torque models, based on approximating functions, are often used with HAWTs but not with VAWTs. To accurately model the complex aerodynamic behaviour of high blade count VAWTs CFD derived models are necessary.

The deployment of large and medium WECS for electricity generation is now well established with considerable research supporting its continued operations, maintenance and development. Urban wind power, however, is not widely installed because current micro WT designs are not optimised for the urban situation and are currently unlikely to give an adequate return on investment. Researchers continue to work on enhancing designs so that economic viability may be achieved. The need to extract energy within the urban

environment to meet growth in EV use, however, will change the point at which urban wind becomes feasible. The future viability of urban wind presents domestic and export market opportunities for manufacturers. Furthermore, urban wind design enhancements will improve the performance of similar sized off-grid WECS increasing market opportunities there. Continued research into the design and deployment of small and micro-wind systems for the urban environment is, therefore, an important endeavour. To facilitate the transition from design to realisation, research activities in the following areas are needed:

- The rapid effective modelling and testing of new turbine designs.
- The development of CBM and reporting based automated fault diagnosis. (Including aerodynamic, mechanical and electrical conditions.)
- The optimum specification and selection of turbine-generator combinations for their intended situations. (Based on CFD models for; wind speed distribution, topography and the effects of adjacent structures.)

WTE is a valuable tool that can provide the means to achieve these tasks even before a physical system has been built. The use of CFD models as the basis for emulating a particular device can also take into account the aerodynamic environment in which it is situated [24][25][26][27]. Once a device has been realised, wind tunnel testing may also be used for verification but there may be additional difficulties and costs associated with access and scheduling delays. WTE reduces the amount of testing that needs to be carried out in a wind tunnel.

To complement this area of work it is intended to research and design a Wind Turbine Emulation (WTE) system capable of reproducing the complex torque output characteristics of multi-bladed VAWTs intended for urban use. Precise, closed-loop control of motor

output torque based on angular position, angular velocity and the emulated wind velocity is required. This is most easily achieved by using a servomotor and drive system equipped with a high resolution encoder. For accessibility, it is intended to develop the system using only industry standard hardware and tools. It is proposed that WTE control models will be derived directly from CFD analyses. The ability to move rapidly from CFD model to a physical test bed will facilitate hardware optimisation and diagnostic development work while reducing wind tunnel use. No instances of WTE systems, based on the use of CFD data, have been found in the literature. The implementation of a such a system would, therefore, be a contribution to knowledge. The detailed research aim for this thesis, together with a set of associated objectives, is developed in the next chapter following a review of the relevant technical literature.

1.5 Thesis Organisation

Chapter One

This chapter explains the motivation for research into the enhancement of WTE techniques intended to ensure a continuing ability to support the design of a new generation of complex VAWT designs for the urban environment. This is necessary because current methods are inadequate. The work is discussed in the context of the general contribution that WECS are making to international efforts intended to deal with CO_2 induced climate change. The reduction of costly and disruptive LV system reinforcement, associated with the proliferation of EVs, by use of urban wind is also reviewed. Finally, the creation of a novel, CFD based, WTE method is proposed to achieve the enhanced performance required.

Chapter Two

This chapter reviews relevant literature used to obtain the technical background informa-

tion required for research into the intended enhancement of WTE techniques for use with urban VAWTs. A review of relevant principles of WECS, CBM and current WTE techniques is carried out setting the work in context and highlighting areas that have not yet been investigated and where a contribution to knowledge may be made. Finally, a detailed research aim, based on the areas identified, is set out together with the objectives required to achieve that aim.

Chapter Three

This chapter deals with the requirements analysis, detailed design and implementation of a novel WTE system using CFD analyses as the basis for deriving real-time torque output control. The use of CFD data as a means to generate real-time torque control for WTE is sucessfully achieved, however, problems are identified in the initial design. Frequency response tests, set out in Chapter Five, identify shortcomings in performance related to inertia compensation. The problem is analysed and dealt with in Chapter Four.

Chapter Four

An analysis of the performance shortcomings in the initial WTE system design is carried out and the cause is identified. A novel enhancement to the inertia compensation scheme is developed and implemented. Retesting, described in Chapter Five, shows that the modified inertia compensation scheme eliminates the performance problem.

Chapter Five

This chapter covers all the assessments carried out to confirm the ability of the system to emulate accurately, outputs for healthy and faulted VAWTs of differing physical sizes. The tests cover four main areas. Firstly, the system frequency response for the initial design is assessed and found to be inadequate. Secondly, frequency response tests are repeated

on a modified design incorporating a novel inertia compensation scheme. Thirdly, having achieved the specified frequency response, the ability to accurately generate predicted mean torque and power is tested. Finally, generator output current signals are used to assess the dynamic behaviour of the system when simulating healthy and faulted WT rotor behaviour. Test results are set out, analysed and discussed.

Chapter Six

This chapter begins by drawing conclusions about the extent to which the work carried out in this thesis has met the original research aim and objectives. A summary of the work achieved is then provided followed by a discussion of the contributions to knowledge that have been made. Finally, limitations of the work are identified and suggestions for further research in the field are set out.

Chapter 2

Literature Review

2.1 Introduction

This chapter is divided into four main sections. The first deals with the physics of energy extraction from moving air and goes on to discuss the differing principles of operation and characteristics of the various devices currently used for this purpose. The second section discusses the use, application, principles of operation and current limitations of WTE systems. The third section discusses incipient fault detection in WECS in general and considers the applicability of this to small scale urban WTs. The final section identifies the gaps in knowledge where a contribution can be made and sets out a research aim and a set of objectives to meet that aim.

2.2 Wind Turbine Technology

2.2.1 Wind Energy Conversion

The kinetic energy associated with a homogenous air mass, moving uniformly in one dimension, is given by:

$$W = \frac{1}{2}\,\rho\, V_{air}\, v^2 \tag{2.1}$$

where:

W = Kinetic Energy (Joules), ρ = Air Density (kgm^{-3}), V_{air} = Volume of air mass (m^3), and v = Air Velocity (ms^{-1}).

If the air volume (V_{air}) passes through an aperture of area $A\,m^2$ aligned normally to the direction of flow then:

$$\frac{dV_{air}}{dt} = A\,v \tag{2.2}$$

$$\Rightarrow \quad \frac{dW}{dt} = P_w = \frac{1}{2}\,\rho\,A\,v^3 \tag{2.3}$$

Equation 2.3 thus indicates the available power in the wind (P_w). The ratio of power extracted by a HAWT rotor (P_{rotor}) to the available power in the airstream gives an indication of WT performance and is known as the power (or performance) coefficient (C_p). See (2.4):

$$C_p = \frac{P_{rotor}}{\frac{1}{2}\,\rho\,A\,v^3} \tag{2.4}$$

There is a theoretical upper limit to the value of C_p which is known as the 'Betz Limit' in recognition of analysis carried out by Albert Betz in 1926 [28]. Accessible explanations of this work are set out in [29] and [30]. The Betz theorem is based on conservation of linear momentum theory and assumes that there is steady state flow of an incompressible, homogenous fluid with no frictional drag effects. Betz discusses an ideal rotor or 'actuator disc', with an infinite number of blades, that introduces a pressure change across its boundary. According to Betz, C_p is a function of the upstream wind velocity and the wind

velocity across the rotor aperture. The latter is influenced by the rotor configuration and angular velocity. The C_p function reaches a maximum when the wind velocity across the rotor is two-thirds that of the upstream wind velocity. This is the Betz Limit ($C_{p,max}$) and is given by:

$$C_{p,max} = \frac{16}{27} = 0.\dot{5}9\dot{2} \tag{2.5}$$

The corresponding theoretical limit to the power that may be extracted from the airstream is given by:

$$P_{max} = \frac{16}{27} \times \frac{1}{2} \rho A v^3 \tag{2.6}$$

The theoretical limit ($C_{p,max}$) is not achievable in practice as practical WTs do not have an infinite number of blades. They also have aerodynamic drag and introduce rotation into the wake air flow. It is possible, for any particular WT, to derive a characteristic power coefficient curve ($C_p(\lambda)$) that is a function of WT Tip Speed Ratio (TSR). TSR is defined by:

$$\lambda = \frac{\omega R}{v} \tag{2.7}$$

where:
λ = TSR, ω = Rotor Angular Velocity ($rad\,s^{-1}$), R = Rotor Radius (m) and, v = Upstream Wind Velocity (ms^{-1}).

The power coefficient curve, for a WT, may be derived experimentally, or analytically, at a particular wind velocity, based on a knowledge of rotor power and using (2.4) and (2.7). The utility of this parameter is that, having derived the $C_p(\lambda)$ characteristic for a particular wind velocity, it may then be used to predict performance at any other opera-

tional wind velocity [30]. This is possible because the ideal Betz power coefficient curve is a function of wind velocity ratios. The non-ideal characteristics of practical WTs means that, in reality, there is some dependance on absolute wind velocity. However, provided wind velocities remain within a WT's designed operational range the model is considered sufficiently accurate to justify the derivation of one curve only. When this is the case, (2.8) may be used to calculate rotor power output for any wind speed given the power coefficient function as follows:

$$P_{rotor} = \frac{1}{2}\rho A v^3 C_p(\lambda) \tag{2.8}$$

where:

P_{rotor} = Rotor Power Output (W), ρ = Air Density (kgm^{-3}), v = Wind Velocity (ms^{-1}), A = Turbine Aperture (m^2) and $C_P(\lambda)$ = Power Coefficient Function.

(nb. The WT power coefficient maximum indicates the optimum TSR necessary for peak power extraction.)

To calculate rotor torque (T_{rotor}) at any wind velocity, an associated torque coefficient ($C_t(\lambda)$) may also be defined:

$$C_t(\lambda) = \frac{C_p(\lambda)}{\lambda} \tag{2.9}$$

Then since $P_{rotor} = \omega\, T_{rotor}$, substituting from (2.7), into (2.8) gives:

$$T_{rotor} = \frac{1}{2}\rho A\, R\, v^2\, C_t(\lambda) \tag{2.10}$$

The Betz analysis and associated limit are generally considered to be applicable to all WT types [30]. Some studies, however, suggest that for VAWTs, the theoretical limit is higher [31][32]. A CFD simulation carried out in 2016 and presented in [33] indicates that the

theoretical limit for an ideal VAWT is approximately 6 percentage points higher than the Betz limit. It is concluded that the flat 'actuator disc' model is not applicable to VAWTs since energy transfer takes place over a curved surface. There are also differences in the wake behaviour and its interaction with downstream blades. The power coefficient curve, however, remains a function of wind velocity ratios with the same constraints on its use. The parameters (C_p and C_t), therefore, remain valid for modelling, design and analysis purposes.

2.2.2 Wind Turbine Configurations

WTs are configured as either vertical-axis or horizontal-axis machines and, within each of these categories, there are many variations particularly for VAWTs. In either configuration energy may be extracted using aerodynamic 'lift' via aerofoil blades. The HAWT and the Darrieus devices shown in Figure 2.1 use this principle. The vertical axis Savonius device, however, uses the 'drag' or reaction principle where air, striking the leading and trailing faces of the device blades, exerts differing forces leading to rotation. The blade tips, of these devices, cannot move much faster than the airstream driving them, resulting in characteristically low TSRs. They tend to be heavy and, in their original form, have low power coefficients. There are also VAWTs that utilise air deflecting stator devices with a drag based rotor.

HAWTs differ in the following ways:

- The number (z) of blades employed.
- Whether the rotor is upwind or downwind of the tower.
- The rotor aperture and axis height.

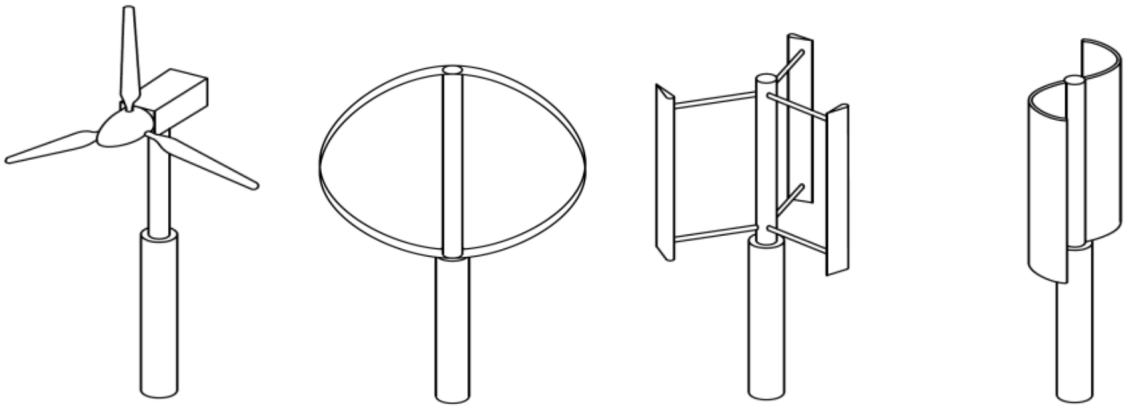

(a) HAWT (b) Darrieus VAWT (c) H-Blade Darrieus (d) Savonius VAWT

Figure 2.1: Wind Turbine Configurations [34]

Air velocity may be reduced, and energy extracted, by a slow moving horizontal axis rotor with many blades and a low TSR, or by a faster moving rotor with fewer blades and a higher TSR [29]. In the former case the torque generated will be higher and the structural forces correspondingly higher. In the latter case power is generated at lower torque with higher angular velocities and TSRs. In general better power coefficients are achieved with lower blade counts and higher TSRs [29]. Two-bladed devices are utilised, but the majority of installed devices can be seen to be three-bladed.

To maximise energy conversion, HAWTs require a yawing mechanism to ensure that the rotor aperture is always presented normally to the incoming airflow. Under these circumstances, the aerodynamic forces on the turbine blades will vary with the square of the wind velocity but will not vary greatly in direction as the blade rotates. There are, however, two main sources of torque variation as the rotor turns:

- Tower Effect.
- Wind Shear Effect.

Rotors located downwind of a supporting tower are affected by 'tower shadow'. As each

rotor blade passes behind the tower, incident airflow is blocked causing torque fluctuations in the rotor output. For a three-bladed rotor ($z = 3$), there will be three such fluctuations per revolution. Upwind rotors suffer from a similar pattern of torque fluctuation, however, the impact is less severe. For this reason upwind rotors are the normal configuration. In the upwind case a bow-wave effect occurs in which airflow ahead of the tower is retarded and flow rate is reduced in this region of the aperture. This aspect is discussed in [35] where it is noted that the closer the blade passes to the support, the greater the effect. A streamline diagram modelling the effect on normalised airflow is presented showing how the effect varies with distance from the tower. For structural reasons the leading rotor should not protrude too far ahead of the tower but for aerodynamic purposes it should not be too close. The normal compromise is to locate the blades approximately one-tower diameter ahead of the support. At this separation, the model shows that the normalised flow rate is reduced by about 10%. It can be seen that if there are z rotor blades there will be z torque oscillations per revolution. A simple graphical approximation to the torque ripple effect for a three-bladed rotor is presented and this is reproduced in Figure 2.2.

A more elaborate improvement on the 'ramp' model is set out in [36] where the torque fluctuation associated with each blade passing the tower is modelled as an inverted, limited cosine function:

$$T_{te} = -t_{ts} \cos \psi \quad \text{with} \quad -\psi_T \geq \psi \geq \psi_T \tag{2.11}$$

Where the reference angle ($\psi = 0°$) is with the blade aligned vertically downwards in front of the support and: T_{te} = Torque fluctuation due to one blade passing through the sector affected by the support; t_{ts} = An empirical coefficient; ψ_T = Half the sector angle in which the blade is influenced by the tower effect.

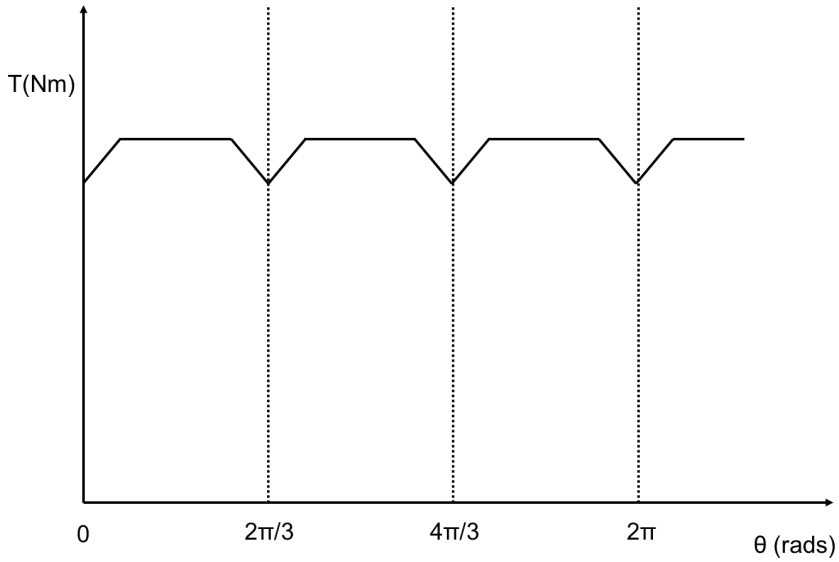

Figure 2.2: A Simple Ramp Model of Tower Shadow Effect for a Three-Blade Rotor [35]

Wind Shear is the increase in wind velocity with height above ground and this non-linear velocity gradient is affected by the roughness of the terrain. It may be modelled as a power law profile [37] as described by:

$$\frac{v_2}{v_1} = \left(\frac{h_2}{h_1}\right)^{\alpha} \tag{2.12}$$

where:

v_1 is the wind velocity at height one (h_1), v_2 is the wind velocity at height two (h_2) and α is the terrain coefficient.

Figure 2.3 shows the results of a survey carried out at a potential WT site near Morris, Minnesota, USA [37]. Average wind speeds were recorded at differing heights, at ten minute intervals, over a period of one year and used to create the profile shown. It was found that the terrain coefficient, (α) was 0.244 which is typical of this rural area.

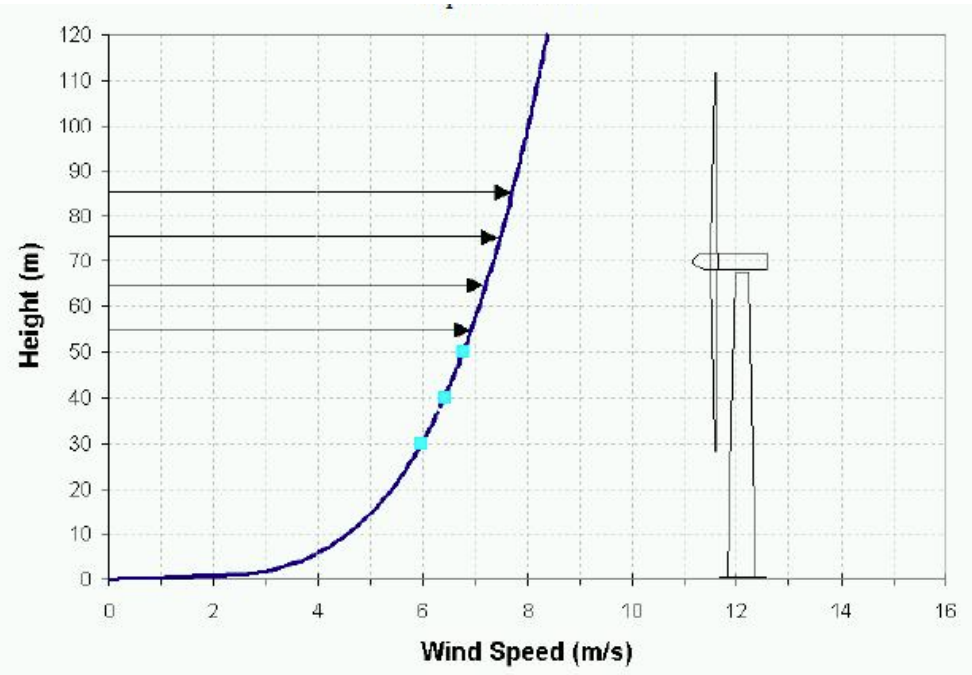

Figure 2.3: Vertical Wind Shear Profile at a Proposed WT Site in Minesota, USA [37]

It can be seen that the wind velocity encountered by each blade varies during each revolution. For tall, large aperture machines, the effect is significant. In this example, the average wind velocity varies, across the aperture, by approximately $\pm 1\, ms^{-1}$ about the hub height value of $7.2\, ms^{-1}$.

A complex mathematical model, incorporating the effects of both wind shear and tower shadow, has been derived in [38]. It is based on firstly, obtaining a complete expression for the wind field across the aperture and then determining, and summing, the effects on each of the blades as they move through the field. The model takes account of; hub height, tower radius, distance from blade centre to tower centre and the terrain coefficient. Figure 2.4 shows three plots of normalised equivalent wind velocity (w.r.t the hub height value) resulting from the use of this model. The dotted plot shows the tower shadow effect. It can be seen that it is more sophisticated than the previous models discussed, as it takes

account of the increase in air velocity on either side of the tower due to the 'bow wave' effect. This can be seen as a slight rise on either side of each bow wave 'trough'. The dashed line shows the isolated effect of wind shear which manifests as a third 'harmonic' cosine function superimposed on a slightly reduced (w.r.t. the hub height velocity) steady state value. The solid line shows the resulting overall effect.

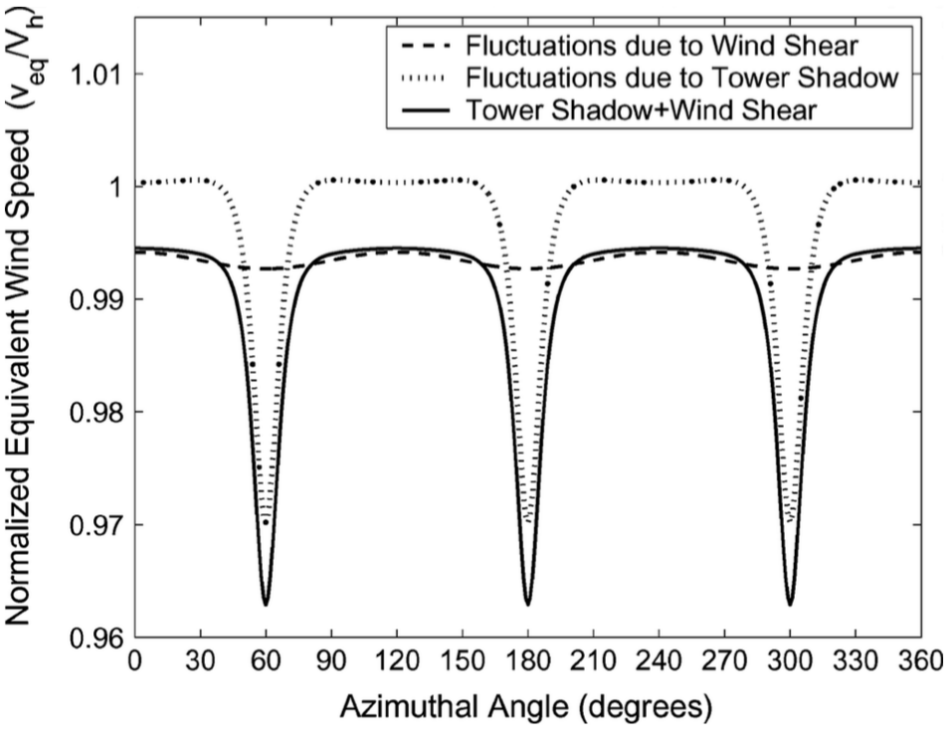

Figure 2.4: The Combined Effects of Tower Shadow and Wind Shear [38]

The overall normalised equivalent wind velocity (v_{eq}) shown in Figure 2.4 is a function of time and blade position and results from the summation of three components as follows:

$$v_{eq} = v_{eq(0)} + v_{eq(WS)} + v_{eq(TS)} \tag{2.13}$$

where:

$v_{eq(0)}$ is the reference (hub height)wind velocity, $v_{eq(WS)}$ is the variation introduced by wind shear and $v_{eq(TS)}$ is the variation introduced by tower shadow.

The following formulae can be used to calculate these components [38]:

$$v_{eq(0)} = V_H \tag{2.14}$$

$$v_{eq(WS)} = V_H \left[\frac{\alpha(\alpha-1)}{8} \left(\frac{R}{H} \right)^2 + \frac{\alpha(\alpha-1)(\alpha-2)}{60} \left(\frac{R}{H} \right)^3 \cos 3\theta \right] \tag{2.15}$$

$$v_{eq(TS)} = \frac{mV_H}{3R^2} \sum_{b=1}^{3} \left[\frac{a^2}{\sin^2 \theta_b} \ln \left(\frac{R^2 \sin^2 \theta_b}{x^2} + 1 \right) - \frac{2a^2 R^2}{R^2 \sin^2 \theta_b + x^2} \right] \tag{2.16}$$

$$\text{and:} \qquad m = \left[1 + \frac{\alpha(\alpha-1)(R^2)}{8H^2} \right] \tag{2.17}$$

where:

V_H = The hub-height wind velocity (ms^{-1}), α = the terrain constant, R = the rotor radius (m), H = the hub height (m), a = the tower radius (m), x = blade distance from tower centre (m), θ_b = azimuthal angle of blade 'b' (deg) and θ = rotor azimuthal position with respect to reference (deg).

The model may be used, with specific WT data, including the torque and power coefficients, to derive a computer based algorithm to determine quasi-steady-state torque and power outputs. Such an algorithm is easily adaptable for a wide range of HAWTs.

VAWTs have a number of features that make them more suitable for use in an urban environment than HAWTs [16]. Built up areas are characterised by frequently and rapidly

changing wind direction. HAWT yawing mechanisms are unable to react rapidly enough to optimise energy capture whereas VAWTs do not require this feature. TSRs are lower than for HAWTs resulting in less noise pollution, and therefore greater acceptability, in the urban environment [39]. They are also more suited to mounting on buildings and generators, gearboxes and cabling may be mounted more accessibly below the device [40]. Wind Shear and Tower Shadow (even on tower mounted devices) do not affect aerodynamic torque in the same way as for HAWTs. The aerodynamic torque fluctuations are, however, significantly more complex, especially in devices with a high blade count. There has been renewed interest in the adaptation of well established VAWT configurations to increase the performance of these devices within an urban environment.

VAWTs differ in the following ways:

- Whether the device is 'lift' or 'drag' based.
- The number (z) of blades employed.
- The rotor aperture and aspect ratio.
- The mounting aerodynamic environment.

Darrieus WTs utilise aerodynamic 'lift' to extract energy from the airstream. The design, patented by G Darrieus in the USA in 1931 [41], proposed two basic aerofoil configurations. These were; Troposkien, (Figure 2.1b) and 'H' type, (Figure 2.1c). Troposkien blades have structural advantages for larger apertures but have the disadvantage that reducing torque contributions occur towards the top and bottom of the aerofoils due to the reducing radii. H-rotors avoid this issue since the rotor radius is constant. The aerofoils also have a uniform chord width which offers advantages in manufacturing costs and construction. They

are less suitable for tall apertures as restraining struts are necessary to prevent blade deformation due to centrifugal forces at higher speeds [42]. It has been shown that, for H-rotors, lower aspect ratios (height/radius) result in higher performance coefficients and the use of wider, shorter (and therefore structurally more robust) blades [43]. Low aspect ratios also give higher moments of inertia resulting in a smoother output. Unlike HAWT blades, Darrieus blades are subject to forces that vary significantly in magnitude and direction during each rotor revolution. This has implications for failure modes and the required quality of blade fixings. Darrieus WTs have poor starting characteristics in low wind speed situations such as the urban environment. It has been shown that, for reliable startup, in steady wind conditions and at light loading, a minimum of three blades is required [44]. Increasing the blade count further begins to introduce blade wake interactions that reduce the overall performance coefficient.

Torque variations in VAWTs are more complex than those seen on HAWTs. For a Darrieus WT, the number of torque 'pulses' seen over one revolution equals the blade count. Each blade, however, is subject to forces that are constantly changing in magnitude and direction. The overall instantaneous torque is the sum of the instantaneous torques operating on each blade. Figure 2.5 shows the output for a two-bladed Darrieus from a study carried out in [45]. There are three plots, one for each blade and one showing the overall torque characteristic. It can be seen that, for each blade, there is a major peak, some minor peaks and positions with significant negative values. The overall characteristic shows two major peaks with undulating areas between them that are slightly negative or close to zero. The graph demonstrates clearly why a minimum of three blades is required for self-starting in any position. The plot was taken for a WT with solidity (σ) of 0.2 and a TSR (λ) of 3.6.

Solidity is defined as:

$$\sigma = \frac{z\,c}{2\,\pi\,R} \tag{2.18}$$

where:

σ = Solidity, z = Blade Count, R = Rotor Radius (m) and, c = Blade Chord Width (m).

Solidity is fixed for a given device but as TSR varies the size and relative positions of the major and minor torque peaks vary in a way that is difficult to model using analytical functions. This is because there are complex interactions between the blades and their wakes which depend on wind velocity and WT angular velocity. It is necessary, therefore, to use numerical methods, such as CFD analysis to model WT behaviour.

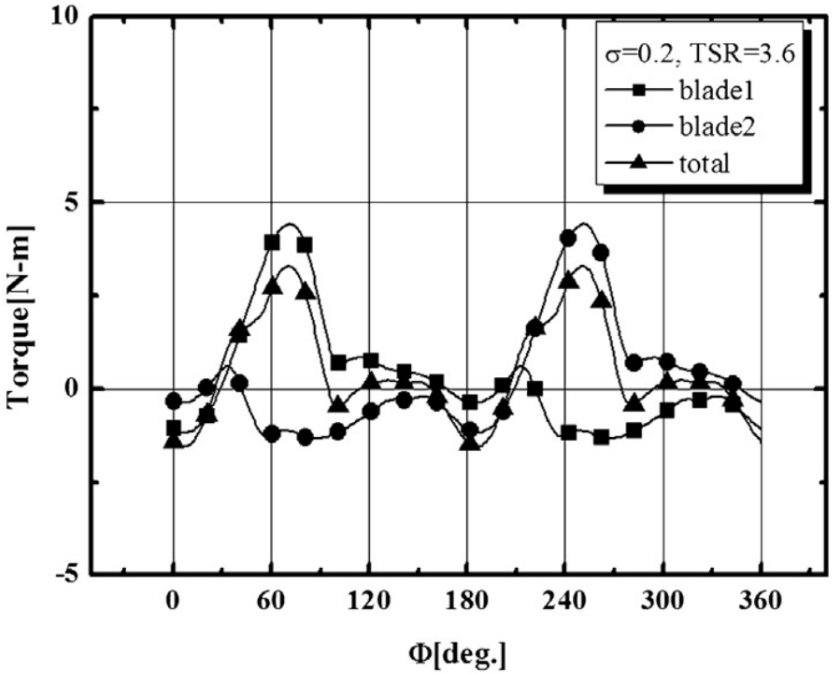

Figure 2.5: Torque Position Plot for a Two-Blade Darrieus WT [45]

The Savonius WT, as originally proposed by S J Savonius [46], is designed to be self-starting in any position. It is a relatively heavy, low-speed, high torque device which utilises aero-

dynamic drag to extract wind energy.

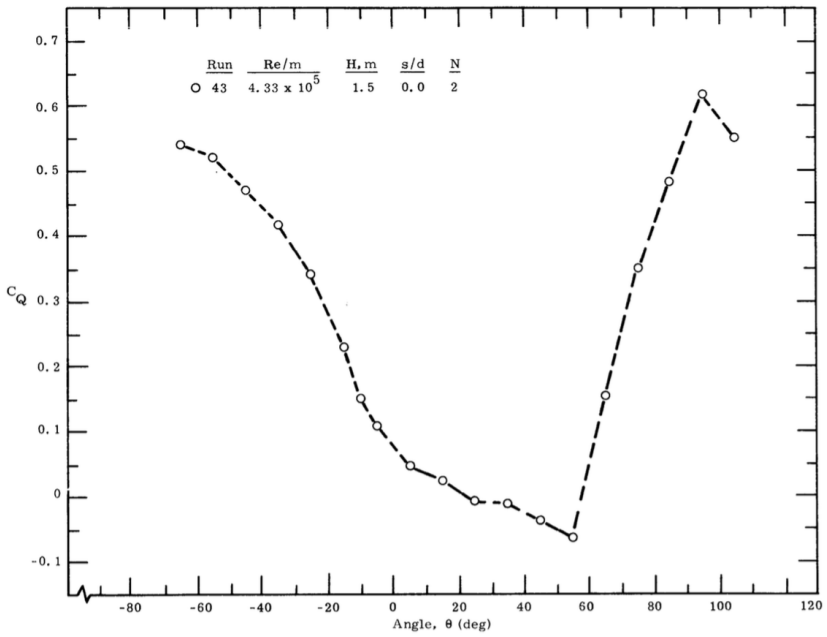

Figure 2.6: Torque Position Plot for a Two-Blade Savonius WT [47]

Figure 2.6 shows the torque coefficient graph for a two-blade Savonius WT presented in [47]. Like the Darrieus WT the number of peaks correspond to the number of blades and, over the 180 ° interval shown, this pattern can be observed. Unlike the Darrieus WT an individual blade contribution cannot be isolated since the torque developed depends on drag difference between the blades. Compared to the Darrieus device the sector of zero and negative torque values extends over a smaller angle and the relative depth of the negative trough is smaller. Savonius rotors have good starting characteristics but poor power coefficients so, until recently, Darrieus devices have been favoured for small, urban wind applications. The use of higher blade counts have been tried as a means of ensuring reliable start up, however, even with higher blade counts the Darrieus WT needs low loading and a steady wind. To ensure reliable startup, and thus increase ALF, interest has grown in developing multi-bladed drag-based devices with improved power coefficients to extract

wind energy in the urban environment. Such machines usually include some form of static air directing mechanism or stator and are often referred to as crossflow devices.

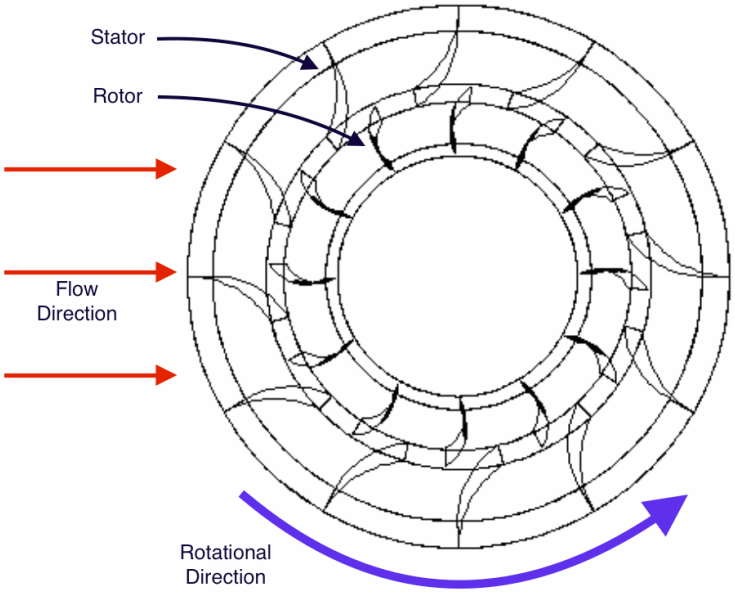

Figure 2.7: Twelve-Bladed Cross-Flow VAWT with Stator [48]

Figure 2.7 shows the plan view of a twelve-bladed, cross-flow, drag-based, VAWT with a twelve-element stator, originally designed by Colley [18]. It is a uni-directional, high-torque low-speed device with a maximum TSR of just over one. It exhibits excellent starting characteristics at low wind speeds with no sectors of negative torque across the normal operational TSR range. It achieves a peak performance coefficient of $C_p = 0.35$. This is considerably better than the Savonius device, which can exhibit $C_p = 0.16$, and approaching that of the Darrieus at $C_p = 0.4$

The torque characteristic for a crossflow device is complex as Figure 2.8 shows. The aerodynamic torque pattern over one revolution at a wind speed of $6\,ms^{-1}$ and TSR of 0.2 shows the repeating twelve-cycle pattern expected from a twelve-bladed device. It can be seen that there is a major and minor peak and trough associated with each $30\,^\circ$ blade

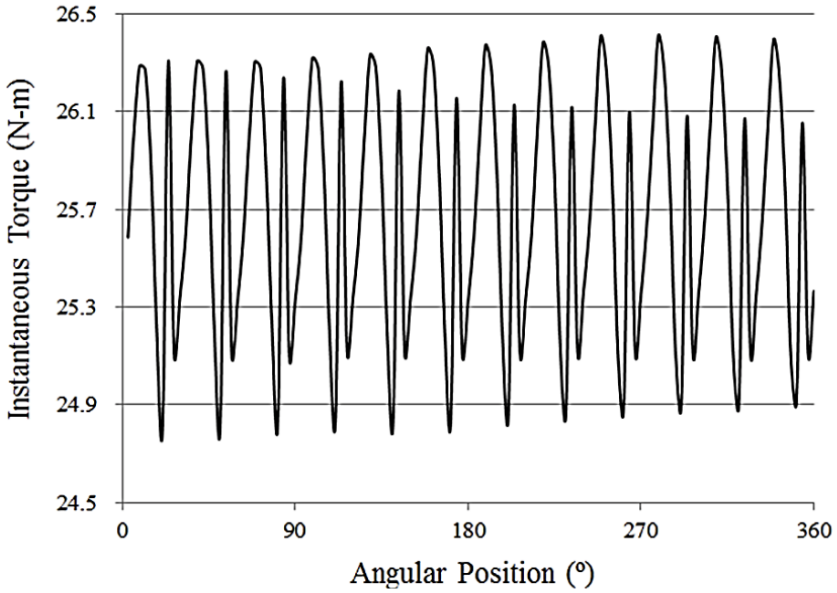

Figure 2.8: Torque Position Plot for a Twelve-Blade Cross-Flow WT [49]

cycle. The plot displayed is derived from a CFD analysis [49]. Analysis over the TSR range, for these devices, show that the absolute and relative magnitudes, and positions, of these major and minor peaks vary with TSR. It is, therefore, not practical to approximate behaviour using analytical functions.

2.3 Wind Turbine Emulation

A WTE system comprises a motor and drive arrangement coupled to a load. Motor torque is controlled to reproduce that of the emulated WT, over the intended range of input wind velocities and TSRs, when coupled to the load. The attached load may be one that the emulated turbine is designed to drive together with its control system. Alternatively, a programmable load, designed to emulate different types of load regime, may be used allowing more diverse testing to be carried out.

Test bed emulation of WT behaviour is often used for initial assessment of candidate WT

configurations prior to the commitment of significant resources to the design process. The immediate need to construct a device and carry out wind tunnel testing can be delayed or, in the case of unsatisfactory emulated performance, avoided. When a physical device has been constructed, wind tunnel testing provides a controlled aerodynamic environment to, confirm that device behaviour meets the specification, optimise WT/generator arrangements and control methods, and develop fault diagnosis techniques. Wind tunnel testing facilities are, however, relatively scarce, costly, and can be difficult to schedule, so WTE is often used to reduce dependence on this technique. In summary, accurate WTE may be used for:

- The rapid effective modelling and preliminary assessment of new WT designs.
- The optimisation of WT and generator combinations for their intended aerodynamic situations.
- The optimisation of load control methods.
- The development of condition based maintenance/reporting and automated fault diagnosis techniques.

The recent growth in interest and research into small/micro wind applications, including VAWTs in the urban environment, means that this well established technique continues to be valuable. It is also necessary that the technique evolves to keep pace with new WT designs that exhibit increasingly complex aerodynamic torque characteristics.

The simplest WTE systems replicate steady-state, non-dynamic, WT behaviour over the designed ranges of wind velocity and TSR. More advanced systems incorporate inertia compensation and some additionally attempt to model the intrinsic torque characteristics of the WT. Examples of schemes based on either, the power coefficient (C_p) [50][51], or

the torque coefficient (C_t) [52][53][54], may be found in the literature. These use (2.8) and (2.10) respectively as the basis for generating the required emulating motor output based on input wind speed (V_w), device angular velocity (ω), rotor radius (R), aperture area (A) and air density (ρ). Since torque is the process variable, schemes are usually based on the torque coefficient model. This has an important advantage over power coefficient based systems, because, for a stationary machine, TSR is zero, but torque, unlike power, is non-zero when wind speed is non-zero. Figure 2.9 shows the CFD predicted power and torque characteristic curves for a particular VAWT designed by Colley [18] that might form the basis of such a system. It can be seen that start up from rest is more easily achieved using the torque characteristic. Figure 2.10 illustrates the torque setpoint generation algorithm for a simple steady state, non-dynamic WTE system.

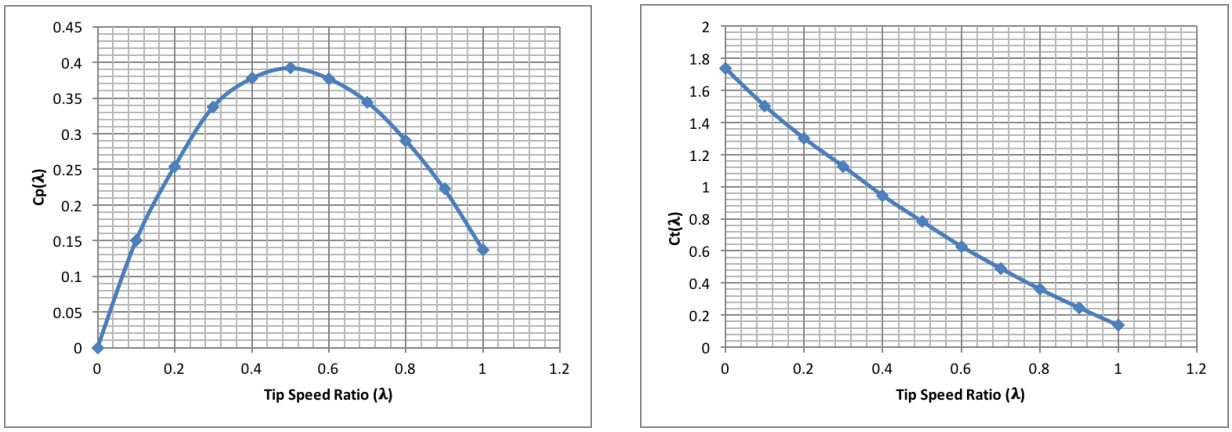

(a) Power Coefficient v TSR

(b) Torque Coefficient v TSR

Figure 2.9: Average Power and Torque Coefficient Graphs for a Crossflow VAWT [18]

To accurately reproduce dynamic WT behaviour due to changes in external factors, such as wind speed or load, it is necessary to compensate for the difference in moments of inertia between the WT to be emulated and the emulating system. A widely used technique involves observing angular acceleration in order to generate a 'compensating torque' for adjustment of the calculated aerodynamic torque. Figure 2.11a shows a simple mechanical

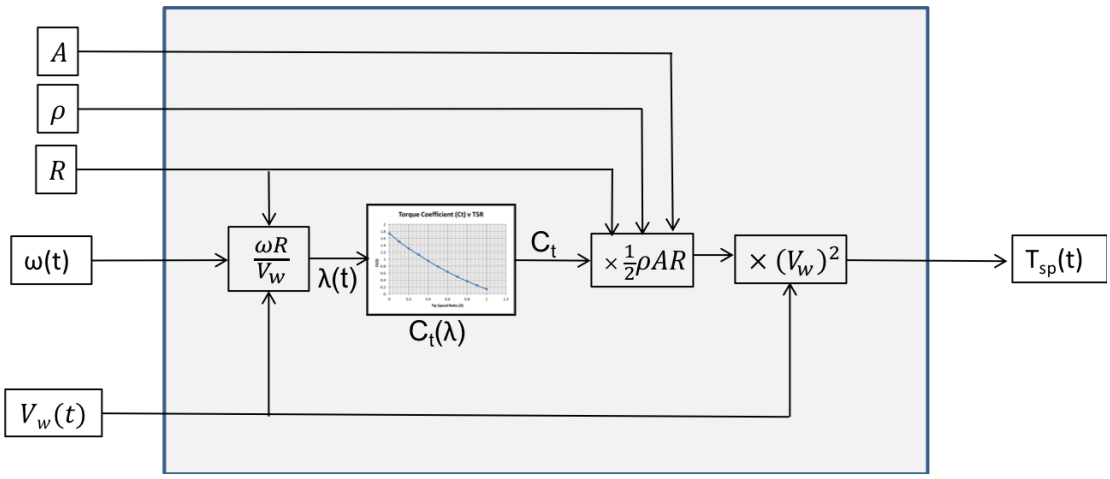

Figure 2.10: Simple Steady State Average Torque WTE Algorithm

model of a WT (with moment of inertia J_{wt}) driving a load generator (with moment of inertia J_g) via a 1:n gearbox. (Such an arrangement is often necessary to match a low speed WT to an appropriately rated generator.) WT and generator shaft angular accelerations are given by α_{wt} and α_g respectively. The aerodynamic input torque is T_{ad} and the generator load torque is T_g. Figure 2.11b shows the equivalent model for the WTE system that must replicate WT behaviour. In this example, the system is driven by a servomotor (with moment of inertia J_{sm}) that generates torque T_{sm} and is directly coupled to the load generator. The servomotor and generator angular accelerations are α_{sm} and α_g respectively and are equal. It is assumed that both systems are rigid and frictional forces are negligible.

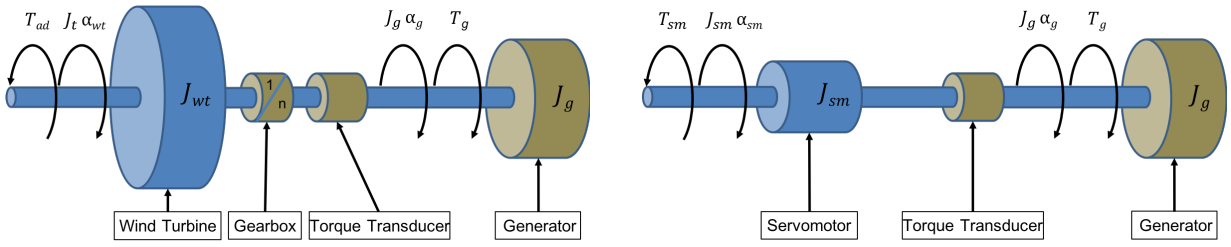

(a) Wind Turbine System (b) Wind Turbine Emulator

Figure 2.11: Simple Mechanical Models

Referring the WT parameters to the gearbox output gives:

$$T'_{ad} = \frac{T_{ad}}{n}, \quad J'_{wt} = \frac{J_{wt}}{n^2} \quad \text{and} \quad \alpha'_{wt} = n\,\alpha_{wt}$$

Then the WT equation of motion can be expressed as:

$$T'_{ad} = J'_{wt}\alpha'_{wt} + J_g\alpha_g + T_g \tag{2.19}$$

The equivalent expression for the WTE is:

$$T_{sm} = J_{sm}\alpha_{sm} + J_g\alpha_g + T_g \tag{2.20}$$

For correct operation α_g in both systems must be equal to α'_{wt}. Subtracting (2.19) from (2.20) and substituting for α'_{wt} gives:

$$T_{sm} = T'_{ad} - \alpha'_{wt}(J'_{wt} - J_{sm}) \tag{2.21}$$

It can be seen that the required servomotor setpoint value equals the referred aerodynamic torque minus a compensating torque value.

This control scheme utilises an angular acceleration observer which depends on differentiation of a velocity signal. In a practical system the differentiator must be preceeded by a Low-Pass Filter (LPF) to supress high frequency noise. Figure 2.12 illustrates the algorithm.

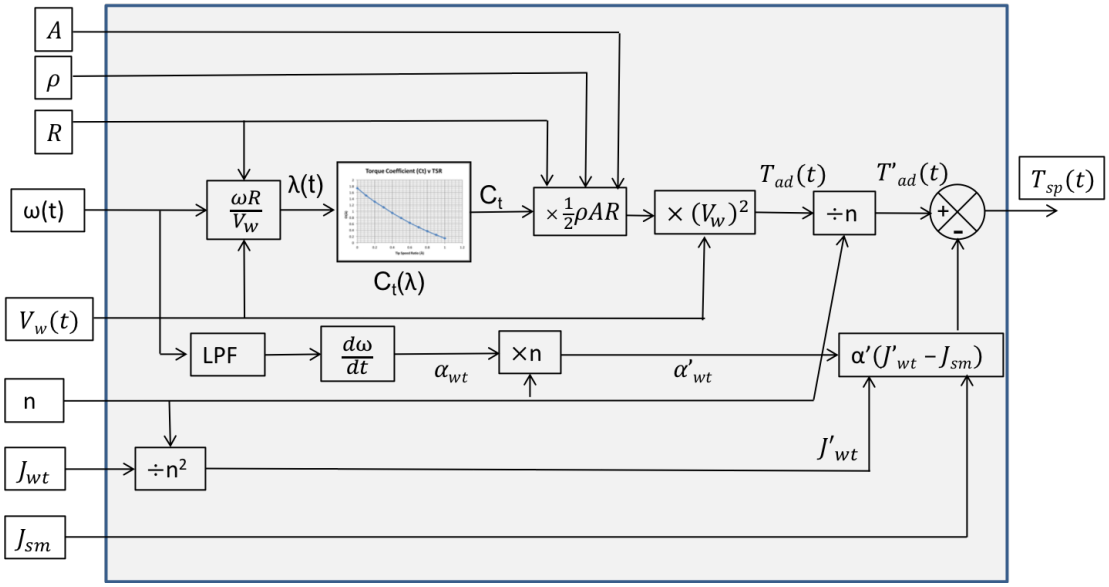

Figure 2.12: Inertia Compensating WTE Algorithm using Acceleration Observer.

An alternative inertia compensation method requires the use of a torque transducer rather than an acceleration observer [55]. From Figure 2.11a the referred aerodynamic torque (T'_{ad}) may be expressed in terms of, shaft torque (T_T), as measured by a torque transducer, and the inertial torque due to J'_{wt}:

$$T'_{ad} = T_T + J'_{wt}\alpha'_{wt} \tag{2.22}$$

From Figure 2.11b, the equivalent expression for the WTE system is:

$$T_{sm} = T_T + J_{sm}\alpha'_{wt} \tag{2.23}$$

For correct emulation the torque transducer values (T_T), in each case, are required to be equal, so eliminating the α'_{wt} term from (2.22) and (2.23) gives:

$$T_{sm} = T'_{ad}\left(\frac{J_{sm}}{J'_{wt}}\right) + T_T\left(1 - \frac{J_{sm}}{J'_{wt}}\right) \tag{2.24}$$

This equation leads to the inertia compensating WTE algorithm shown in Figure 2.13:

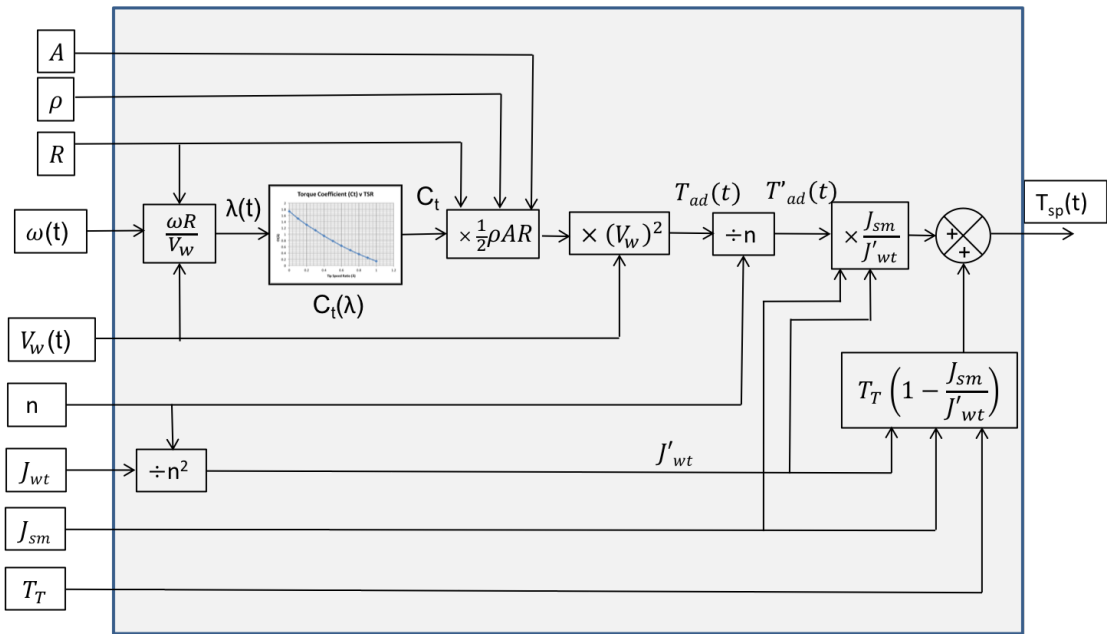

Figure 2.13: Inertia Compensating WTE Algorithm using Torque Transducer.

To accurately reproduce dynamic WT behaviour due to intrinsic characteristics, it is usual for the mean aerodynamic torque signal (T_{ad}), or wind velocity signal (V_w) to be modulated in accordance with an appropriate model. The aerodynamic torque modulation, as shown in Figure 2.2, Section 2.1, may be achieved using a 'ramp' function [35]. Alternatively, the torque signal can be modulated using a 'limited sine' function, rather than a 'ramp' [36] [50]. A more accurate 'equivalent wind' velocity model given by equation 2.13 may also be used to generate the required aerodynamic torque signal [38]. Intrinsic WT dynamic behaviour is a function of rotor position, so incorporating this feature involves monitoring emulated rotor position.

All the examples of WTEs providing intrinsic as well as external dynamic behaviour simulation discussed in this section, relate to HAWTs. Recent papers on VAWT simulation, incorporating inertia compensation have been found [56]. However, no examples of VAWT

simulation incorporating intrinsic dynamic healthy, or faulted behaviour, have been discovered. The methods currently used to achieve this capability for HAWTs are inadequate for VAWTs. Current WTE techniques are, therefore, limited in their ability to support the development of novel VAWT designs for use in the urban environment so research into the enhancement of WTE methods is necessary. Models of driving aerodynamic torque characteristics, for VAWTs across their operational ranges of TSR, wind velocity and rotor position, are now routinely derived using CFD analyses and may be found in the literature[57][58][59]. CFD does not model dynamic behaviour associated with device moment of inertia and loading or provide a physical output. It is intended to use CFD analyses as the basis of a novel method for accurate VAWT emulation to address this issue and thus make a contribution to knowledge.

2.4 Urban Wind Turbine Condition Monitoring

All rotating machinery is subject to operational wear, that eventually leads to faults and breakdown. To maximise return on capital invested, it is usual to implement a maintenance regime to minimise fault-related downtime and repair costs. Three possible approaches to fault management have been described [60] to justify the use of CBM:

1. Maintain on breakdown.
2. Scheduled maintenance.
3. Condition Based Maintenance (CBM).

The first approach is inherently unpredictable so resource planning and allocation is difficult. As plant ages, breakdowns may occur at any time so resources may not be immediately available to deal with the fault and restore service. Allowing equipment to fail, often results in additional damage to plant and ancilliaries beyond the original causal fault. This

not only increases repair costs but also increases downtime costs as the machine will be out of service for longer. If a group of similar machines have been installed at the same time, it is likely that after a period of reliable operation there will be multiple failures over a relatively short period of time.

Scheduled maintenance allows easy resource management and is intended to reduce the instances of catastrophic failure associated with the first approach. Maintenance periods are based on the pre-existing knowledge of plant failure modes and may vary depending on the operational environment and the loading. To be effective, a cautious approach is usually adopted, so work is often carried out before necessary and up to 90 % of service parts are replaced before they have reached the end of their serviceable life [60]. When a plant is taken out of service for maintenance there are associated downtime costs. Mistakes made during maintenance procedures can precipitate faults in 1.3 % of interventions as reported in [61].

CBM based on a limited set of observation techniques has been used since the 1970s [62]. However, the availability of increasingly powerful diagnostic technologies from the late 1990s has seen its application grow. The engineering industry has embraced CBM because it provides early warning of incipient faults facilitating the scheduling of resources for the pre-emptive repair work. It avoids premature changes of service parts and minimises the number of maintenance outages thus reducing downtime, servicing costs and occasions for maintenance induced faults. In the context of WTs, CBM ensures that design ALF is maintained which is critical to economic operation. CBM requires some degree of instrumentation or transduction to facilitate monitoring. The complexity and cost of this aspect is a function of the value of the WT being monitored, since additional capital invested must show an adequate return in terms of reduced downtime and damage costs. Interpretation

of data gathered relies on the pre-existing knowledge of the failure modes of the plant. For new designs this may be based on analytical predictions of the plant behaviour and knowledge of a similar plant. The advantage of gathering such data is that a database may be built and by analysis, predictive methods may be improved based on real performance in various environments and loading regimes. Monitoring, therefore, facilitates improvement of operation and maintenance regimes and provides useful data for design improvements.

CBM relies on the following four processes [63]:

1. Transduction.
2. Data Acquisition including signal conditioning.
3. Data Processing.
4. Diagnostics and Prognostics.

It is important to differentiate between fault identification for protection purposes and incipient fault diagnosis for CBM. The former may use some of the same transducers to achieve functionality but the detection process must occur in real time, and be continuous and autonomous. The diagnosis of incipient faults and associated plant prognosis functions are intended to predict problems that are not immediate. It may not be necessary, therefore, to monitor continuously. WT behaviour could be sampled at timed intervals or based on operating conditions or a combination of these. It is only necessary that the plant behaviour is observed sufficiently often to ensure that deteriorating trends in performance are not missed. Where the monitoring process is passive, or non-intrusive, the plant operational behaviour is simply observed. Some regimes also supplement passive methods by periodically using intrusive techniques. This involves the application of a forcing function and the observation of resulting plant behaviour. The manipulation of generator torque

in a WT system to change system bandwidth and thus alter the magnitude of electrical signal spectral components of interest, falls into this category.

Transduction and local data acquisition are invariably carried out in near-real-time with sample rate and resolution determined by the required bandwith and quality of the signals to be monitored. Data processing and diagnostics may be carried out locally or remotely. For the local case these processes will be near-real-time and the interpreted data used to check performance against known 'fault signatures'. Another local method compares actual WT behaviour with a model of expected behaviour based on current operating conditions [64]. The difference, or 'residual', between model and system is used to draw conclusions about system health and prognosis. Local data processing and diagnostics requires local intelligence in the form of an embedded microcontroller or Application Specific Integrated Circuit (ASIC). It is also necessary that the results of local diagnostic assessments are communicated periodically. Where diagnostics are carried out remotely, data acquistion includes data communication and transmitted contemporaneous data samples will be time-stamped. Onshore and offshore wind turbines create a great deal of data due to the large number of measurands that are processed. These systems also use dedicated communication channels and protocols to ensure accurate and secure data transmission. Small WTs, located in the urban situation, generate less data as the inclusion of transducers must be minimised due to economic constraints. The provision of a dedicated communication channel for each device is neither feasible nor necessary since the ubiquity of broadband internet connections provides a scalable solution to cope with any projected proliferation of these devices.

The advantage of remote processing and diagnostics is that algorithms for fault detection may be updated in the light of data acquired from many similar devices. Failure modes

and preceeding trends will become identifiable from a database of turbine behaviour. It also provides the opportunity to compare WT performance with that of adjacent WTs [65]. Machine learning could be applied to the observed correlations between turbine performances under various conditions and used to spot trends indicating an individual turbine's deterioration.

2.4.1 Measurands and Methods

Large scale WECS incorporate extensive instrumentation monitoring a wide variety of parameters. This is justified due to the high capital value of the plant and the high value of potentially lost revenue due to downtime. The parameters typically monitored include [65][66][67]:

- Vibration.
- Acoustic Emissions.
- Strain.
- Torque.
- Temperature.
- Oil Analysis.
- Electrical Signals.
- SCADA Signals.

Such extensive instrumentation is economically infeasible for small-scale urban WTs. Individual WTs have relatively low capital value, but also exhibit relatively low ALFs. To ensure economic viability, some form of inexpensive CBM is appropriate to ensure that

design ALFs are maintained. The electrical signals available at generator output terminals may be monitored easily and cheaply and are therefore suitable. These signals are modulated by the mechanical behaviour of the WT and may be used to monitor the condition of turbine blades and other mechanical components in the drive train. They are, however, non-stationary which introduces difficulties in the interpretation of time-domain and frequency-domain outputs. Several authors suggest solutions to this issue which include the use of Wavelet Analysis [68][69], and artificially generating stationary signals by some form of synchronous sampling based on rotor position [64]. This latter technique requires the inclusion of a position transducer at extra cost, but facilitates observation of rotor velocity and acceleration. The further addition of wind velocity monitoring provides the means to utilise internal comparative process models or external comparison with adjacent installations.

2.5 Research Aim and Objectives

From this review it is concluded that current WTE methods, applicable to HAWTs, are inadequate for simulating the complex behaviour of recent, multi-bladed, VAWT designs intended for use in the urban environment. CFD techniques are now used widely in the design and analysis of such turbines, however, these are also insufficient as inertial response is not modelled. The inherent low-pass filtering effect of the mechanical system, which varies with load stiffness, is thus not considered. To address these issues and contribute to knowledge, a novel WTE using CFD data as the basis of its operation will be designed. Given the requirement to model complex torque characteristics the WTE frequency response will be sufficiently accurate for CBM studies to be supported. A detailed research aim, intended to address the identified gap in knowledge, is presented below together with a set of specific objectives intended to achieve the aim.

2.5.1 Research Aim

To create an improved Wind Turbine Emulation technique to address the inability of current methods to emulate accurately, multi-bladed VAWTs designed for the urban environment. The novel aspect lies in the use of CFD predicted aerodynamic data as the basis for WTE operation. The WTE will be reconfigurable in terms of the CFD profiles that may be used and the dimensional aspects of the emulated device. Profiles may relate to the healthy and faulted behaviour of a particular turbine, and to a range of different turbines. The WTE will incorporate inertia compensation to ensure that the frequency response of the system to intrinsic characteristics and external events accurately reproduces that of the emulated device. The bandwidth will be sufficient to support the analysis of 'fault signatures' for CBM purposes. A servomotor and drive combination with a high resolution position encoder will be used because accurate control of output torque related to rotor position and velocity is essential. An accurate data capture capability, covering all relevant measurands and process variables, will be included.

2.5.2 Objectives

(I) To draw up a detailed requirements analysis, for the WTE, based on the known characteristics of a suitably complex multi-bladed VAWT for which CFD and wind tunnel data is available. The analysis will be used to derive a functional design specification.

(II) To implement a suitably rated programmable load for attachment to the WTE. The load will provide the necessary regimes for use during WTE development and final use. It will capture and condition the load generator current and voltage signals for presentation to the WTE system. The specification, design and implementation of the programmable load are set out in Appendix B.

(III) To implement the WTE design in Hardware and Software using industry standard equipment and tools.

(IV) To test, modify and retest the WTE as necessary to ensure that:

- The time and frequency-domain responses, for a suitably complex emulated VAWT at different physical scalings, meet the specification.
- The WTE system accurately reproduces the mean torque and power output behaviour of differently scaled, multi-bladed VAWTs.

(V) To capture for analysis, data from WTE system tests simulating healthy and faulty WT behaviour. Offline data analysis, from the tests, is to be carried out to assess the ability of the WTE system to facilitate development of WT fault diagnosis and CBM techniques.

2.6 Summary

The literature review carried out in this chapter has led to the identification of a relevant area for research. Consequently the design of a novel WTE method to support the research and development of VAWT devices for use in the urban environment has been proposed. A detailed research aim has been presented together with a set of objectives required to meet the aim. The next chapter begins by developing a design specification that is derived by considering the requirements for emulating a particular VAWT for which wind tunnel and CFD predicted performance data are available. The implementation of the proposed design is then presented.

Chapter 3

WTE System Design

3.1 Introduction

A multi-bladed VAWT, designed at the University of Huddersfield for use in urban environments, provides the basis for WTE system requirements analysis and design carried out in this thesis [18]. This complex, high-solidity, twelve-element stator/rotor device, shown in Figure 3.1, was chosen to ensure that the developed WTE system would be reconfigurable for a wide range of WT designs using the same fundamental CFD based approach. The VAWT is optimised for a wind speed of $4.5\,ms^{-1}(16.2\,kmh^{-1})$, characteristic of an urban situation, and develops high torque from start up and at low angular velocities. Further CFD modelling on the same VAWT, predicting rotor aerodynamic torque variations over one revolution for a range of TSRs, was carried out as part of an investigation into the effects of blade faults in [70]. The CFD data derived from this investigation has been used for the development of the WTE control algorithm outlined in this thesis.

A schematic diagram of the 12-bladed VAWT is shown in Figure 3.2 where the plan view shows the concentric arrangement of the stator and rotor. The device is uni-directional, rotating in a clockwise direction (as viewed from above) regardless of the wind direction. The stator directs air into and out of the central area containing the rotor. Returning

(a) Side View (b) Top View

Figure 3.1: High-Solidity Twelve-Bladed Crossflow Vertical-Axis Wind Turbine with Stator

rotor blades are shielded from incoming air which is directed towards the rotor in a way that maximises positive torque. The flow of air through the WT is complex and, in order to calculate total instantaneous applied torque at any rotor position, it is necessary to calculate and sum the instantaneous torque values for each blade at that rotor position. At a given TSR the applied torque varies cyclically with position, as shown in Figure 3.3. It can be seen that, since the rotor has rotational symmetry of order twelve, the torque pattern repeats every 30 degrees. Air flow through the VAWT and its subsequent effect on each rotor blade is affected by the angular velocity of the rotor so the cyclic pattern of input torque fluctuations varies with TSR.

The initial WT test process, carried out in [18], provides data used to inform WTE system and development and that of the associated programmable load. During these tests, the VAWT rotor shaft was coupled to an electrical generator via a gearbox as shown in Figure 3.2. A gearbox was used in the arrangement to match the torque and angular velocity characteristics of the generator used to those of the VAWT. The VAWT was placed in a wind tunnel and, for a range of wind velocities, the mechanical load on the VAWT was varied by manipulating the electrical load connected to the generator. Values for; torque,

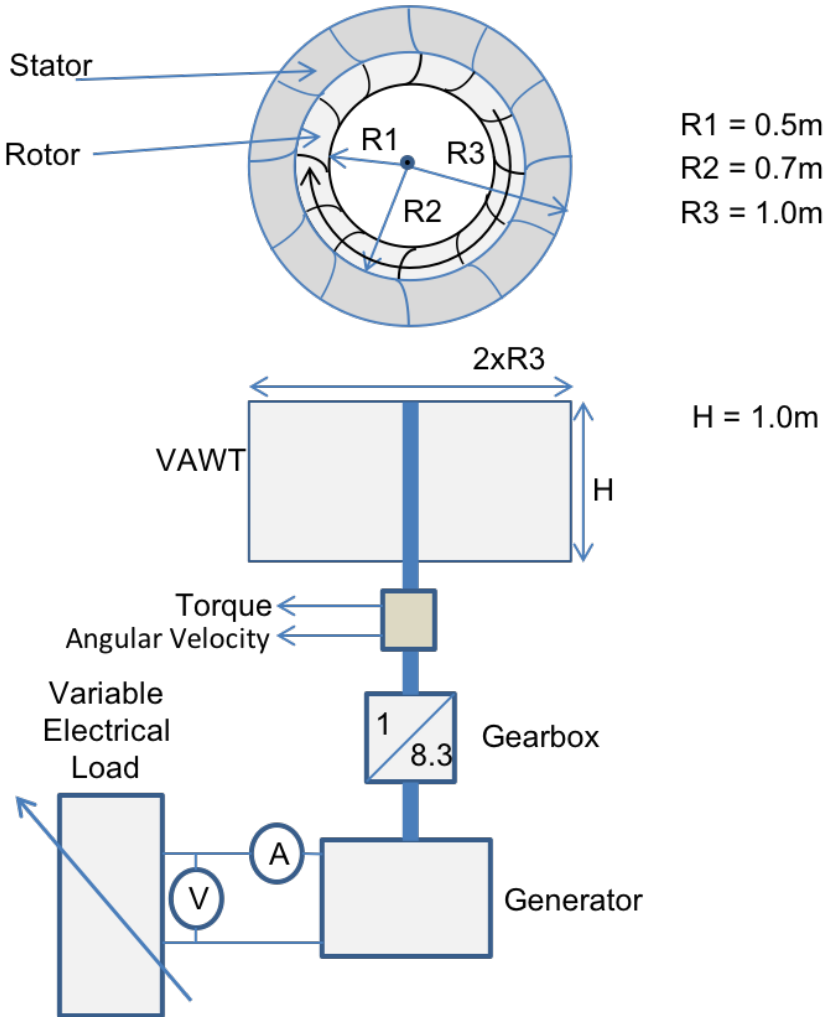

Figure 3.2: Original Test Set-Up for Twelve-Bladed VAWT [18]

rotor angular velocity, load voltage and current were recorded and correlated with the applied wind velocity. Table 3.1 summarises the recorded VAWT parameters that were relevant to the derivation of the WTE system Requirements Specification.

Table 3.1: Summary of Vertical-Axis Wind Turbine Parameters Relevant to Emulator Design

Number of Stator Vanes	12 (30° spacing)	
Number of Rotor Blades	12 (30° spacing)	
Rotor Inner Radius (R1)	0.5	m
Rotor Outer Radius (R2)	0.7	m
Stator Outer Radius (R3)	1.0	m
Rotor/Stator Height (H)	1.0	m
Aperture (A) = 2 x R3 x H	2.0	m^2
Assumed Air Density (ρ)	1.225	kgm^3
Rotor Moment of Inertia (J_{wt})	2.02	kgm^2
Design Mean Wind Velocity (V_w)	4.5	ms^{-1}
Wind Velocity Range	0 - 12	ms^{-1}
Tip Speed Ratio Range	0 - 1	
Maximum Angular Velocity (ω_{max}) based on Maximum Wind Velocity and $\lambda = 0.9$	15.4	$rads^{-1}$
Corresponding Angular Velocity at Gearbox Output Shaft (1:8.3)	127.8	$rads^{-1}$
Maximum Torque based on Maximum Wind Velocity and $\lambda = 0.1$	166.5	Nm
Corresponding Torque at Gearbox Output Shaft	20.1	Nm

3.1.1 CFD Performance Models

The CFD model [70] referred to in Section 3.1, provided a dataset detailing aerodynamic torque variation over a complete revolution for nine TSR values between 0.1 and 0.9 inclusive at 3 degree intervals. The study was based on a wind speed of $4.0\,ms^{-1}$ and provided absolute rather than normalised torque values. The graph shown in Figure 3.3, shows predicted aerodynamic input torque, over one complete revolution, for a TSR of 0.5. Similar graphs were derived for all the TSRs considered. Graph shape varies significantly with TSR, however, the 12-cycle pattern, associated with the 12-blade construction is always

observable.

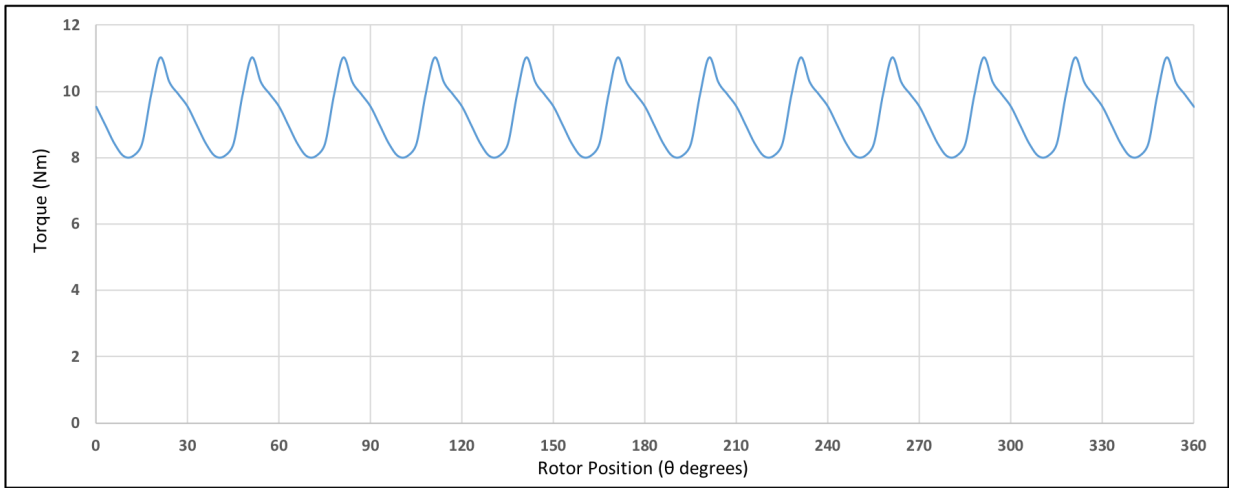

Figure 3.3: CFD Predicted Aerodynamic Torque variation with Rotor Position (TSR=0.5, $V_w = 4.0\,ms^{-1}$)

As part of the study, average torque values over one revolution, for each TSR dataset, had also been calculated and used to generate a graph of predicted average torque against TSR shown in Figure 3.4a. The corresponding graph of average power against TSR, derived by taking account of the rotor angular velocity, is shown in Figure 3.4b. These graphs are only valid at a wind velocity of $4.0\,ms^{-1}$. To predict behaviour across the required range of wind velocities it was necessary to generate generic torque and power coefficient function characteristic graphs. This was achieved by substituting parameters from Table 3.1, and the graphs in Figure 3.4, into (2.8) and (2.10). The resulting coefficient graphs are shown in Figure 3.5 where it can be seen that predicted peak power occurs at a TSR of approximately 0.47. The mean power and torque coefficient graphs were used in the system design process to estimate the required WTE system operating ranges and corresponding values for the programmable electrical load. It should be noted that the graphs have been extrapolated to provide values for a TSR of zero. This facilitates the emulation of WT 'start-up' from rest when TSR is zero.

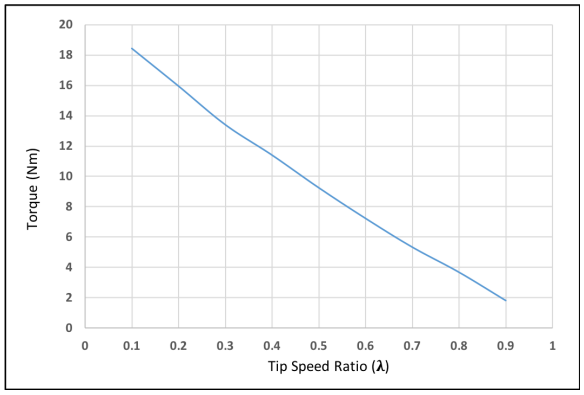

(a) Torque v TSR

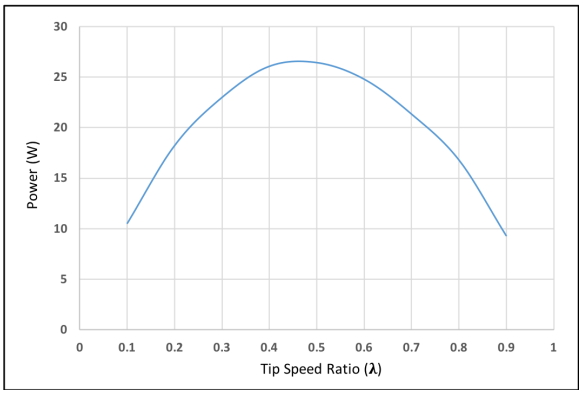

(b) Power v TSR

Figure 3.4: Average Torque and Power Predictions from CFD Study

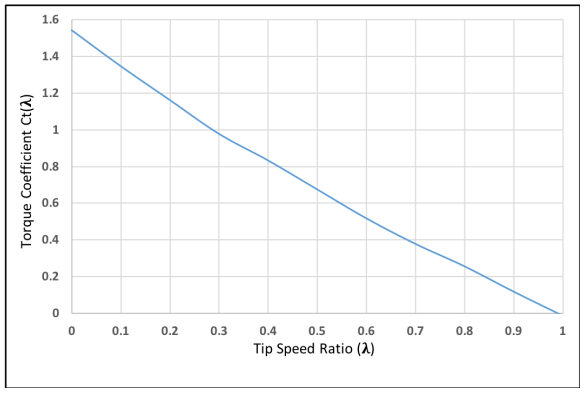

(a) Ct v TSR

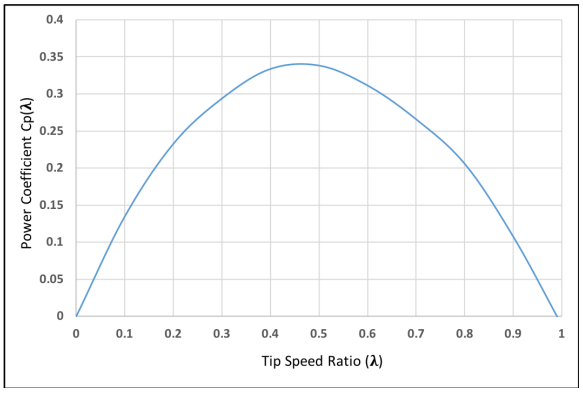

(b) Cp v TSR

Figure 3.5: Extrapolated Average Torque and Power Coefficient Graphs derived from CFD Study

The average-torque-coefficient graph is often used as the basis for steady state emulation at any wind velocity within the model range. The method is usually extended to emulate transient WT behaviour brought about by wind velocity or load changes by using one of the moment of inertia torque-compensation techniques discussed in Chapter 2. However, such methods are inadequate when it is required to emulate inherent dynamic aspects of the WT, such as aerodynamic torque variation associated with blade configurations and faults. To emulate these it is necessary to return to the original set of torque versus angu-

lar position graphs for each TSR. Figure 3.6a, shows an expanded, normalised 30 degree section of the 360 degree graph from Figure 3.3. One cycle of the torque variation associated with each 'blade-period' is shown and, in a healthy VAWT, each of the sequential 12 'blade-periods' exhibits an identical torque pattern.

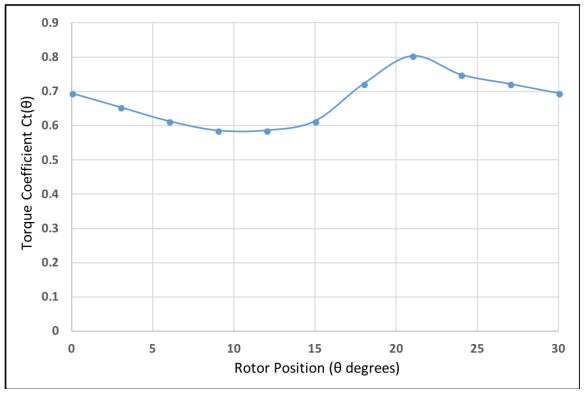

(a) Torque Coefficient Variation with Rotor Position (TSR = 0.5)

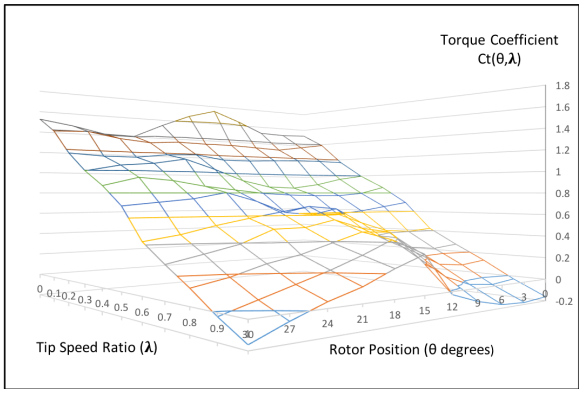

(b) Torque Coefficient Variation with Rotor Position and TSR

Figure 3.6: CFD Predicted Torque Coefficient Variation over a 30 ° Interval

The pattern in Figure 3.6a relates to a single TSR, however, as torque is applied, TSR changes. To take account of this the complete set of 30 degree torque patterns was assembled to generate a surface graph displaying torque coefficient as a function of both TSR and angular position. The result is shown in Figure 3.6b where it can be seen that the Vector (θ, λ) maps to the Scalar (C_t) thus providing a method for torque set-point derivation. Detailed predicted torque coefficient patterns, such as these, underpin the WTE algorithms developed in this thesis.

To emulate a 'healthy' WT, over one revolution, the data derived for one 'blade-period' may be used repeatedly; however, this is not the case for the emulation of a faulty WT. An example of a graph relating to a faulty VAWT, with one missing blade, derived from the work presented in [70], is shown in Figure 3.7a. Figure 3.7b shows the associated

'healthy' graph for comparison. Both graphs display the underlying 12^{th} harmonic relating to blade period, but in the faulty case, lower order, superposed harmonics are also evident. A torque surface graph extending over a complete revolution is necessary for the emulation of a faulty WT so the default model for the WTE system uses a 360 degree model.

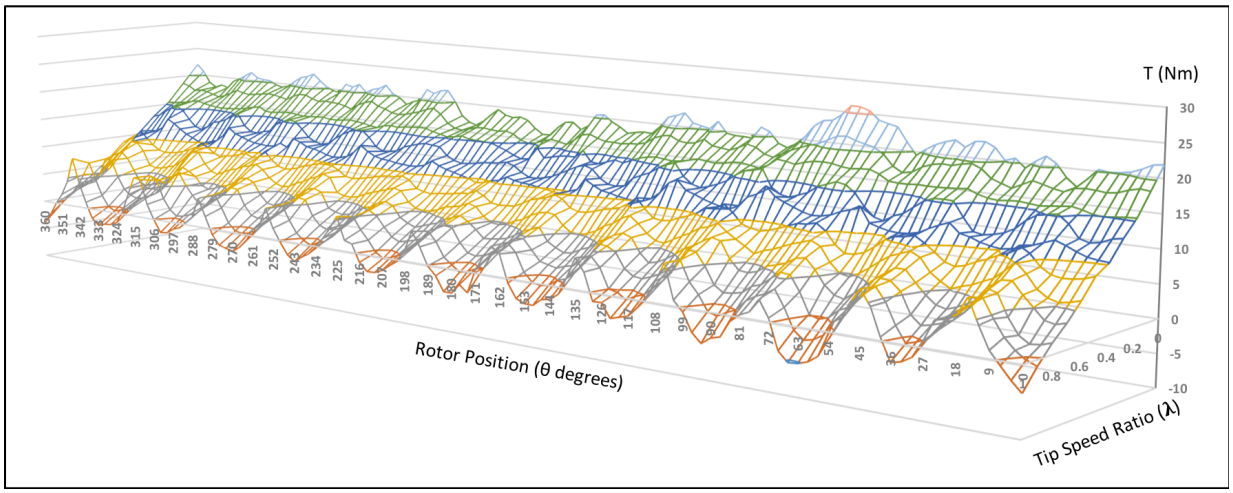

(a) VAWT with One Faulty Blade

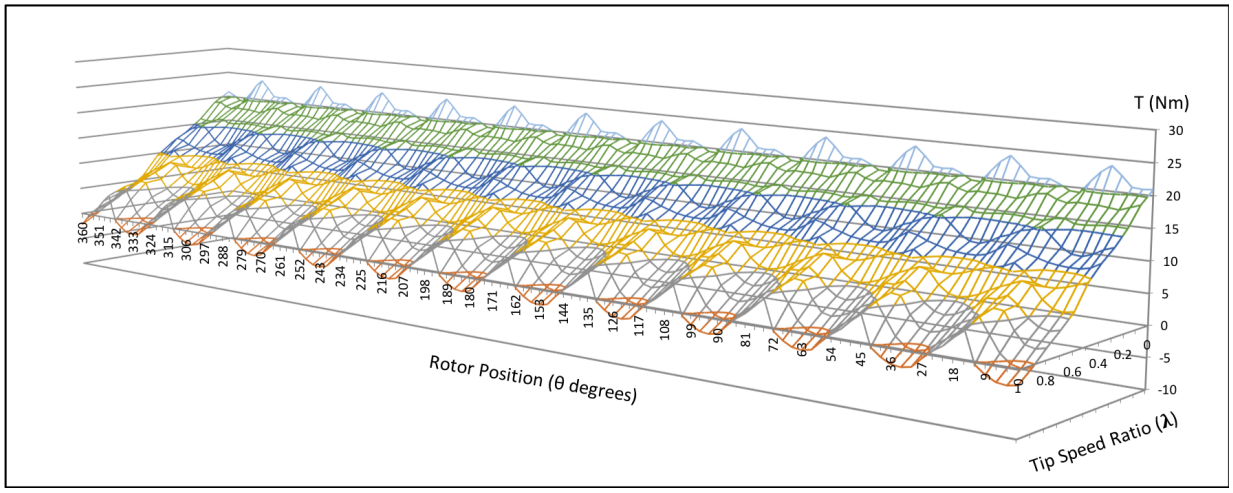

(b) Healthy VAWT

Figure 3.7: Torque Surface Graphs for VAWT

3.1.2 WT System Bandwidth

The torque surfaces in Figure 3.7 represent torque input to the WT rotor. However, the WTE is required to emulate torque output. The rotor has inertia so, when the WT drives a load resistance proportional to angular velocity, it acts as a low-pass filter thus setting an upper limit on the required WTE frequency response. Figure 3.8 shows a simple rigid mechanical model for the VAWT system where:

T_{ad} = Aerodynamic Input Torque (Nm), T_g = Output Load Electromagnetic Torque (Nm),
J_{wt} = Rotor Moment of Inertia (kgm^2), J_g = Generator Moment of Inertia (kgm^2),
k = Generator Load coefficient (Nmsrad^{-1}) and, ω_{wt} = Rotor Angular Velocity (rads^{-1})

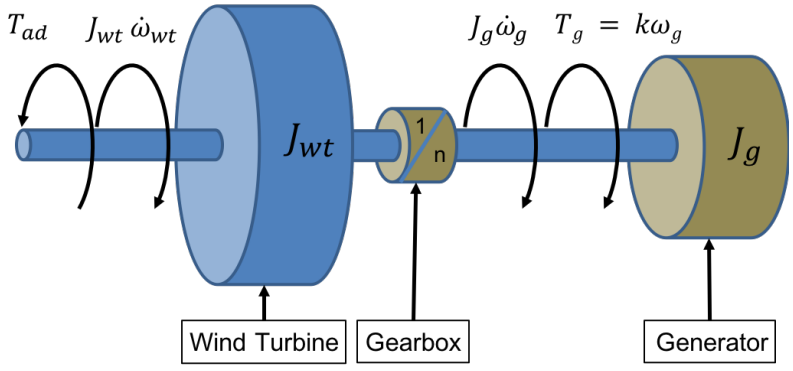

Figure 3.8: Wind Turbine System Mechanical Model

Aerodynamic torque input (T_{ad}) is opposed by the accelerating torque on the combined masses of the rotor and generator and the generator electromagnetic load torque (T_g). Referring the generator parameters to the gearbox input gives:

$$J'_g = J_g \times n^2, \quad \dot{\omega}'_g = \frac{\dot{\omega}_g}{n} = \dot{\omega}_{wt}, \quad \omega'_g = \frac{\omega_g}{n} = \omega_{wt}, \quad k' = k \times n^2, \quad \text{and} \quad T'_g = T_g \times n$$

The situation may, therefore, be modelled by the following equations:

$$T_{ad} = \dot{\omega}_{wt}(J_{wt} + J'_g) + T'_g \tag{3.1}$$

$$\text{and} \quad T'_g = k'\omega_{wt} \tag{3.2}$$

$$\Rightarrow \quad \frac{T'_g}{T_{ad}} = \left(\frac{\omega_{wt}}{\dot{\omega_{wt}}(\frac{J_{wt}+J'_g}{k'}) + \omega_{wt}} \right) \tag{3.3}$$

Taking transforms of (3.3) gives:

$$\frac{T'_g}{T_{ad}} = G(s) = \left[\frac{1}{1 + s(\frac{J_{wt}+J'_g}{k'})} \right] \tag{3.4}$$

$$\Rightarrow \quad G(j\omega) = \left[\frac{1}{1 + j\omega(\frac{J_{wt}+J'_g}{k'})} \right] \tag{3.5}$$

It can be seen from the transfer function that the system behaves like a simple first order low-pass filter with time constant (τ) and breakpoint frequency(f_b) as shown in (3.6) and (3.7):

$$\tau = \frac{J_{wt} + J'_g}{k'} \tag{3.6}$$

$$\text{and} \quad f_b = \frac{k'}{2\pi(J_{wt} + J'_g)} \tag{3.7}$$

Now:

$$T'_g = k'\omega_t \quad \text{and} \quad P_g = \omega_{wt}T'_g = k'\omega_{wt}^2$$

$$\Rightarrow \quad k' = \frac{P_g}{\omega_{wt}^2} \tag{3.8}$$

where $P_g =$ Generator Load Power (Watts)

To estimate the highest likely breakpoint frequency of the WT assembly (f_b), and hence the required bandwidth of the WTE, it was necessary to find the highest value of k' that the referred load would exhibit. This occurs at high power values, so to maximise the estimate, a high wind velocity and a relatively low TSR was chosen. A TSR of 0.3, corresponding to a C_p value of 0.29, and a wind velocity of $12\,ms^{-1}$ were considered suitable. At these values, assuming an air density of $1.22\,kgm^{-3}$, the average power, (P_{rotor}) is found by substituting into (2.1) as follows:

$$P_{rotor} = \frac{1}{2}\rho A V_w^3 C_p(\lambda) = 0.5 \times 1.22 \times 2 \times 12^3 \times 0.29 = 611\,W \tag{3.9}$$

Using the corresponding value for angular velocity, system stiffness (k) is established. Subsequently, using values for the WT and generator moments of inertia, f_b may be calculated:

$$\omega_{wt} = \frac{\lambda V_w}{R} = \frac{0.3 \times 12}{0.7} = 5.14\,rads^{-1}$$

$$\Rightarrow \quad k' = \frac{611}{5.14^2} = 23.13\,Nmsrad^{-1} \tag{3.10}$$

$$\Rightarrow \quad f_b = \frac{23.13}{2\pi \times (J_{wt} + J'_g)}$$

From Table 3.1, $J_{wt} =$ $2.02\,kgm^2$

and Table B.1 $J'_g =$ $0.0238 \times 8.3^2 = 1.64\,kgm^2$ so that:

$$f_b = \frac{23.13}{2\pi \times (2.02 + 1.64)} = 1.01\,Hz \tag{3.11}$$

Under these conditions the fundamental blade input torque frequency is 9.8 Hz so output is attenuated by approximately 20 dB.

3.2 WTE System Requirements and Implementation

Figure 3.9, shows the required WTE system and programmable load system inputs and outputs. The WTE system produces a mechanical output based on a CFD/Turbine model of the WT behaviour and supplied wind velocity data. Mechanical system measurands are fed back to enable closed loop control of the emulation process. The WTE is coupled to a programmable electrical load that was designed and built to facilitate this work, whose characteristics may be varied in real time. To facilitate data logging and display during 'test runs' electrical and mechanical signals are made available to the WTE system.

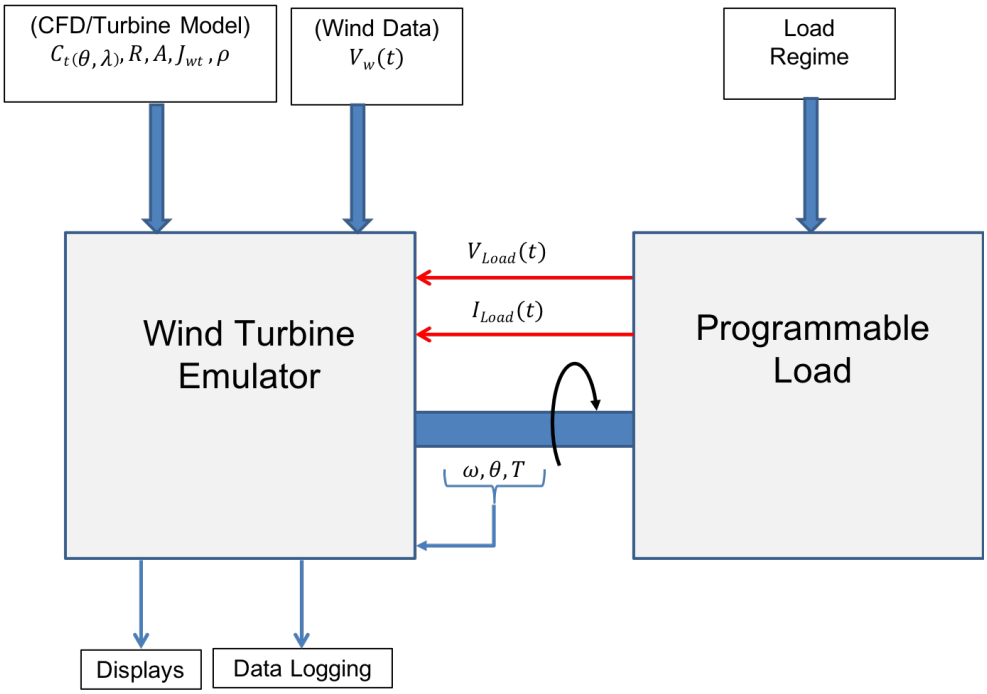

Figure 3.9: WTE and Programmable Load Inputs and Outputs

3.2.1 System Inputs

Wind velocity input values may be provided to the WTE as follows:

- A real time value based on a suitably conditioned analogue input.
- A real time value based on a virtual control.

The use of an analogue input facilitates convenient control of the system via a potentiomenter. It also has the potential for near-real-time data from an operational WT to be streamed for comparison purposes. The virtual control permits system operation directly from a user interface. The input wind velocity range is matched to the design constraints of the emulated device.

The frequency response of the WT to aerodynamic input torque sets an upper limit on the bandwidth requirement of the 'torque coefficient' model of the WT behaviour. It can be seen by inspection of Figure 3.3, showing aerodynamic torque variation with rotor position, that two main harmonic components are present. A 'dc' or mean value and a harmonic related to blade-period. The same phenomenon is observed in graphs for the other TSRs. The average torque component is unattenuated by the low-pass filter effect of the WT, but the blade-period harmonic (12^{th} w.r.t. one revolution) is attenuated by a factor dependent on its frequency which, in turn depends on angular velocity. In the previous section, it was established that the highest frequency associated with dynamic blade torque variation is approximately $10\,Hz$ at which point the attenuation is $20\,dB$. It was decided, therefore, that the WTE frequency response should faithfully reproduce that of the emulated system up to at least $10\,Hz$. This ensures that spectral analysis techniques may be used to detect blade faults characterised by lower frequency components that are nevertheless, above the system breakpoint frequency.

3.2.2 Mechanical Outputs and Feedback Parameters

Torque is the controlled variable, so it was necessary to specify the range, accuracy and resolution of the required output. WTs are designed to operate at, or close to optimal TSR. For this device the CFD predicted optimal TSR was 0.47 so it would normally be operated in the TSR range (0.4 - 0.6). Average torque values were obtained for given wind velocities and TSRs by firstly using Figure 3.5 to obtain the Torque Coefficient at a given TSR. This value and the wind velocity were then substituted into (2.10). To obtain a 'high' estimate of the maximum torque required from the WTE, a wind velocity of $12\,ms^{-1}$ and a TSR of 0.3 was used to obtain an average value of $120\,Nm$. The gearbox ratio used was 1:8.3, so this corresponds to a value of $14.5\,Nm$ at the gearbox output.

The CFD model for control is based on the torque coefficient, which is a function of angular position (θ) and TSR (λ). TSR is a function of the first derivative of angular position w.r.t. time (angular velocity). It was also necessary to use torque compensation techniques to account for the difference in moments of inertia between the WT rotor-generator to be modelled and the WTE motor-generator. This technique requires observation of the derivative of angular velocity w.r.t. time (angular acceleration). It was therefore necessary to accurately monitor angular position and angular velocity w.r.t. time. These process parameters were also made available for display and data logging purposes.

Angular velocity is not controlled so it was only necessary for the WTE to operate over the speed range of the emulated WT system. The WT being considered has a maximum angular velocity of 147 rpm (based on a V_w of $12\,ms^{-1}$ and a TSR of 0.9). It is a relatively low speed, high torque, device requiring a gearbox to match its output to the generator. High torque servomotors, capable of operating at low speeds, have high power ratings and therefore require high power rated drives. The rating of such a setup would not be well

matched to the WT to be emulated and the costs would be unnecessarily high; however, gearbox emulation in software is used to avoid this difficulty. This technique facilitates the emulation of a range of WTs from high-solidity low speed types through to low-solidity high-speed devices using the same, appropriately rated, servomotor system.

3.2.3 Electrical Control and Load Signals

System stiffness (k), associated with the mechanical load attached to the WTE output shaft is controlled separately via the programmable electrical load. Devolved control reduces the complexity of the WTE system and increases flexibility. Electrical load voltage and current signals are conditioned within the programmable load and fed back to the WTE for instrumentation and data-logging purposes. Full details of the programmable load design and implementation can be found in Appendix B.

3.2.4 Displays and Data Logging

A user interface is provided for control of the WTE and to view all relevant measurands and derived quantities during WTE operation. The facility to carry out data-logging related to test runs is provided. The LabVIEW^{TM} front panel interfaces providing this functionality may be viewed in Appendix C.

3.3 WTE Hardware Design

To meet the required functionality the following equipment was sourced:

- An Emerson Servomotor and Drive System
- A Real Time National Instruments (NI) LabVIEW^{TM} Development System comprising:
  - A Windows PC running the LabVIEW^{TM} application.
  - A PC running a NI Real Time Operating System (RTOS).
  - Two NI PCI-6229 Data Acquisition Cards (DAQ).
  - Two NI Signal Conditioning Boards (SCB68).

Relevant specifications are provided in Tables A.1, A.2 and A.3, which may be found in Appendix A.

The chosen servomotor has power, torque and speed ratings of $2.26\,kW$, $10.8\,Nm$ and $2000\,rpm$ respectively. From Subsection 3.2.2 the maximum values of torque and speed required from the WTE are $120\,Nm$ and $147\,rpm$ respectively. These do not occur at the same time. Emulating the 1:8.3 gearbox ratio in software means the servomotor must be able to deliver corresponding torque and speed values of up to $14.5\,Nm$ and $1223\,rpm$. The torque figure exceeds the continuous rating, but is below the peak torque rating of $18.7\,Nm$. This is acceptable because, as the system accelerates, torque falls rapidly with increasing TSR. The speed requirement is well within the range of the servomotor which is equipped with an integral encoder that provides angular position feedback with a resolution of $\pm\,0.088°$. The drive, described in Table A.2, provides facilities for implementing applications requiring accurate position, speed, acceleration and torque control together

with appropriate signalling interface features.

The LabVIEW^{TM} based WTE system uses two NI data acquisition cards (described in Table A.3) installed on two separate platforms. One provides the interface between the Drive and the WTE application running on the Real-Time (RT) PC. The other is associated with instrumentation and data capture on the Windows Host PC.

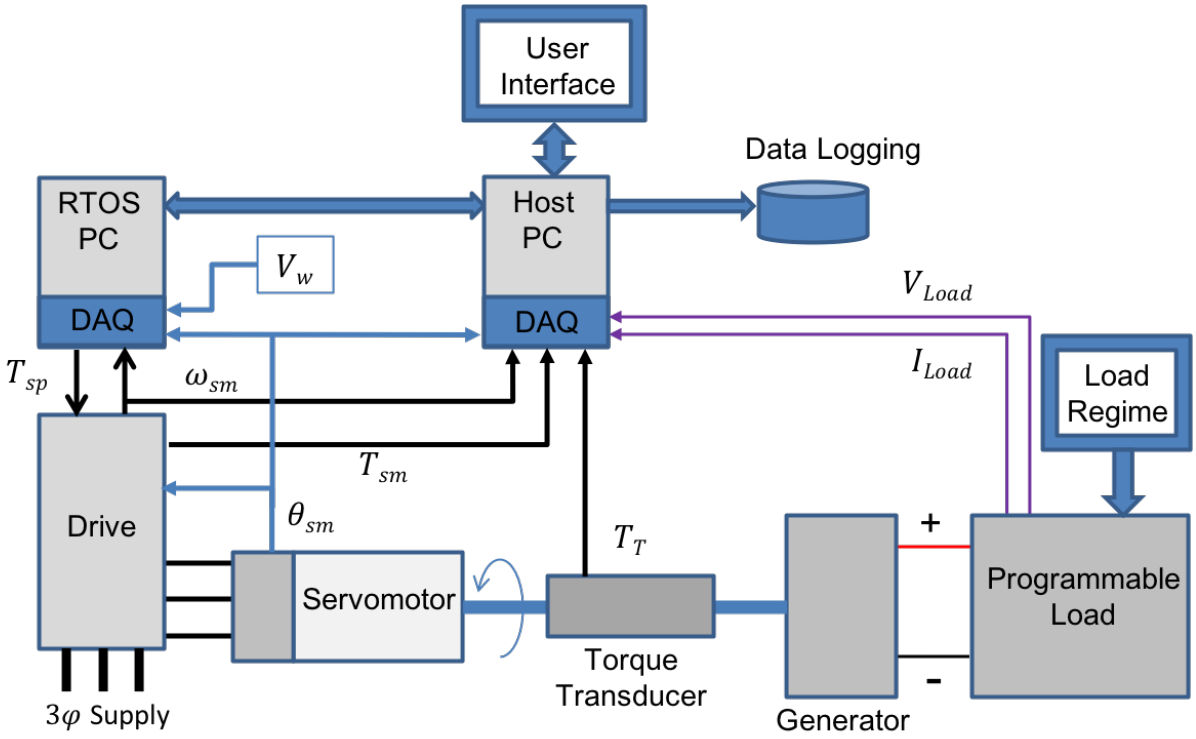

Figure 3.10: WTE and Programmable Load Schematic Diagram

A schematic representation of the physical setup is shown in Figure 3.10. A CFD aerodynamic model, together with the associated WT and gearbox parameters, is provided via the Host PC User Interface. The parameters are processed and downloaded to the RT WTE application running on the RTOS PC which, by monitoring wind velocity (V_w), angular position (θ) and angular velocity (ω), calculates the instantaneous aerodynamic torque on

the WT to be emulated. A varying torque setpoint (T_{sp}), representing the WT gearbox output, is then derived for the drive/servomotor control subsystem. The drive operates in high-speed 'torque mode' with output torque being estimated by a real-time software model monitoring line currents, angular position and angular velocity. The accuracy and loop time for the drive torque control are specified in Table A.2. Signals from the drive, the motor encoder and the load are fed back via the DAQ cards installed in the RTOS and Host PCs. This data may be monitored via the user interface or captured for analysis. Signals provided to the RTOS PC, relate to the real-time control process. Signals provided to the Host PC are for instrumentation data logging and subsequent offline analysis. The motor encoder output is normally supplied directly to the drive; however, the RT LabVIEW^{TM} application also utilises this signal. To facilitate this it was necessary to design and build an RS485 interface with optical isolation to relay the encoder A, B and Z signals.

3.4 LabView Software Design for WTE

The WTE application uses the Host-Target arrangement shown in Figure 3.10. The Real-Time (RT) program, which is capable of running autonomously on the RT platform, controls the WTE system. The Host program, running on a Windows machine, provides a User Interface (UI) for interaction with the RT Target facilitating parameter updates and the graphical display of process data. The Host program is also used to collect analogue process data, for off-line analysis, via its own DAQ interface.

3.4.1 Real-Time Controller

In Chapter 2 it was shown that inertia compensation may be accomplished by using either an acceleration observer, or a torque observer and the associated algorithms were shown in Figures 2.12 and 2.13 respectively. The acceleration observer method was chosen for this

application due to the quality of available hardware. In order to implement the intrinsic dynamic characteristics of a WT, a torque coefficient (C_t) generation algorithm, which includes emulated rotor position data, has been used as the basis for RT control. Figure 3.11 illustrates the method and Table 3.2 provides a key to the parameters shown.

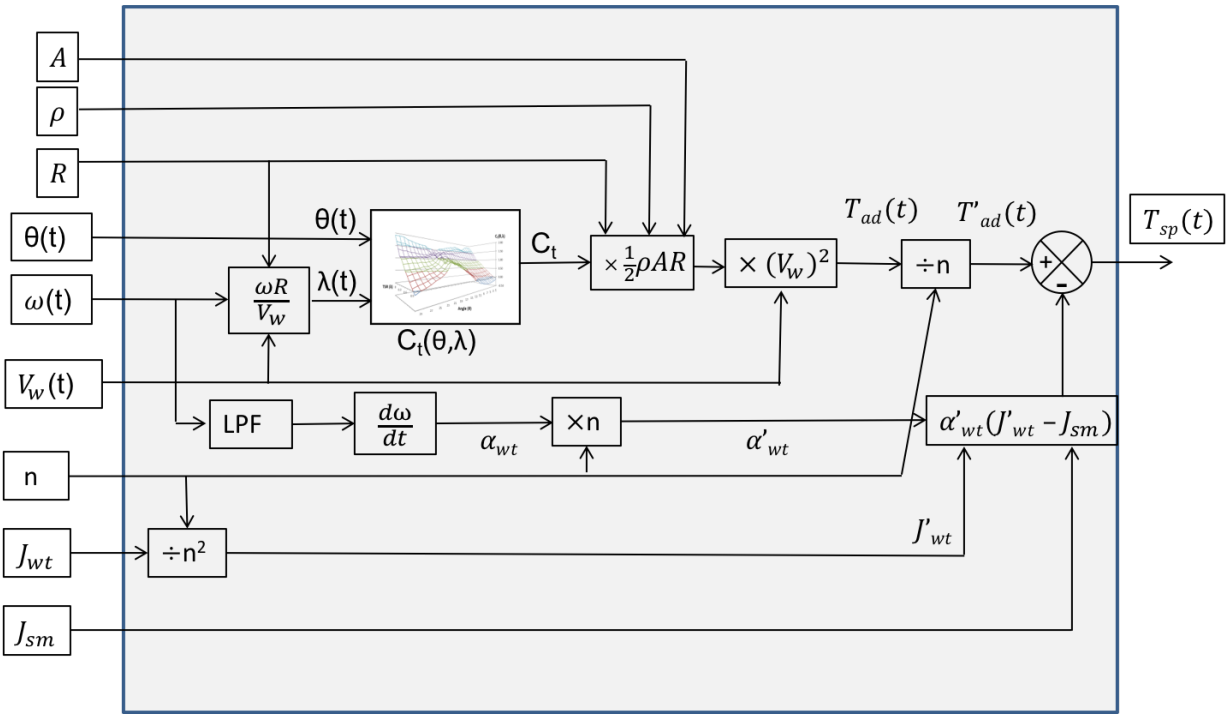

Figure 3.11: WTE Inertia Compensating Torque Setpoint Generation Algorithm

Torque Coefficient surface graphs, derived from CFD analyses, are used as the basis for dynamic WTE. For a particular WT, the characteristic graph ($C_t(\theta, \lambda)$) is passed into the program as a two-dimensional array. Within the array, rotor position data is provided at one-degree intervals from zero to three-hundred and sixty degrees inclusive. This facilitates interpolation in the final interval. TSR data is provided at intervals of 0.1 from zero through to one. The array, therefore, has dimensions (361×11). This is appropriate for the crossflow VAWT being used as the basis for the emulator design, however, the code may be altered to accomodate different WTs with higher TSRs. The array is used to 'look up' instantaneous torque coefficient values (C_t) based on current values for WT position

Table 3.2: Key to Parameters used in Figure 3.11

A	WT Aperture	(m^2)
ρ	Air Density	(kgm^{-3})
R	WT Radius	(m)
$\theta(t)$	WT Angular Position at time t	(deg)
$\omega(t)$	WT angular velocity at time t	$(rads^{-1})$
$V_w(t)$	Wind Velocity at time t	(ms^{-1})
n	Gearbox Ratio	
J_{wt}	WT Moment of Inertia	(kgm^2)
J_{sm}	Servomotor Moment of Inertia	(kgm^2)
J'_{wt}	WT Moment of Inertia (Referred to gearbox output)	(kgm^2)
$\lambda(t)$	WT Tip Speed Ratio (TSR) at time t	
$C_t(\theta, \lambda)$	2D-Array mapping $\theta(t)$ and $\lambda(t)$ to Torque Coefficient	
$\alpha_{wt}(t)$	WT angular acceleration at time t	$(rads^{-2})$
$\alpha'_{wt}(t)$	WT angular acceleration at time t (Referred to gearbox output)	$(rads^{-2})$
$T_{ad}(t)$	Aerodynamic Torque at time t	(Nm)
$T'_{ad}(t)$	Aerodynamic Torque at time t (Referred to gearbox output)	(Nm)
$T_{sp}(t)$	Torque Setpoint at time t	(Nm)

(θ) and TSR (λ). The torque coefficient is then used to calculate an instantaneous value for the driving aerodynamic torque on the WT (T_{ad}). Following inertia compensation and gearbox scaling, the resulting instantaneous torque value (T_{sp}) is passed, as a setpoint demand, to the motor-drive system.

The RT controller is a sampled system so algorithms for torque control and compensation must be translated into the z-domain. The servomotor-generator system can be modelled similarly to the WT system mentioned in Subsection 3.1.2. and adapting (3.1) and (3.2) yields:

$$T_{sm} = \dot{\omega}_g(J_{sm} + J_g) + k\omega_g \tag{3.12}$$

$$T_g = k\omega_g \tag{3.13}$$

$$\Rightarrow (T_{sm} - T_g) = \dot{\omega}_g(J_{sm} + J_g) \tag{3.14}$$

where:

T_{sm} = Servomotor Electromagnetic Torque (Nm), T_g= Generator Electromagnetic Torque (Nm), J_{sm} = Servomotor Moment of Inertia (kgm^2), J_g = Generator Moment of Inertia (kgm^2), k = Load coefficient ($Nmsrad^{-1}$), ω_g = Generator Angular Velocity ($rads^{-1}$) and $\dot{\omega}_g$ = Generator Angular Acceleration ($rads^{-2}$)

Equation (3.14) leads to the s-domain block diagram representation shown in Figure 3.12:

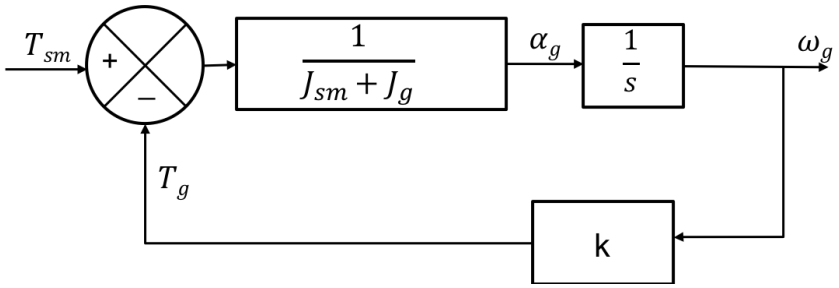

Figure 3.12: Servomotor-Generator s-domain Block Diagram

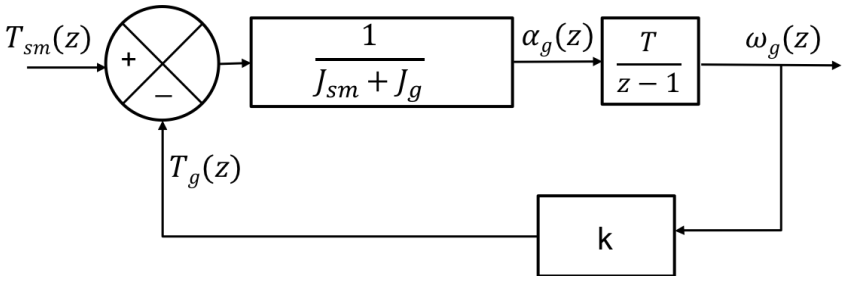

Figure 3.13: Servomotor-Generator Sampled System Block Diagram

The equivalent sampled system diagram is shown Figure 3.13 and the corresponding overall

z-domain transfer function is given by (3.15):

$$H(z) = \frac{\omega_g(z)}{T_{sm}(z)} = \frac{T}{J_{sm} + J_g}\left[\frac{1}{z + \left(\frac{kT}{J_{sm}+J_g} - 1\right)}\right] \tag{3.15}$$

where T is the sampling time of the system.

Incorporating the above transfer function in the forward path, and placing the inertia compensation block in a feedback path, yields the block diagram shown in Figure 3.14. For clarity, the total WT system moment of inertia, referred to the gearbox output, $(J'_{wt} + J_g)$ has been replaced by the term J'_T. The total servomotor system moment of inertia $(J_{sm}+J_g)$ has been replaced by the term J_S.

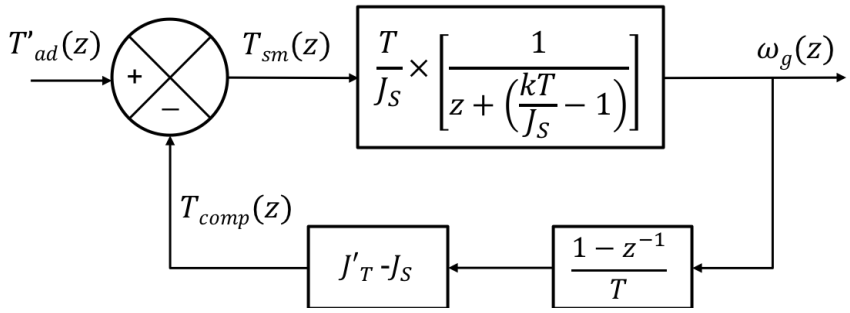

Figure 3.14: Torque Compensation Sampled System Block Diagram

The resulting transfer function is given by:

$$H(z) = \frac{zT}{J_S z^2 + (kT + J'_T - 2J_S)z + (J_S - J'_T)} \tag{3.16}$$

Performing a w-transform on the characteristic equation yields:

$$w^2\, kT + w\, 2J'_T + (4J_S - 2J'_T - kT) = 0 \tag{3.17}$$

Applying the Routh-Hurwitz criterion shows that, for stability, the following constraint

must be met:

$$(4J_S - 2J'_T - kT) > 0 \tag{3.18}$$

$$\Rightarrow \qquad J_S > \frac{J'_T}{2} + \frac{kT}{4} \tag{3.19}$$

The final term is normally negligible.

$$\Rightarrow \qquad \frac{J'_T}{J_S} < 2 \tag{3.20}$$

As WT systems have much larger moments of inertia than WTEs, this restriction must be overcome. It has been shown in [71] that the problem is due to the sample time delay and may be managed by using a Deviation Mitiation Filter (DMF) prior to the differentiator in the feedback path. The paper reviewed explains that differentiated noise in the feedback path does not cause instability. The resulting revised block diagram (with DMF coefficient α) is shown in Figure 3.15 and forms the basis of the torque compensation algorithm implemented by the RT control program.

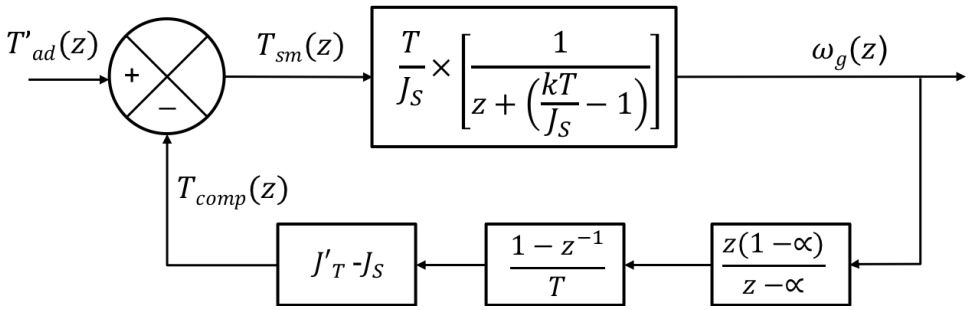

Figure 3.15: Torque Compensation Block Diagram with Deviation Mitigation Filter

The new transfer function is given by 3.21:

$$H(z) = \frac{(z-\alpha)T}{J_S z^2 + (kT + J'_T(1-\alpha) - 2J_S)z + (J_S - J'_T(1-\alpha) - \alpha\, kT)} \tag{3.21}$$

The requirements for stable operation are again determined by carrying out a bilinear transformation process and applying the Routh criteria. The condition is given by:

$$\frac{J'_T - 2\,J_S}{J'_T} < \alpha < 1 \tag{3.22}$$

The WTE algorithm is implemented within an RT loop running on the RT platform. A second RT loop deals with related instrumentation rather than control. Data acquisition tasks 'run' within both loops to acquire and transmit RT signals. To pass back process and related measurands to the Host, for display, it is necessary to 'relay' the data via a non RT loop. LabVIEW^{TM} code for the RT Controller can be found in Appendix C.

3.4.2 Host Application and User Interface

On startup the Host program initialises variables and waits until communication with the RT Controller is established. Relevant RT Controller parameters are then uploaded and a timed delay ensures that network variables have propagated. Following startup the Host executes the Finite State Machine (FSM) program outlined in Figure 3.16. Transitions due to user operation of screen pushbuttons are labelled PB.

Initially the WTE configuration is displayed, including the uploaded RT controller parameters. The user may then update or retain the parameters and confirm the choice. Numerical parameters are entered from the keyboard via a Front Panel interface. Front Panels visible to the user during program execution can be viewed in Appendix C. The 2-D array, representing $C_t(\theta, \lambda)$, is uploaded by choosing a tab-delimited file from a drop down

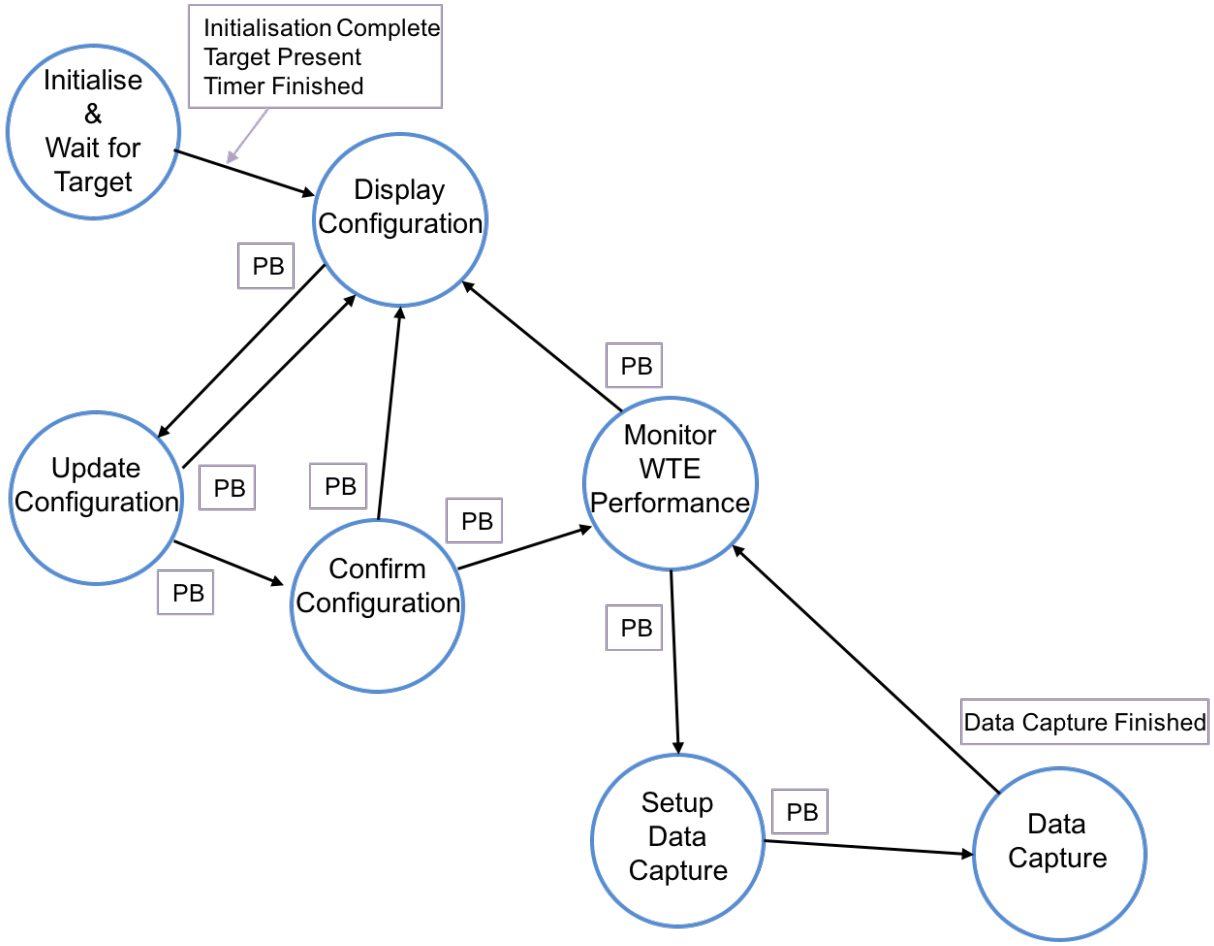

Figure 3.16: Host Application FSM Diagram

menu. Checks on data integrity are carried out before the user can confirm and download the configuration to the RT controller. Following confirmation the user may choose either to display the configuration again, or to monitor WTE system operation.

In monitoring mode virtual instruments panels display the following parameters graphically in near-real-time:

- Emulated WT Angular Velocity, Torque and Power.
- Servomotor Angular Velocity, Torque and Power.
- Compensation Torque.
- Generator Voltage, Current and Power.
- System Efficiency.
- Wind Velocity.
- Tip Speed Ratio.
- System Bandwidth.

These parameters are derived, directly or by calculation, from the data captured by the RT controller.

To capture process data, for offline analysis, the 'Setup Data Capture' mode is used. Here a target file, for data storage, and the capture time duration is specified. Files are created using the NI 'Technical Data Management Streaming' (TDMS) format and may be analysed directly using NI's DIAdem application. Any RT controller process variable is available for capture but only the following parameters are obtained in this way:

- Calculated Aerodynamic Torque.
- Emulated WT Output Torque.
- Emulated WT Angular Velocity.

To avoid indeterminacy issues with the network connection, the remaining process data is captured directly via the Host's separate data acquisition interface. The following parameters are obtained in this way:

- Generator Voltage.
- Generator Current.
- Generator Angular Velocity.
- Wind Velocity.
- Torque Transducer Output.
- Drive Torque Signal from RT controller.

When data capture is complete the user is returned to the Monitor screen.

LabVIEW code for the Host application can be found in Appendix C.

3.5 Summary

This chapter began with the development of a comprehensive requirements analysis for the proposed WTE system, based on a particular, complex, crossflow VAWT design. The hardware and software design processes and the resulting initial implementation of the

WTE were then presented. The resulting device used a standard 'acceleration observer' method for inertia compensation, however, initial system tests, described in Chapter 5, Subsection 5.2.1, demonstrate that the initial WTE system fails to meet the spectral response specification. The following chapter begins by providing a detailed analysis of the reasons for the inadequate spectral response and subsequently describes the development of a novel inertia-compensation scheme that yields the performance required.

Chapter 4

An Improved Moment of Inertia Compensation Scheme for WTE

4.1 Introduction

During initial system tests, a DMF coefficient value, giving smooth WTE operation, was established empirically. Substituting moment of inertia values for the servomotor, generator and emulated WT into (3.22) indicated that the filter coefficient (α) should be greater than 0.17 and less than 1. In practice, a minimum value of 0.95 was required. Furthermore, this had to be adjusted upwards with higher values of J_{wt}. According to the work presented in [71], noise in the feedback path does not cause instability and, provided the filter coefficient value is calculated as quoted the system will be stable. The problem, however, was not instability but 'noisy' operation. This only occurred at low speeds and low drive torque setpoint values suggesting quantisation noise may be the cause. In high-speed mode, the drive resolution for the angular velocity signal is 10-bit. The servomotor maximum speed rating is $3200\,rpm$, however, the drive allows some 'headroom' and allocates a range of $4000\,rpm$. The angular velocity quantisation noise in the feedback path has, therefore, an amplitude of approximately $\pm 2\,rpm$. At low speeds this is a relatively high value and differentiating this signal with inadequate low-pass filtering causes significant noise on the compensating torque signal. Increasing the DMF coefficient to deal with noise, conflicts

with the requirement that it should be as low as possible to maximise the frequency range over which torque compensation is effective. It is not feasible to increase the resolution provided by the drive for the angular velocity signal. The drive is capable of providing higher resolution, but this is achieved at the expense of an unacceptable increase in torque control loop time. This chapter presents the design of a novel solution which, in overcoming this problem, makes a contribution to knowledge.

4.2 Analysis

The transfer function of the emulated WT system, with total referred moment of inertia J'_T, is given by:

$$H(z) = \frac{T}{J'_T}\left[\frac{1}{z - \left(1 - \frac{kT}{J'_T}\right)}\right] \tag{4.1}$$

For the particular case where: $T = 5\,ms$, $J'_T = 0.048\,kgm^2$ and, $k = 0.0714\,Nmsrad^{-1}$ the transfer function is:

$$H(z) = \frac{T}{J'_T}\left[\frac{1}{(z - 0.9926)}\right] \tag{4.2}$$

The transfer function for a WTE with inertia compensation using a DMF is:

$$H(z) = \frac{T(z - \alpha)}{J_S z^2 + (kT + J'_T(1 - \alpha) - 2J_S)z + (J_S - J'_T(1 - \alpha) - \alpha\, kT)} \tag{4.3}$$

If the total moment of inertia for the emulator system is J_S and the previous parameters are substituted, the particular transfer function is:

$$H(z) = \frac{T}{J_S}\left[\frac{(z - 0.95)}{(z - 0.8690)(z - 0.9931)}\right] \tag{4.4}$$

The dominant pole is close to the WT system pole but the transfer function includes an extra pole and zero. It is the presence of a zero, with a breakpoint frequency within the required operating range, that is the cause of poor performance. A matching low-pass filter in the T_{ad} signal path could eliminate this zero but would introduce inaccuracy into the response. If the dominant pole can be manipulated to take the same position as that of the original WT system, however, the other pole will take up a position determined only by J_T, J_S, and the DMF filter coefficient (α). This would allow an adaptive lag-lead pre-filter to be placed in the T_{ad} signal path and the accuracy of the response to be maintained. The filter would take the form:

$$F(z) = \frac{J_S}{J'_T}\left(\frac{z-\beta}{z-\alpha}\right) \tag{4.5}$$

where: α = DMF Coefficient and, β = Pole position to be calculated.

Placing this filter in the T_{ad} signal path, prior to torque compensation, gives the following overall transfer function:

$$H(z) = \frac{J_S}{J'_T}\left(\frac{z-\beta}{z-\alpha}\right) \times \frac{T}{J_S}\left[\frac{(z-\alpha)}{(z-\beta)(z-p_R)}\right] \tag{4.6}$$

$$= \frac{T}{J'_T}\left[\frac{1}{(z-p_R)}\right] \tag{4.7}$$

where: p_R = Required Pole Position = $\left(1-\frac{kT}{J'_T}\right)$

Since $H(1)$ must always be the reciprocal of k then:

$$F(1) = \frac{J_S}{J'_T}\left(\frac{z-\beta}{z-\alpha}\right) = 1 \tag{4.8}$$

$$\Rightarrow \beta = 1 - \frac{J'_T}{J_S}(1-\alpha) \tag{4.9}$$

The application of the pre-filter described relies on correct adjustment of the dominant pole position. To correct the dominant pole position and implement the required lag-lead pre-filter, an algorithm was developed and implemented in LabVIEW code. This can be viewed in Appendix C. Developing a z-domain adjustment algorithm, based on an altered value for J'_T, is particularly complex, so an s-domain approximation model was was used.

4.3 Algorithm Development

The s-domain WT system transfer function, with total referred moment of inertia (J'_T), is given by:

$$H(s) = \frac{\omega(s)}{T_{ad}(s)} = \frac{1}{k}\left[\frac{1}{1 + s\left(\frac{J'_T}{k}\right)}\right] \tag{4.10}$$

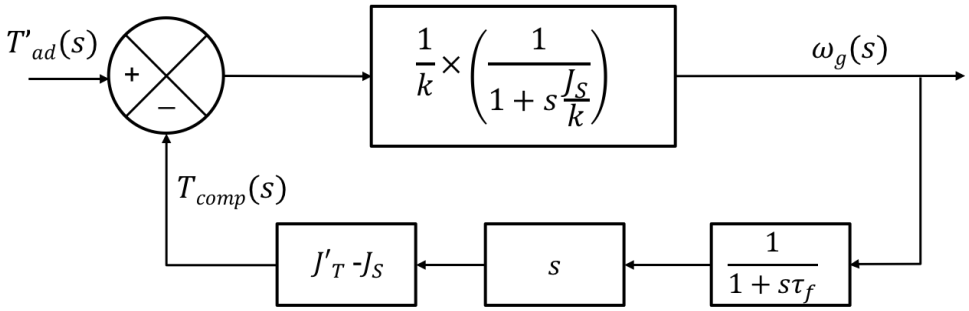

Figure 4.1: WTE s-domain Equivalent Model

The transfer function for the corresponding emulating system differs only in the moment of inertia value and inertia compensation is achieved by incorporating it into the control loop shown in Figure 4.1. This results in the transfer function given by:

$$H(s) = \frac{1}{k}\left[\frac{1 + s\tau_f}{s^2\left(\frac{J_S\tau_f}{k}\right) + s\left(\frac{\tau_f k + J'_T}{k}\right) + 1}\right] \tag{4.11}$$

If the s^2 coefficient is neglected, the system approximates to a first-order system with time constant given by the s coefficient. Comparing this with the s coefficient from (4.10), it can be seen that the time constant is overestimated by the low-pass filter time-constant (τ_f) value. Pole position correction, however, must take account of the s^2 coefficient as simply subtracting $\tau_f\, k$ from the value used for J'_T in the feedback path, results in overcompensation. The characteristic equation is quadratic and may be solved using the classic formula:

$$s_p = \frac{-b \pm \sqrt{b^2 - 4ac}}{2a} \tag{4.12}$$

where: $a = \left(\frac{J_S \tau_f}{k}\right)$, $b = \left(\frac{\tau_f k + J'_T}{k}\right)$ and $c = 1$.

It is required to adjust the value of b so that when the numerator is divided by $2a$ the correct least-negative root is obtained. The a-term is a constant, since it is unaffected by changes to J'_T. The c-term is also constant, with a value of one. The top line of this formula may be interpreted trigonometrically in order to correct the least negative pole position. Figure 4.2 illustrates the method and uses the following parameters:

- b_r = The required value for correct root placement.
- $\Delta\, b$ = The reduction in b necessary to achieve b_r.
- $y_1 = -b + \sqrt{b^2 - 4a}$ = Current Root $\times\, 2a$.
- y_2 = Required Root $\times\, 2a = \frac{-k}{J_T} \times 2a$.

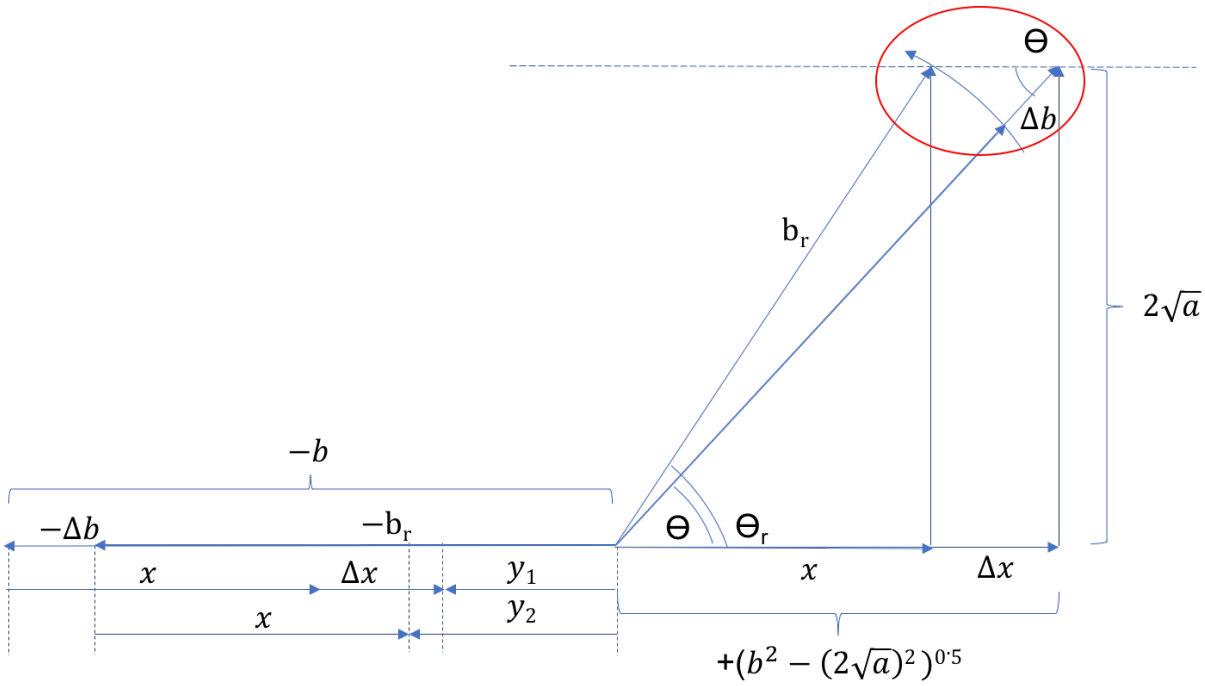

Figure 4.2: Trigonometric Model for Pole Compensation

From Figure 4.2:

$$\Delta b = \Delta x + (y_1 - y_2) \tag{4.13}$$

The shape within the red circled area approximates to a right-angled triangle with hypotenuse Δx and adjacent Δb so:

$$\Delta x \approx \frac{\Delta b}{cos\theta} \tag{4.14}$$

$$\Rightarrow \Delta b \approx \frac{(y_1 - y_2)}{(1 - \frac{1}{cos\theta})} \tag{4.15}$$

The value of Δb obtained is an overestimate since the opposite side of the 'triangle' is slightly curved. By repeating the process, however, successive values for Δb_n may be obtained. The sum of these may be used to obtain the required value for b_r. To achieve root

position adjustment the final 'summed' value for Δb is multiplied by k and subtracted from the value used for J'_T in the feedback path.

The method was applied to the s-domain model using the parameters that yielded (4.1) above. The required root value is $-1.4875\,s^{-1}$ and before adjustment the actual value is $-1.3033\,s^{-1}$. Following the first iteration the value obtained was $-1.4995\,s^{-1}$. After the second, final, iteration the value calculated was $-1.4875\,s^{-1}$.

The results of the above s-domain calculation where then applied to the z-domain model giving the following particular transfer function.

$$H(z) = \frac{T}{J_S}\left[\frac{(z-0.95)}{(z-0.880)(z-0.9925)}\right] \tag{4.16}$$

The required root value 0.9926, seen in (4.2), is closely matched. The other root has also moved to the 'correct' position since substituting for J'_T J_S and α in (4.8) gives:

$$\beta = 1 - \frac{0.048}{0.02}(1-0.95) = 0.880 \quad \text{As required.} \tag{4.17}$$

Applying the pre-filter specified in (4.5) gives the overall transfer function:

$$H(z) = \frac{J_S}{J'_T}\left(\frac{z-0.880}{z-0.95}\right) \times \frac{T}{J_S}\left[\frac{(z-0.95)}{(z-0.880)(z-0.9925)}\right] \tag{4.18}$$

$$= \frac{T}{J'_T}\left[\frac{1}{(z-0.9925)}\right] \tag{4.19}$$

The s-domain model is an approximation of z-domain behaviour so, to ensure algorithm

validity, over the range of system stiffnesses (k) and moments of inertia (J'_T) to be used, a spreadsheet was constructed. This can be found in Appendix D and demonstrates that, following two iterations of the correction method, the pole is successfully corrected to within 2% of its required distance from the unit circle.

4.4 Implementation

The modified WTE inertia compensation algorithm requires the calculation of the 's' and 's^2' coefficients from (4.11) within successive control loop sample periods. The relevant parameters are; J'_T, J_S, τ_f and k. The moment of inertia data (J'_T and J_S) are program constants. The equivalent DMF s-domain time constant (τ_f) is calculated from the current DMF coefficient (α) and the system sample time value (T_s). The DMF coefficient is also used, with moment of inertia data, to calculate the pre-filter denominator coefficient (β). System stiffness (k) is a real-time variable observed by monitoring generator voltage (V_g) and current (I_g) to calculate instantaneous load resistance. The square of the generator machine constant (K_m^2) is divided by the total electrical resistance, including generator armature resistance (R_a), to obtain the electromagnetic stiffness. The generator is subject to rotational resistance or 'windage' (k_{wind}) which is also taken into account.

Figures 4.3, - 4.5 show the algorithm implementation and Table 4.1 provides a key to the parameters used. Figure 4.3 is an overview detailing the additional functionality provided, including the system stiffness observer and the pre-filter. Figure 4.4 shows in more detail how the torque compensation value is calculated. It can be seen that three parameters are generated. The s^2 coefficient (a) and the reciprocal of the required s coefficient ($\frac{1}{b_r}$) are used repeatedly with successive pole adjustment iterations. The uncompensated s coefficient (b_U) is passed into each pole adjustment routine and a compensated version

(b_{cn}) is passed out to be used in subsequent iterations. At each iteration an adjustment (Δb_n) to the input 'b-value' is passed out. The sum of such adjustments, for the iterations used, are multiplied by the system stiffness (k) to generate an adjustment to the J'_T value used for inertia compensation. Figure 4.4 shows the pole adjustment algorithm.

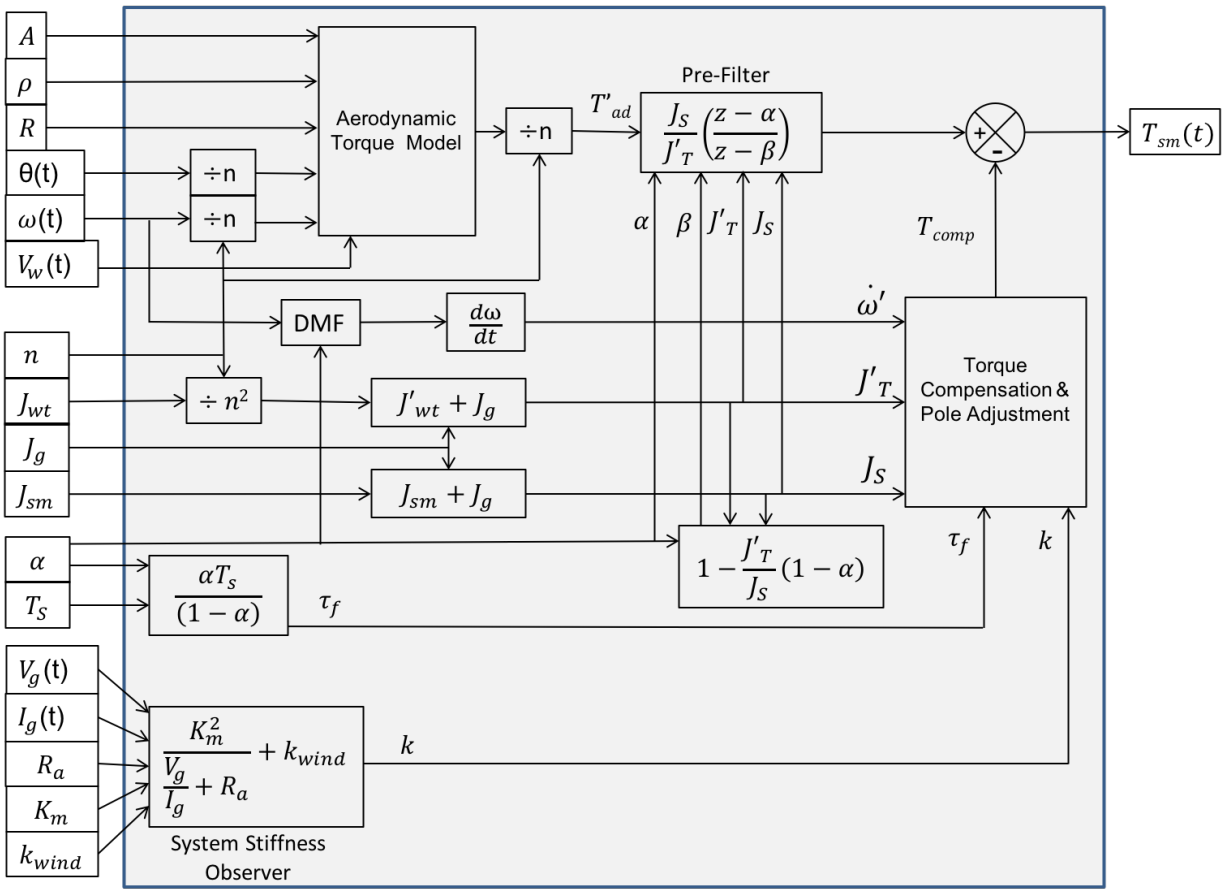

Figure 4.3: Modified WTE Inertia Compensation Algorithm

The corresponding LabVIEW code, developed to implement the algorithm depicted in Figures 4.3 - 4.5, can be found in Appendix C, Figures C.8 to C.11.

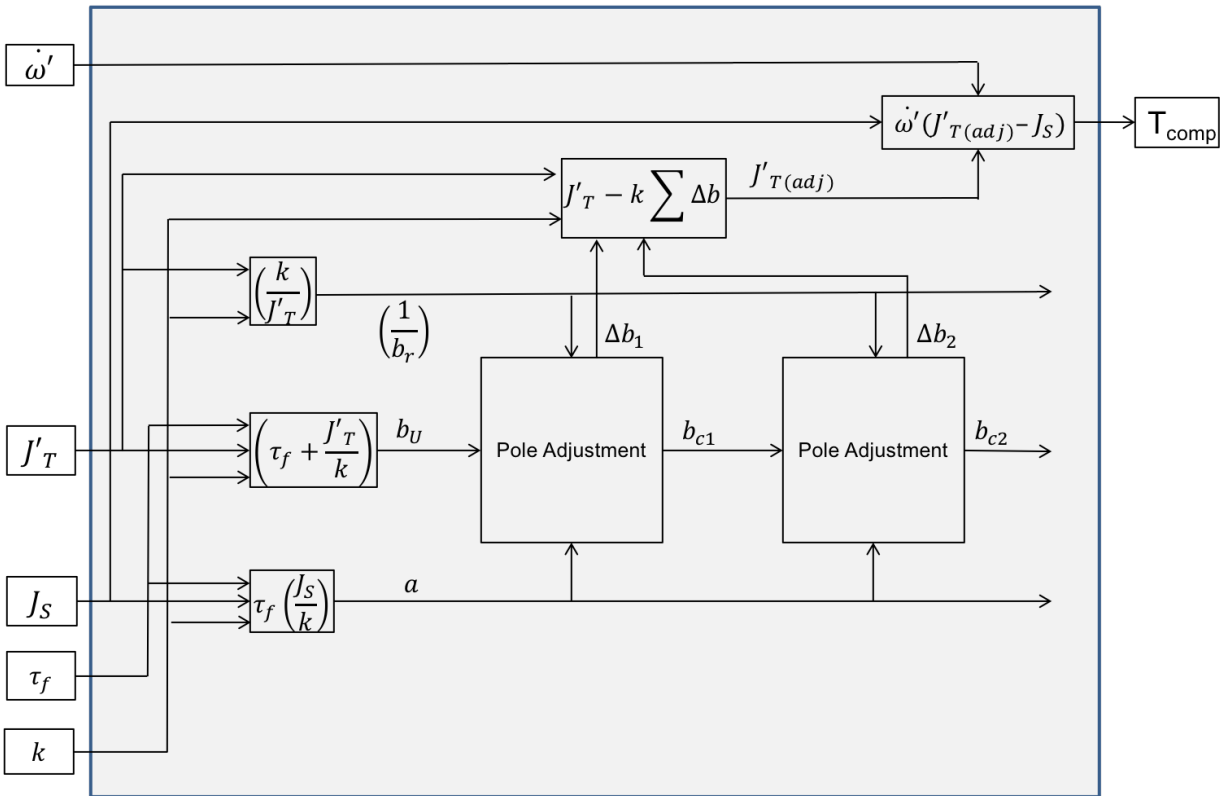

Figure 4.4: Torque Compensation and Pole Adjustment Algorithm

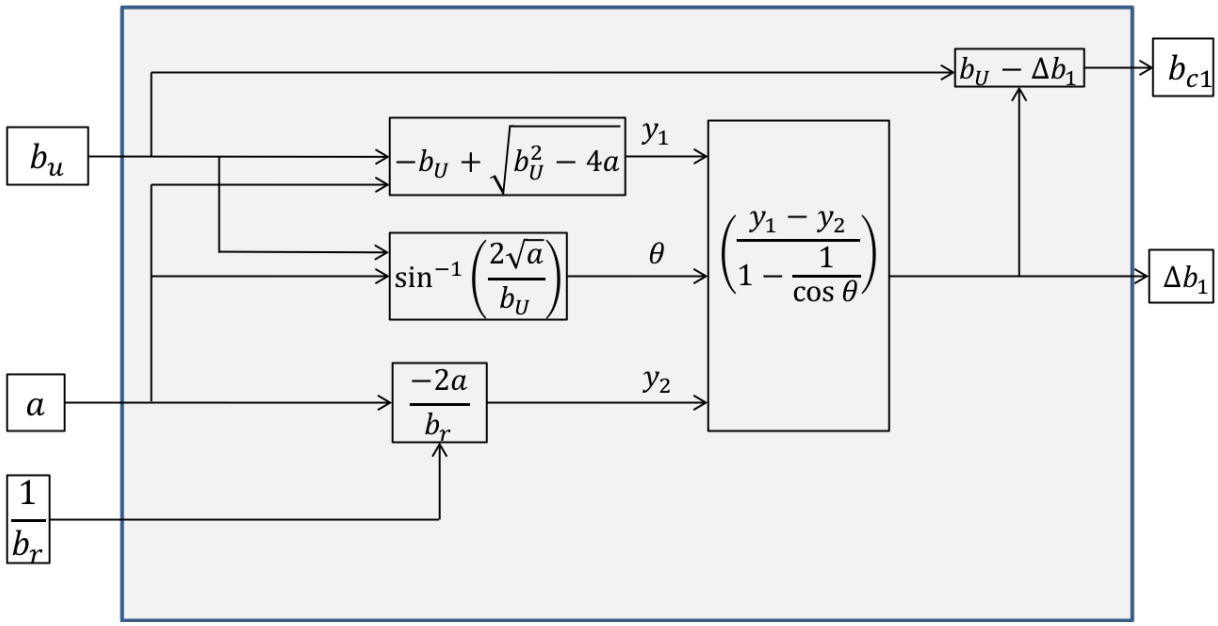

Figure 4.5: Pole Adjustment Algorithm

Table 4.1: Key to Parameters used in Figures 4.3, 4.4 and 4.5

A	WT Aperture	(m^2)
ρ	Air Density	(kgm^{-3})
R	WT Radius	(m)
$\theta(t)$	WTE Angular Position at time t	(deg)
$\omega(t)$	WTE angular velocity at time t	$(rads^{-1})$
$\dot{\omega}$	WT angular acceleration at time t	$(rads^{-2})$
$V_W(t)$	Wind Velocity at time t	(ms^{-1})
n	Gearbox Ratio	
J_{wt}	WT Moment of Inertia	(kgm^2)
J_g	Generator Moment of Inertia	(kgm^2)
J_{sm}	Servomotor Moment of Inertia	(kgm^2)
J'_T	WT Total Moment of Inertia (Referred to gearbox output)	$kgm^2)$
J_S	WTE Total Moment of Inertia	(kgm^2)
α	DMF coefficient	
β	Pre-Filter denominator coefficient	
T_S	System Sample Time	(s)
τ_f	s-domain filter time constant based on α	(s)
$V_g(t)$	Generator Voltage at time t	(V)
$I_g(t)$	Generator Current at time t	(V)
R_a	Generator Armature Resistance	(Ω)
K_m	Generator Machine Constant	$(Vsrad^{-1})$
k_{wind}	Generator Windage Constant	$(Nmsrad^{-1})$
k	System Stiffness	$(Nmsrad^{-1})$
$T'_{ad}(t)$	Aerodynamic Torque at time t (Referred to gearbox output)	(Nm)
T_{comp}	Compensating Torque	(Nm)
$T_{sm}(t)$	Torque Setpoint at time t	(Nm)
a	s^2 coefficient	(s^2)
b_U	Uncompensated s coefficient	(s)
b_r	Required s coefficient	(s)
b_{cn}	s coefficient following the n^{th} correction	(s)
$\Delta\, b_n$	Adjustment in b due to n^{th} adjustment	(s)

4.5 Summary

An analysis of the inadequate performance of the initial WTE system has been presented in this chapter, and the reasons for the poor frequency response of the system were determined. The design and implementation of a novel inertia-compensation scheme, to deal with the problems identified, was then set out. Section 5.2, of the following chapter, presents and compares the results of frequency response tests carried out firstly on the initial WTE system developed in Chapter 3, and secondly on an improved system using the new inertia compensation scheme. The remainder of Chapter 5 goes on to cover the further tests necessary to ascertain that the WTE performance specification is met and that it is thus suitable for its intended purpose.

Chapter 5

Results and Discussion

5.1 Introduction

In this chapter the results and analyses of the WTE system performance tests are set out and discussed. Tests relating to inertia compensation are covered first since the correct operation of this feature was necessary to ensure the validity of subsequent tests. Following this, investigations were carried out on the correctly compensated system, using WT CFD models for healthy and various faulted rotor configurations. The datasets obtained were used to perform two further sets of analyses. The first set was to confirm that mean torque and power generated by the WTE system were in accordance with the CFD models used. Secondly, comparative studies of dynamic WTE generator electrical output signals were used to explore their effectiveness for condition monitoring purposes.

5.2 Inertia Compensation

The WTE system was initially implemented using a standard method for Inertia Compensation based on an angular acceleration observer and a DMF as outlined in [71]. Performance tests on the initial system revealed that the frequency response was inadequate for the intended functionality of the WTE. An analysis was carried out and an improved method was devised as set out in Chapter 4. The method was implemented and the perfor-

mance tests were repeated. The test procedures and results for the standard and modified systems are presented below.

5.2.1 Standard Inertia Compensation Scheme

To test WTE performance quantitatively, the RT controller code was temporarily altered allowing the Aerodynamic Torque (T_{ad}) parameter to be driven directly from an analogue input. The gearbox ratio was set to the default value of 1:8.3, and the Programmable Load was configured to provide a total resistance (including generator armature resistance) of $0.6\,\Omega$. A signal generator was then used to apply step inputs and a range of sinusoidal inputs from $0.05\,Hz$ to $10\,Hz$ inclusive. In each case the corresponding generator angular velocity signal was recorded. For the sinusoidal tests, frequency was incremented from $0.05\,Hz$ to $0.1\,Hz$, then in steps of $0.1\,Hz$ from $0.1\,Hz$ to $1\,Hz$ and in steps of $1\,Hz$ thereafter. The tests were repeated for each of the following situations:

- No Inertia Compensation (Uncompensated).
- Compensation for $J_{wt} = 2.02\,kgm^2$.
- Compensation for $J_{wt} = 13\,kgm^2$.

In every case the signal generator was set up so that Aerodynamic Torque values, within the program, took maximum and minimum values of $33\,Nm$ and $8\,Nm$ respectively. All test data was captured and processed using DIAdem [72]. For the step tests, DIAdem was used to remove the offset and normalise the responses. Frequency response data was also extracted using DIAdem before being processed in Microsoft Excel to generate amplitude Bode plots. The results are summarised in Figures 5.1 and 5.2.

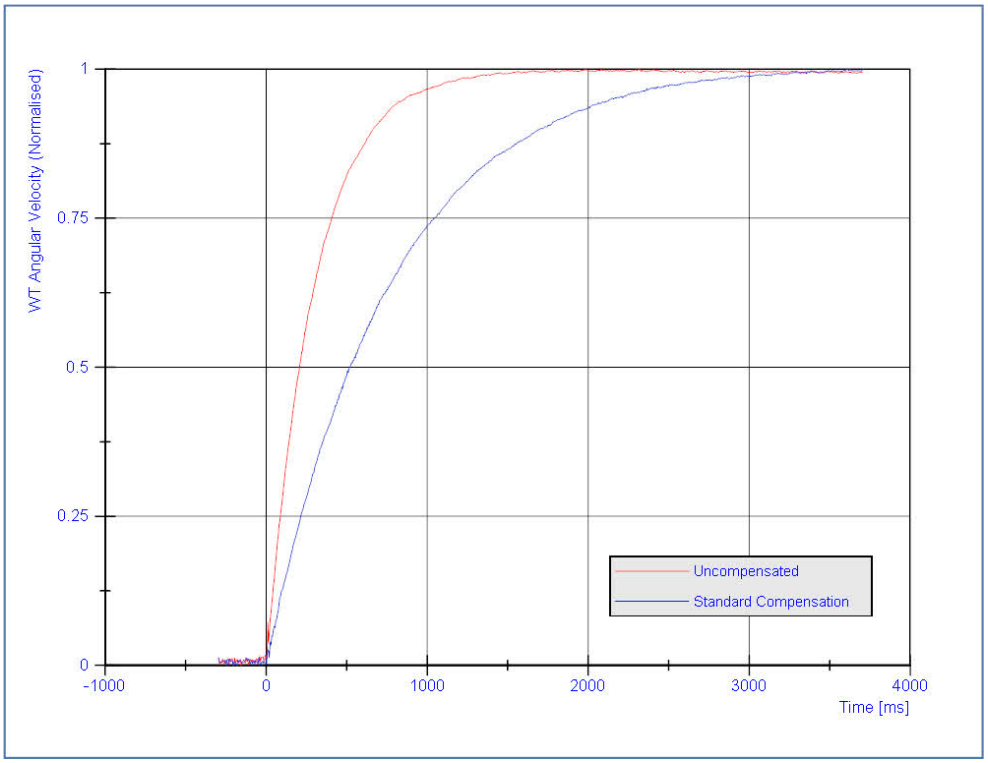

(a) Uncompensated and Standard Compensation with $J_{wt} = 2.02\,kgm^2$

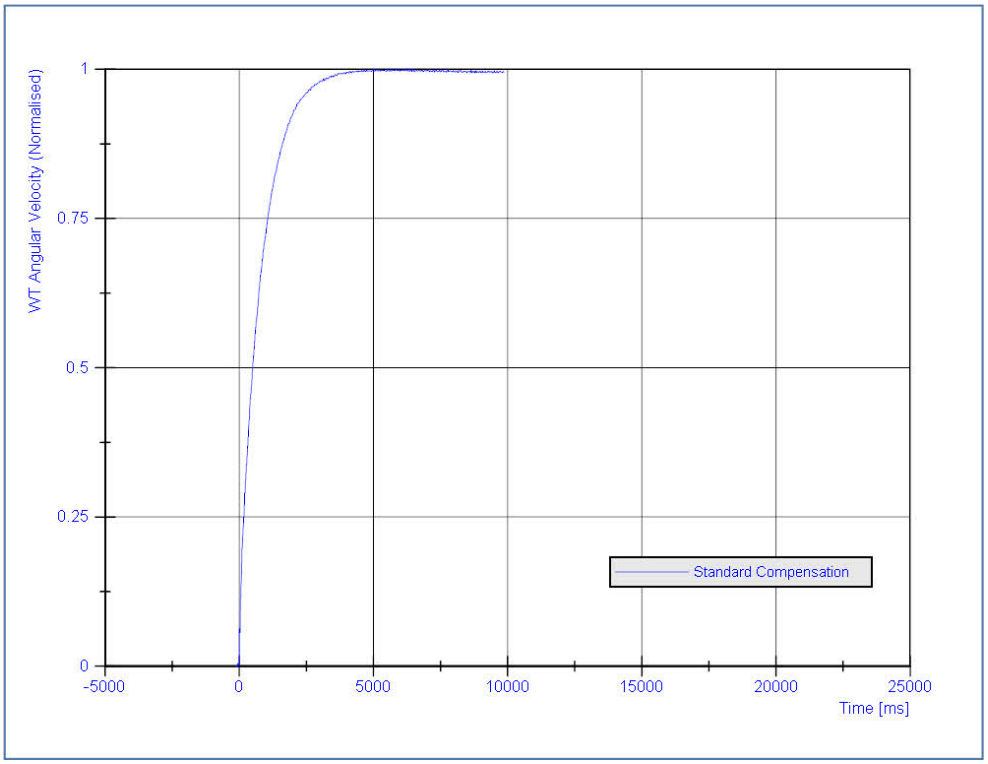

(b) Standard Compensation with $J_{wt} = 13\,kgm^2$

Figure 5.1: WTE Step Responses to Differing Emulated WT Moments of Inertia

The theoretical time constant, for each case, is obtained using the following formula:

$$\tau = \frac{J'_T R}{k_m^2} \tag{5.1}$$

where:

τ = Time Constant (s), J'_T = Total WT System Moment of Inertia (kgm^2),

R = Total Load Resistance (Ω) and, k_m = Generator Constant ($Vsrad^{-1}$)

The total moment of inertia (J'_T) is obtained by adding the generator moment of inertia (J_g) to the driving system moment of inertia. In the uncompensated case this is simply the sum of the servomotor and generator moments of inertia. In the emulated cases, J_g is added to the emulated WT moment of inertia (J_{wt}) referred to the gearbox output shaft.

Table 5.1 shows the result of these calculations and compares them to the actual values obtained. The uncompensated step response is exactly as predicted and gives confidence that the motor-drive setup does not introduce any significant delay to the control loop forward path. The performance for the lower value of J_{wt} is close to the predicted behaviour with a time constant about 5% longer than the calculated value. The performance for the higher value of J_{wt}, however, is completely inadequate with a time constant 72% shorter than required.

Table 5.1: Comparison of Intended and Actual WTE System Time Constants

	J'_T (kgm^2)	τ_{calc} (ms)	τ_{meas} (ms)	τ_{error} (%)
Uncompensated	0.02	300	300	0.0
$J_{wt} = 2.02\,kgm^2$	0.048	720	755	4.9
$J_{wt} = 13\,kgm^2$	0.208	3116	880	−71.8

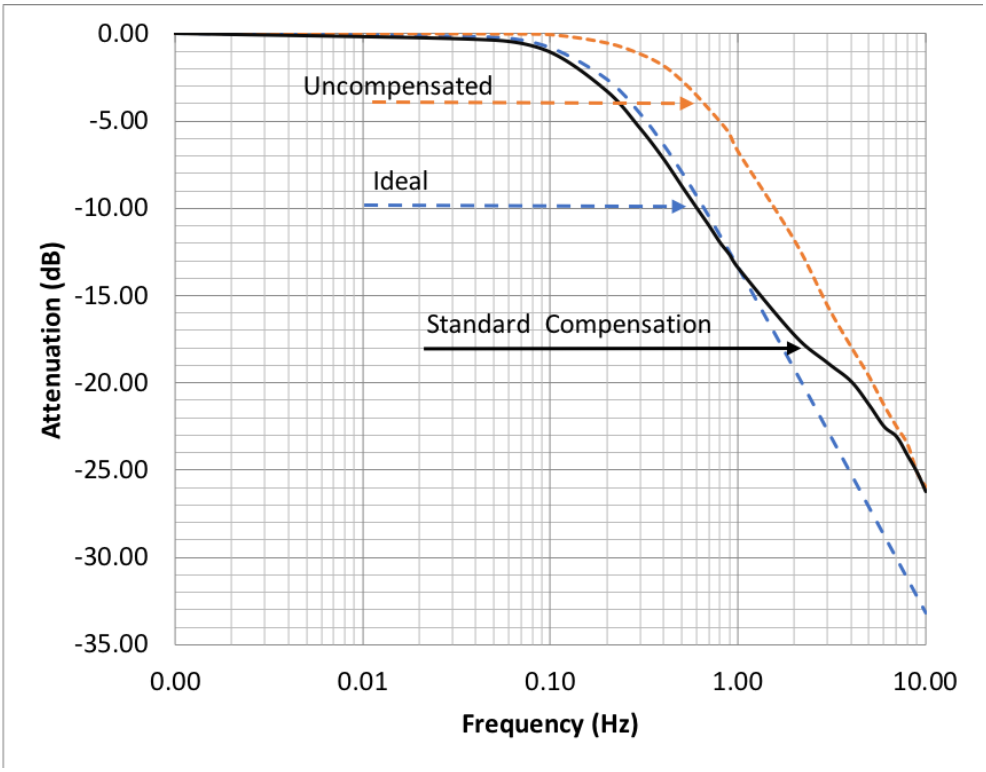

(a) Standard Compensation with $J_{wt} = 2.02\,kgm^2$

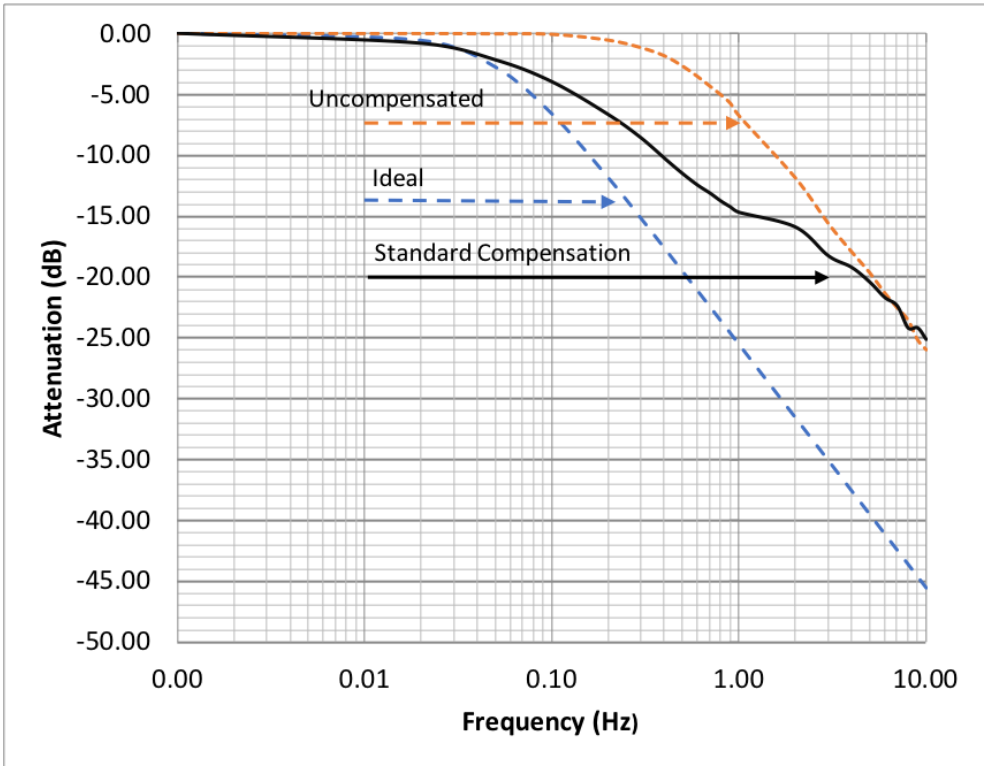

(b) Standard Compensation with $J_{wt} = 13\,kgm^2$

Figure 5.2: Ideal, Uncompensated and Standard Compensation Frequency Responses.

Each Bode plot in Figure 5.2 comprises three traces. The amber dashed lines show the actual uncompensated behaviour. The blue dashed lines show the calculated ideal behaviour for that configuration. The black lines show actual WTE behaviour. For the lower value J_{wt} case, the system closely follows the ideal behaviour up to about $1.5\,Hz$. It then begins to deviate, and by $6\,Hz$, it follows the uncompensated line. In the higher value case the trace begins to deviate from the breakpoint frequency and again follows the uncompensated trace from about $6\,Hz$.

The WTE step and frequency responses, using this compensation scheme, especially at higher emulated moments of inertia, does not meet the specified performance. Consequently an improved scheme was devised and implemented as discussed in Chapter 4. The step and frequency response tests for the improved scheme are presented in the following subsection.

5.2.2 Improved Inertia Compensation Scheme

The tests were repeated using the improved compensation scheme, and the data obtained was processed in exactly the same way. The step response plots for the improved method are shown in Figure 5.3. For the lower value J_{wt} case, the change in step response is barely discernable from the graph. For the high value J_{wt} case, the improved response due to the modified compensation scheme is clear. Table 5.2 compares the time constants for the old and new compensation schemes for both cases. For the $J'_T = 2.02\,kgm^2$ case, the difference in time constant from the ideal value has been reduced from +4.9% to +0.7%. For the $J'_T = 13\,kgm^2$ case, the difference in time constant from the ideal value has changed from −72% to +7.3%.

Table 5.2: Comparison of Standard and Modified Compensation Scheme Time Constants

	$J_T\ (\,kgm^2)$	$\tau_{calc}(ms)$	$\tau_{SC}(ms)$	$\tau_{MC}(ms)$	$\tau_{MCerror}\ (\%)$
$J_{wt} = 2.02\,kgm^2$	0.048	720	755	725	0.7
$J_{wt} = 13\,kgm^2$	0.208	3116	880	3345	7.3

Each Bode plot in Figure 5.4 comprises four traces. The amber dashed lines show actual uncompensated behaviour. The blue dashed lines show the calculated ideal behaviour for that configuration. The black lines show WTE behaviour for the 'standard' inertia compensation scheme. The red lines show WTE behaviour for the 'improved' inertia compensation scheme. For the lower value J_{wt} case, the breakpoint frequency is about $0.2\,Hz$, and the improved system closely follows ideal behaviour up to $10\,Hz$ as required by the original specification. In the higher value case, the breakpoint frequency is about $0.05\,Hz$, and the trace begins to deviate slightly from about $2.5\,Hz$.

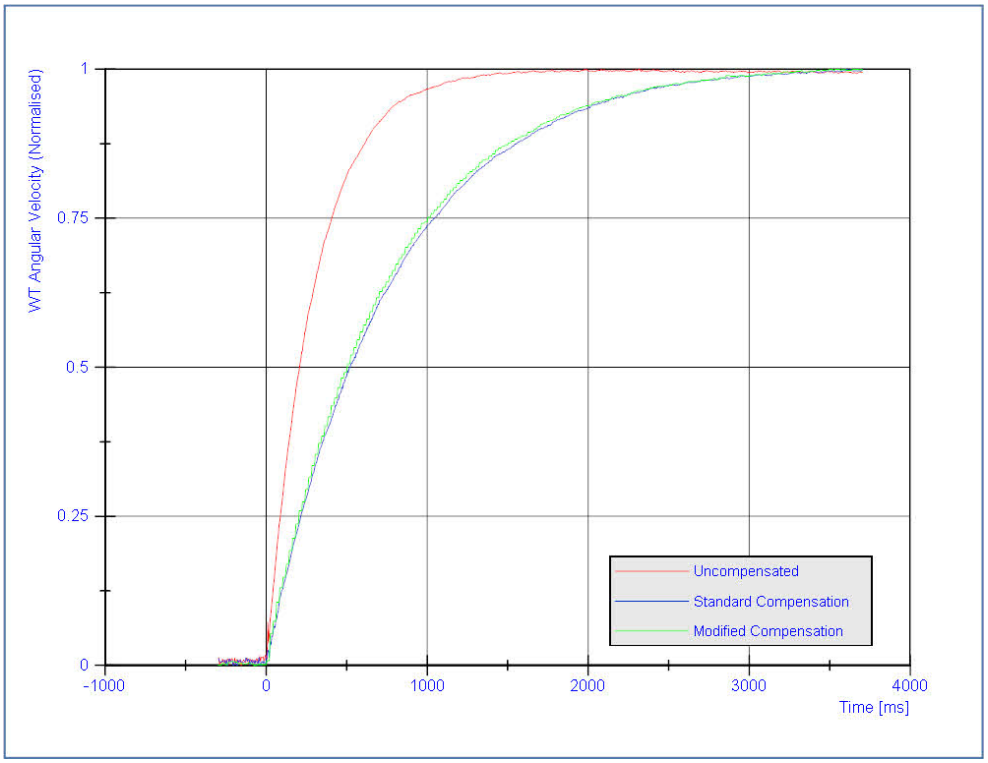

(a) $J_{wt} = 2.02\,kgm^2$

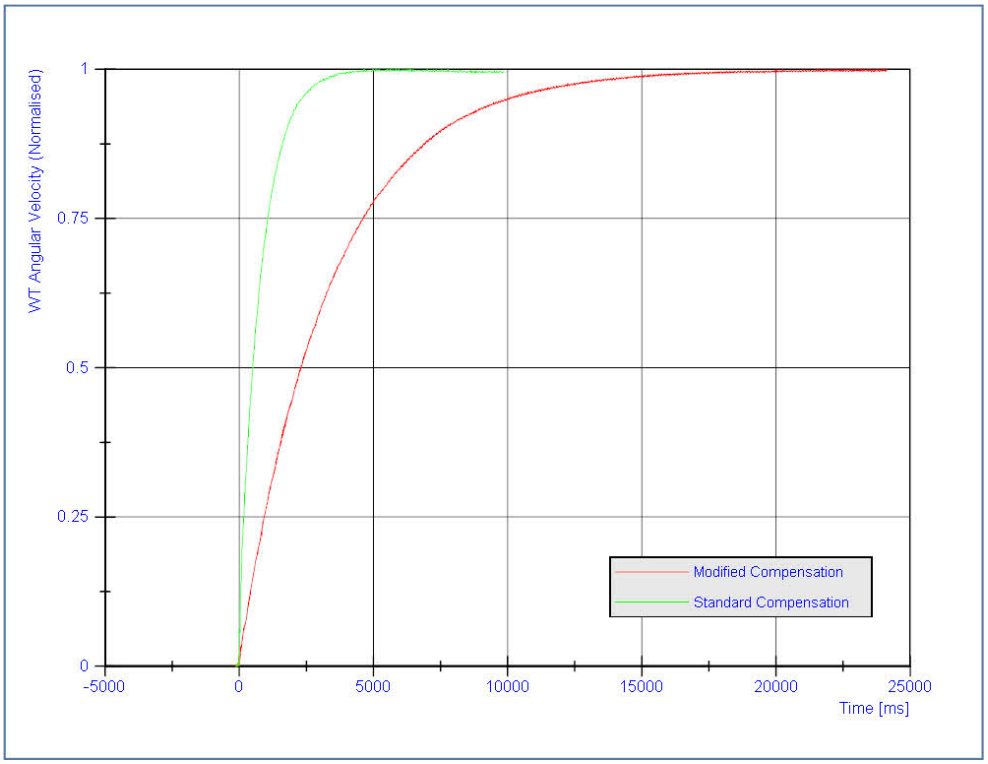

(b) $J_{wt} = 13\,kgm^2$

Figure 5.3: Improved WTE Step Response Comparisons

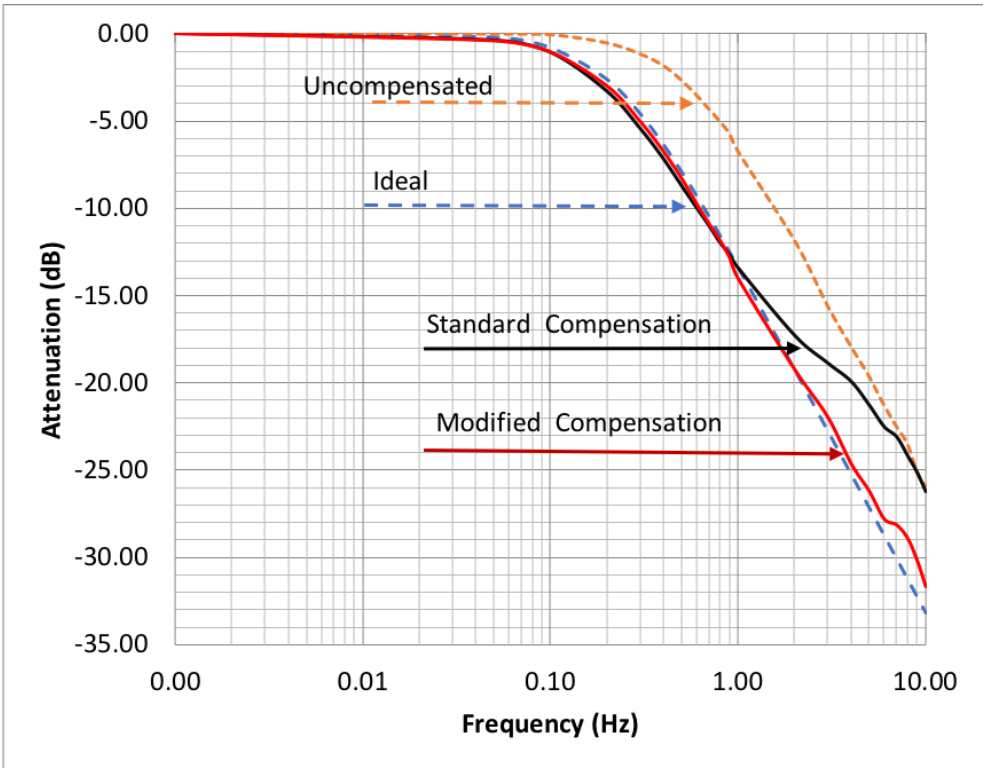

(a) $J_{wt} = 2.02\,kgm^2$

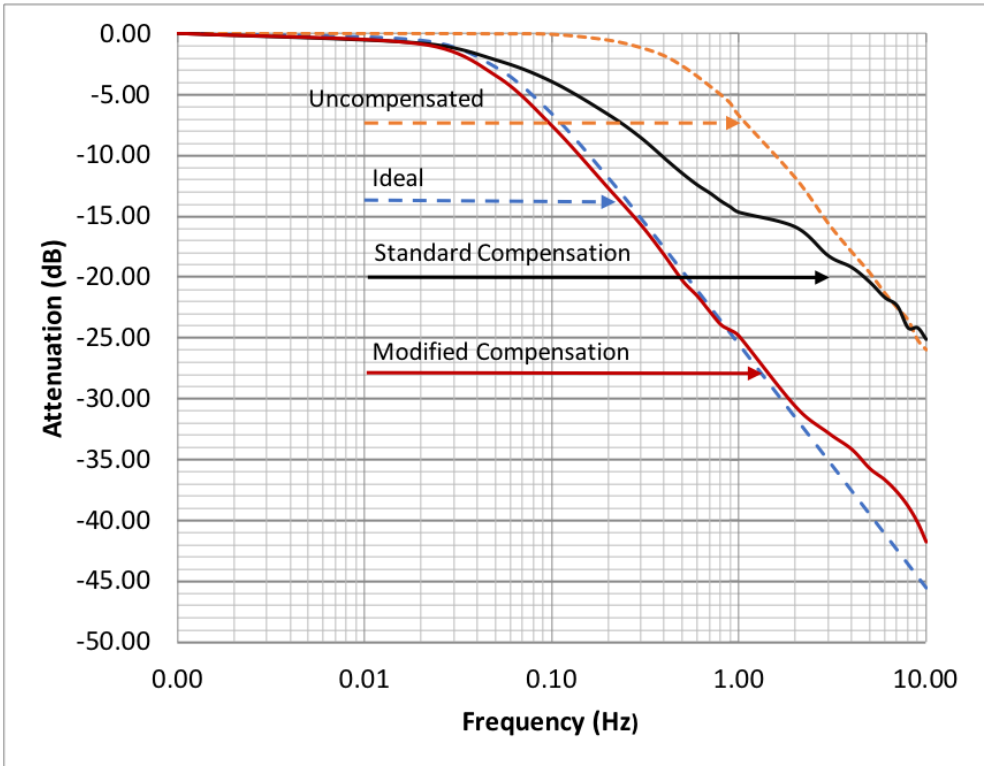

(b) $J_{wt} = 13\,kgm^2$

Figure 5.4: Improved WTE Frequency Response Comparisons

5.2.3 Discussion

The higher total WT system emulated moment of inertia value ($J'_T = 0.208\,kgm^2$) is more than ten times the servomotor system value ($J_S = 0.02\,kgm^2$). This represents a high upper limit to the compensation range and it is assumed that if adequate compensation is achieved at this upper limit then lower values will also be correctly compensated. In each case, Figure 5.4 shows that the original scheme provides no compensation above $6\,Hz$. The improved scheme, however, generates a response that deviates by only $2\,dB$ from the required $-33\,dB$ value at $10\,Hz$ for the $J_{wt} = 2.02\,kgm^2$ case. For the $J_{wt} = 13\,kgm^2$ case, the corresponding deviation from the ideal of $-46\,dB$ is $4\,dB$. The original $10\,Hz$ specification was determined by the blade frequency for a VAWT with $J_{wt} = 2.02\,kgm^2$. For a similar VAWT, with $J_{wt} = 13\,kgm^2$, dimensional scaling gives an increase in linear dimensions of 1.45 with an attendant reduction in angular velocity for a given TSR. On this basis the required correct frequency response need only extend to $6.9\,Hz$. At this point it can be seen that the modified scheme response deviates by only $4\,dB$ from the ideal value of $-42\,dB$. These results show that the modified inertia compensation scheme has improved the frequency response of the system enabling it to reproduce the complex output of a VAWT based on a CFD model as required.

5.3 Mean Torque and Power Response.

A WT system under constant load, subject to unchanging wind velocity, will operate in a quasi-steady state. Dynamic input torque fluctuations, associated with blade aerodynamics, are attenuated, but the underlying mean or 'dc' component is unaffected by rotor inertia. The original CFD analyses, used to derive the WTE control model, make predictions about WT mean torque and power coefficient values across the range of TSRs. The WTE system should reproduce predicted mean torque and power values accurately. To ensure that this was the case, tests were carried out to ascertain mean torque and power outputs over a range of wind velocities, and TSRs, at two different moments of inertia. This set of tests were repeated using four different WT CFD profiles:

- Healthy rotor.
- Rotor with one missing blade.
- Rotor with two missing blades.
- Rotor with three missing blades.

Test results for the healthy rotor profile are detailed below. The remaining results, which show a similarly accurate performance, can be found in Appendix E.

5.3.1 Response with $J_{wt} = 2.02\,kgm^2$

The results from the healthy rotor WTE system tests are summarised in Table 5.3 and displayed in Figure 5.5. In Figure 5.5a, the black dashed line shows the torque plot predicted by a CFD model, with the corresponding WTE system torque output plot shown in green. In Figure 5.5b, the black dashed line shows the power plot predicted by the CFD model and the corresponding WTE system power output plot is shown in red. The predicted

mean torque and power values were obtained from [70] which relates to the VAWT used as the basis for WTE design in this thesis. Predicted performance covered TSRs in the range $(0.1 - 0.9)$ and shows that the optimum TSR is close to 0.5. As WTs are operated at, or close to, optimum TSR the WTE test range was set at $(0.4 - 0.6)$. The predicted values, set out in the paper, are based on a wind speed of $4\,ms^{-1}$. To obtain predicted values for torque and power at other wind velocities, the given figures were scaled by the wind velocity squared ratio and the cubed ratio respectively. The corresponding WTE performance figures were obtained as follows:

Firstly, WT configuration data, including physical parameters and a healthy rotor CFD profile, was entered via the WTE user interface. Then a series of data capture routines was repeated for each TSR and wind velocity permutation:

- The wind velocity parameter was adjusted using a potentiometer while monitoring a LabVIEW virtual instrument.
- The TSR was adjusted by altering the programmable load resistance setpoint while monitoring a LabVIEW virtual instrument.
- The Host Interface was used to capture near-real-time WTE process and instrumentation data for an appropriate interval.

The following WT physical configuration data was used for these tests:
Aperture ($A = 2m^2$); Rotor Radius ($R = 0.7\,m$); Air Density ($\rho = 1.225\,kgm^{-3}$); Gearbox Ratio ($n = 8.3$); and Wind Turbine Moment of Inertia ($J_{wt} = 2.02\,kgm^2$).

Captured data was processed using DIAdem tools to calculate WTE torque and power figures for each situation. The WTE results displayed in Table 5.3 and Figure 5.5 show a very close correlation with the predicted WT performance data.

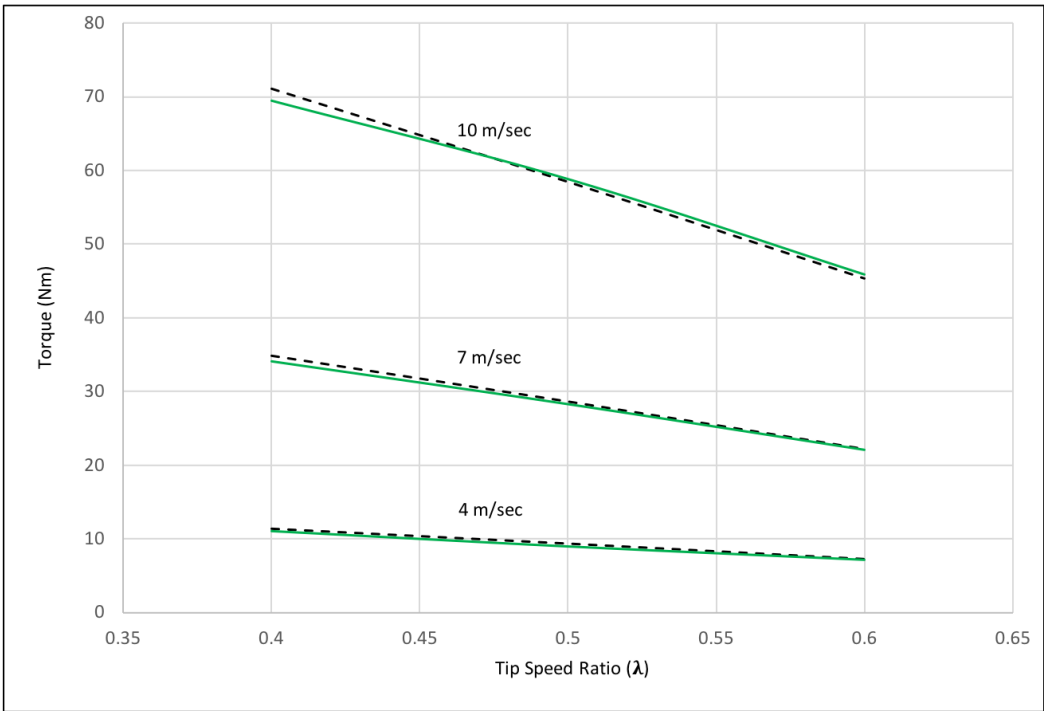

(a) Predicted Torque (Dashed Black Lines) v Actual Torque (Green lines)

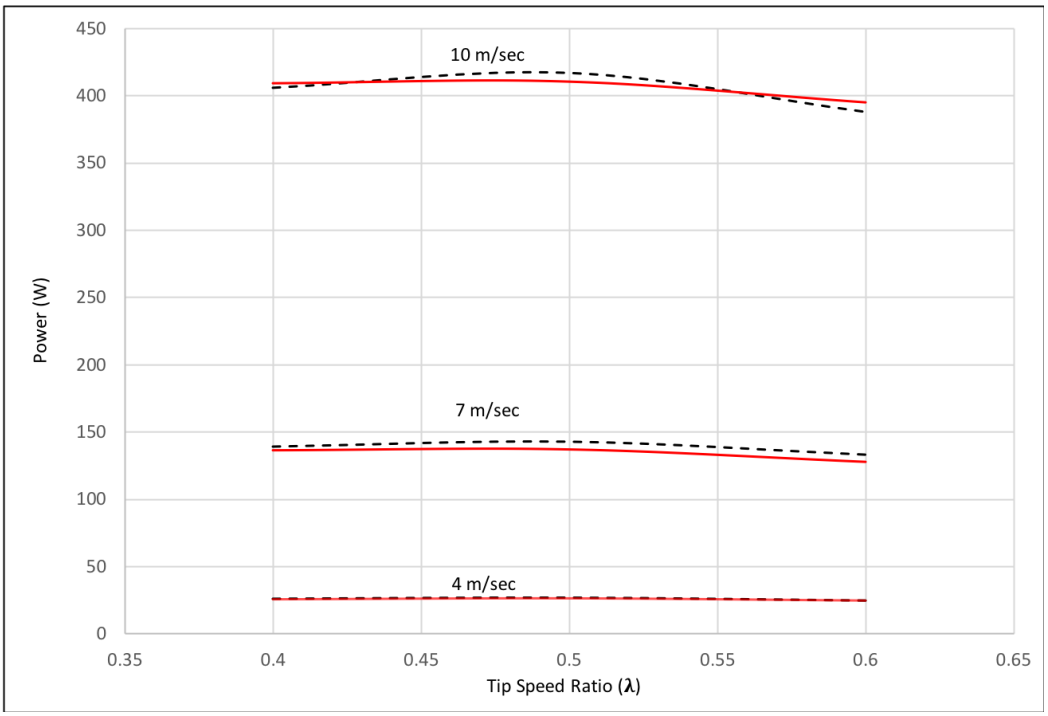

(b) Predicted Power (Dashed Black Lines) v Actual Power (Red lines)

Figure 5.5: Comparison of Predicted and Actual WTE System Behaviour at Differing Emulated Wind Velocities with $J_{wt} = 2.02\,kgm^2$

Table 5.3: Comparison of Predicted and Actual Behaviour at Differing Wind Velocities with $J_{wt} = 2.02\,kgm^2$

TSR	Wind Velocity (ms^{-1})	Predicted Torque (Nm)	WTE Torque (Nm)	Torque Error (%)	Predicted Power (W)	WTE Power (W)	Power Error (%)
0.4	4	11.4	11.1	−2.6	26.0	25.6	−1.5
	7	34.8	34.1	−2.0	139.3	136.5	−2.0
	10	71.1	69.4	−2.4	406.2	409.3	+0.8
0.5	4	9.3	9.0	−3.2	26.7	26.3	−1.5
	7	28.6	28.3	−1.0	143.1	137.1	−4.2
	10	58.4	58.8	+0.7	417.3	410.5	−1.6
0.6	4	7.2	7.1	−1.1	24.8	24.8	+0.0
	7	22.2	22.0	−0.9	133.2	128.2	−3.8
	10	45.3	45.9	+1.3	388.3	395.0	+1.7

5.3.2 Response with $J_{wt} = 10\,kgm^2$

To repeat the tests, for a similar WT configuration with a different moment of inertia, it was necessary to carry out dimensional scaling to obtain realistic results. For similar physical configurations, rotor moment of inertia is proportional to the product of mass and the square of the radius and the radius is proportional to linear dimensions. Assumimg that mass is proportional to volume then mass is proportional to linear dimensions cubed. The moment of inertia is therefore proportional to the fifth power of the linear dimensions. On the basis of this simple model, the physical WT parameters used for the tests with $J_{wt} = 10\,kgm^2$ were set at:

Aperture ($A = 3.79\,m^2$); Rotor Radius ($R = 0.966\,m$); Air Density ($\rho = 1.225\,kgm^{-3}$); Gearbox Ratio ($n = 11.4$); and Wind Turbine Moment of Inertia ($J_{wt} = 10.0\,kgm^2$).

Table 5.4 and Figure 5.6 show the results of the tests. No values for $V_w = 10\,ms^{-1}$ were obtained due to concerns about the programmable load power limitations. The predicted performance values were obtained by using (2.10) and (2.8) together with the previously

Table 5.4: Comparison of Predicted and Actual Behaviour at Differing Wind Velocities with $J_{wt} = 10.0\,kgm^2$

TSR	Wind Velocity (ms^{-1})	Predicted Torque (Nm)	WTE Torque (Nm)	Torque Error (%)	Predicted Power (W)	WTE Power (W)	Power Error (%)
	4	29.7	28.9	−2.7	49.3	47.9	−2.8
0.4	7	91.1	86.1	−5.5	264.0	262.1	−0.7
	4	24.4	23.8	−2.5	50.6	48.1	−4.9
0.5	7	74.8	74.3	−0.7	271.2	259.6	−4.3
	4	19.0	18.0	−5.3	47.1	44.2	−6.2
0.6	7	58.0	55.7	−4.0	252.4	236.6	−6.3

used perfomance data provided in [70].

5.3.3 Discussion

Mean rotor torque is given by (2.10) reproduced here for convenience:

$$T_{rotor} = \frac{1}{2}\rho A\, R\, V_w^2\, C_t(\lambda) \tag{5.2}$$

The torque coefficient function $C_t(\lambda, \theta)$, used by the WTE programme, is loaded as a CFD profile and is a function of the two variables, TSR (λ) and emulated rotor angular position (θ). If position is accurately monitored, the mean torque output should depend only on TSR, which in turn, is dependant on emulated rotor angular velocity (ω) and wind velocity (V_w).

Position data is provided by the servomotor mounted $4096\,ppr$ encoder [73] via the NI DAQ device. The WTE program derives torque coefficient values at sample instants by interpolation. Errors due to position measurement are therefore considered negligible.

Angular velocity data is derived from the drive. As previously discussed in Chapter 4

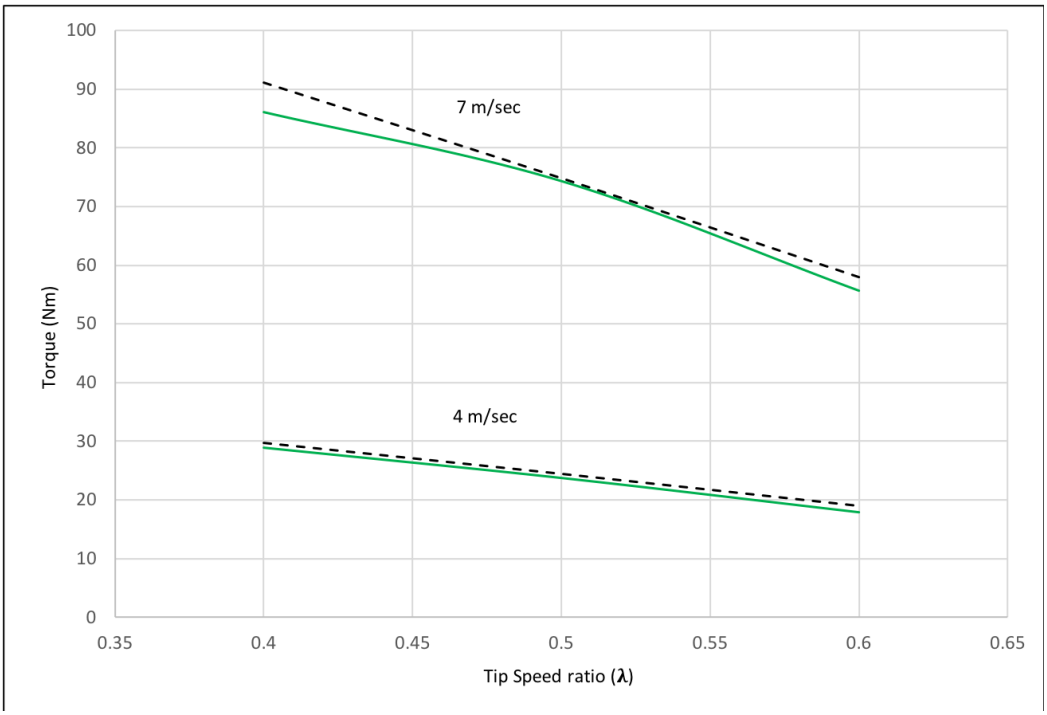

(a) Predicted Torque (Dashed Black Lines) v WTE Torque (Green lines)

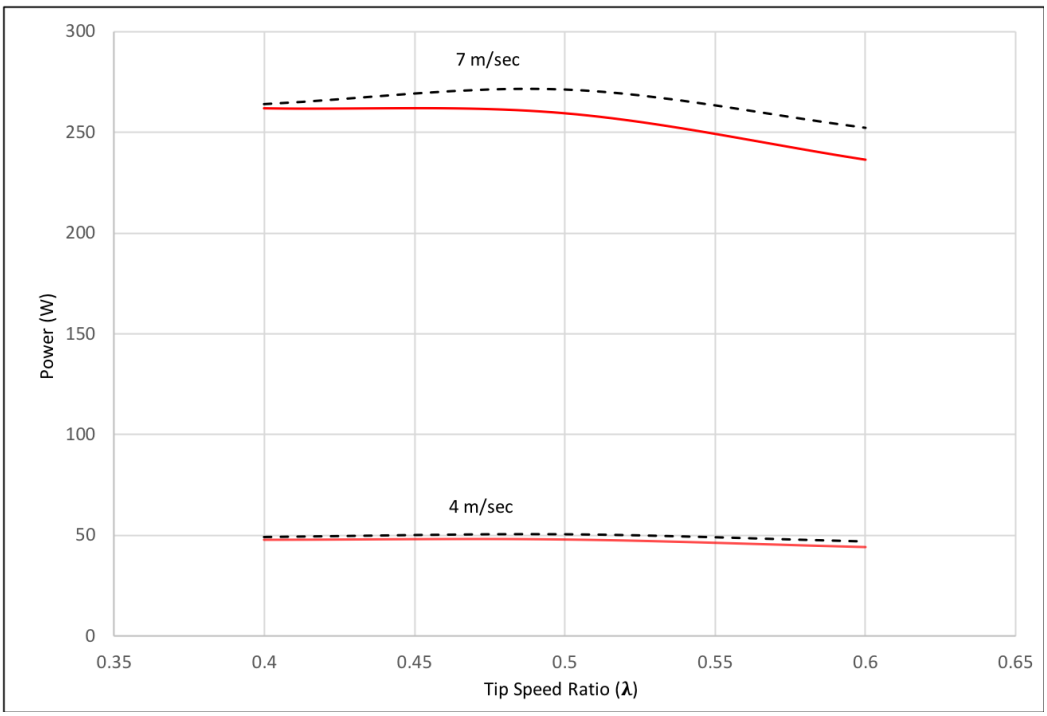

(b) Predicted Power (Dashed Black Lines) v WTE Power (Red lines)

Figure 5.6: Comparison of Predicted and Actual Behaviour at Different Wind Velocities with $J_{wt} = 10\,kgm^2$

Section 4.1, the speed accuracy is $\pm 2\,rpm$ which approximates to $\pm 2\,\%$.

The wind velocity signal (V_w) was provided by a DAQ analogue input channel with a stated accuracy of 0.03% of full scale [74], so errors in this parameter are also considered negligible for the purposes of TSR calculation.

Errors relating to WTE computation of TSR are $\pm 2\,\%$, setting the required TSR values also relies on user input, based on readings on a virtual instrument display. Analysis of the dataset showed that the user induced RMS error range, was $\pm 2\%$.

Wind velocity V_w also relies similarly on user input, and analysis of the dataset showed the RMS error range to be $\pm 2\%$. Since rotor torque is a function of wind velocity squared, the overall error contribution will be $\pm 4\%$.

WTE torque setpoint is provided via a DAQ analogue output channel with a stated accuracy of 0.03% of full scale [74]. The setpoint signal is passed to the drive via an analogue input with stated accuracy of 0.1% of full scale [75]. Both of these figures are considered negligible. Torque output estimation is carried out by the drive, which has a stated accuracy of at least $\pm 2\%$ of full scale [75]. This equates to approximately $\pm 6\%$ of reading for the range of torque values used in the tests.

The mean torque RMS error band, due to the above three significant possible error contributions, is therefore estimated to be $\pm 7.5\%$ of reading.

Mean rotor power is given by (2.8) reproduced here:

$$P_{rotor} = \frac{1}{2}\rho A V_w^3 C_p(\lambda) \tag{5.3}$$

It can be seen that the same error contributing parameters are involved in the derivation of mean power output. The main difference is that rotor power output is a function of wind velocity cubed, so the possible error contribution from this source becomes ±6% of reading. Since errors associated with rotor angular velocity are considered negligible, the accuracy of the power output measurement depends only on the accuracy of the estimated torque output.

The mean power RMS error band, due to the contributions of TSR, wind velocity and power output measurement, is therefore estimated to be ±8.7% of reading.

The results set out in Tables 5.3 and 5.4, show that in every case, WTE performance falls well within the experimental error bounds around predicted WT performance. The results for faulty blade configurations, set out in Appendix E, show the same degree of accuracy.

5.4 Generator Current Analyses for CBM

The datasets obtained during the tests discussed in Section 5.3, relating to healthy and faulty rotor configurations, comprise all the WTE system process and instrumentation measurand data, including generator electrical parameters. In this section, generator current signal data from these datasets, are analysed to assess their suitability for condition monitoring purposes. Graphs are presented relating to the range of TSRs, wind velocities, and emulated WT moments of inertia previously outlined. For each permutation of these parameters the following graph types are presented:

- Time domain.
- Autocorrelation.
- Frequency domain.

In each instance graphs relating to; a healthy rotor, one blade missing, two blades missing, and three blades missing are grouped for comparison.

Datasets relate to test runs carried out over ten-second periods and the time-domain graphs show actual generator output current waveforms over this period. Corresponding autocorrelation graph x-axes extend over a five-second period and the y-axes are scaled in per-unit amps squared, with the base value being the highest value present (normalised). The y-axes for the time-domain and autocorrelation graphs are subtended so that waveform detail can be seen. The ranges are also constant so that relative level changes are obvious. Frequency-domain graphs were created firstly by removing the dc component, then by carrying out a power-spectrum FFT to give x-axes scaled in mean-square amperes. Frequency component amplitudes vary widely between the healthy rotor, and three-blade fault situations. To ensure that relevant frequency components are visible in each plot, the x-axes are scaled

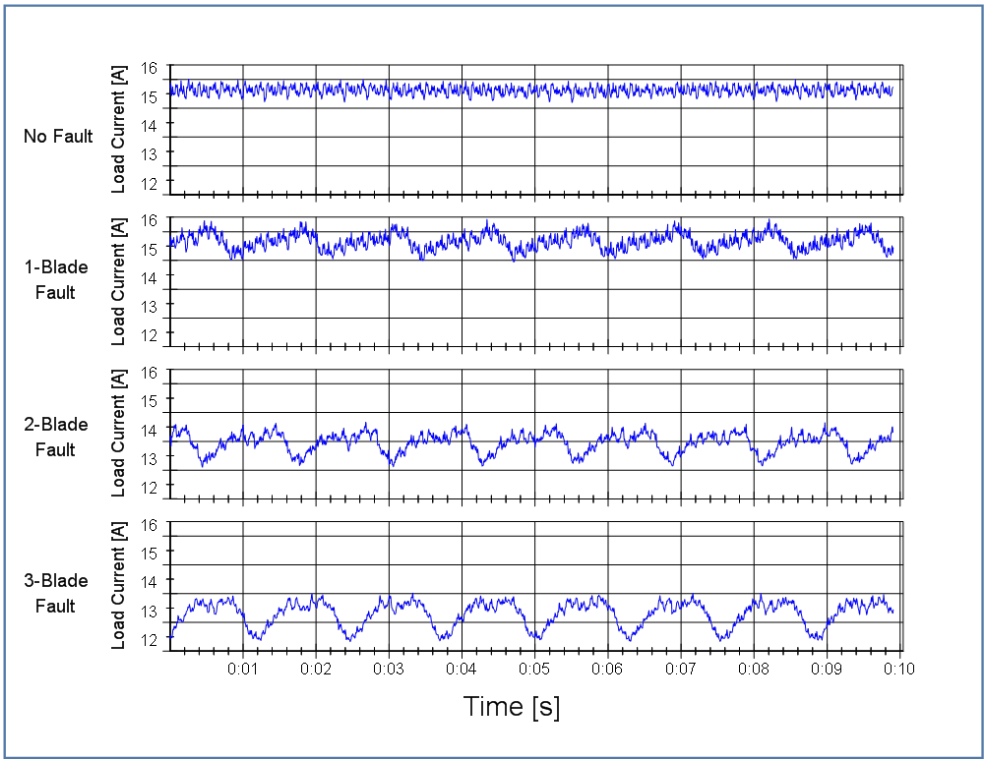

(a) Healthy and Faulted Time Domain Graphs

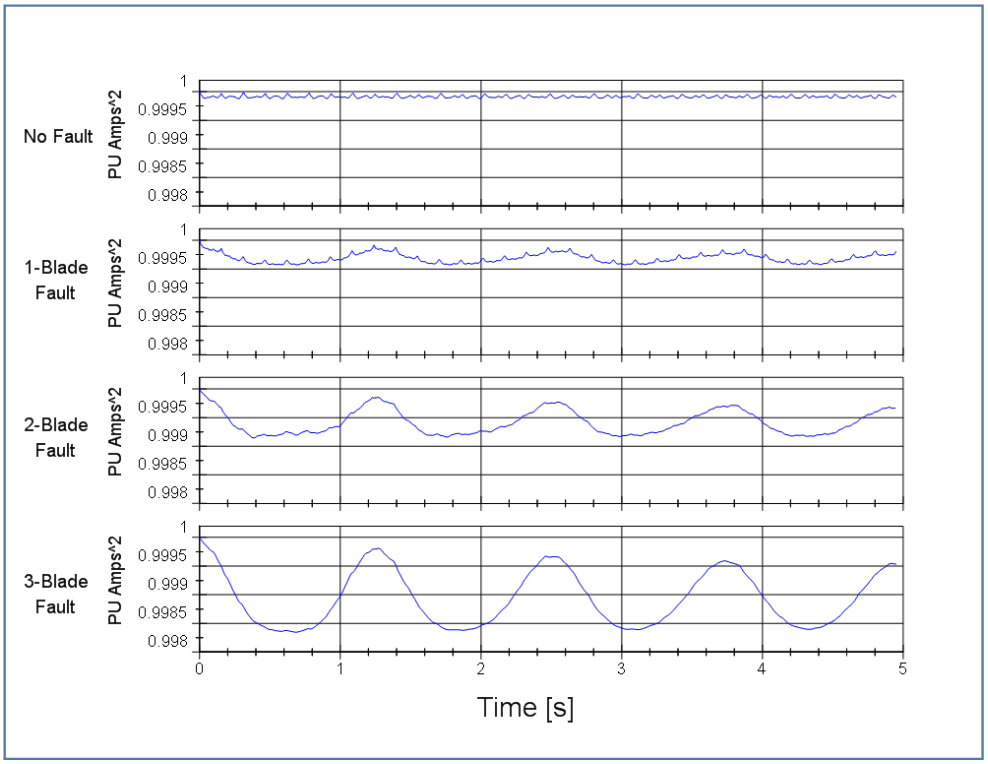

(b) Normalised Healthy and Faulted Auto Correlation Graphs

Figure 5.7: WTE Behaviour with $J_{wt} = 2.02\,kgm^2$, $V_w = 7\,ms^{-1}$ and TSR = 0.5

differently. The sampling rate was $200\,Hz$ giving a maximum frequency range of $100\,Hz$, however the range was curtailed to $20\,Hz$ for clarity. A Hamming window function was chosen to deal with time capture discontinuity. A selection of related graphs are presented in this section in order to draw relevant conclusions.

Figures 5.7 and 5.8a show comparative plots for an emulated WT experiencing a wind velocity of $7\,ms^{-1}$ and a TSR of 0.5. The current waveforms seen in Figure 5.7a show superimposed noise, however, undulations due to the presence of blade faults, where present, are clearly visible. The amplitude of these undulations are seen to increase, while the mean current value decreases, with fault severity. The autocorrelation plots in Figure 5.7b also show the effect of blade faults clearly. In addition, the autocorrelation function tends to remove the effects of random noise. This can be seen in the no-fault and 1-blade fault plots in which small superimposed, periodic waveforms are revealed.

Figure 5.8a shows the corresponding frequency spectrum plot. Components related to blade faults are clearly visible and their magnitude increases significantly with fault severity. The fundamental frequency related to rotor faults is labelled (1) on the plots and the associated second harmonic is labelled (2). The magnitude of these components are seen to increase significantly with fault severity. A number of other frequency components are also clearly visible in the healthy rotor plot. These have been identified by reference to the fundamental, or per revolution, frequency. The component labelled (12) is expected due to the 12-bladed rotor construction, and this is accompanied by a second harmonic labelled (24). The component labelled (8.3) is the fundamental multiplied by the emulated gearbox ratio. This is related to servo motor shaft speed and may be due to coupling misalignment or a bearing problem. The associated second harmonic is labelled (16.6). This artefact is not obvious from the time domain plots and was not expected as the shaft couplings had

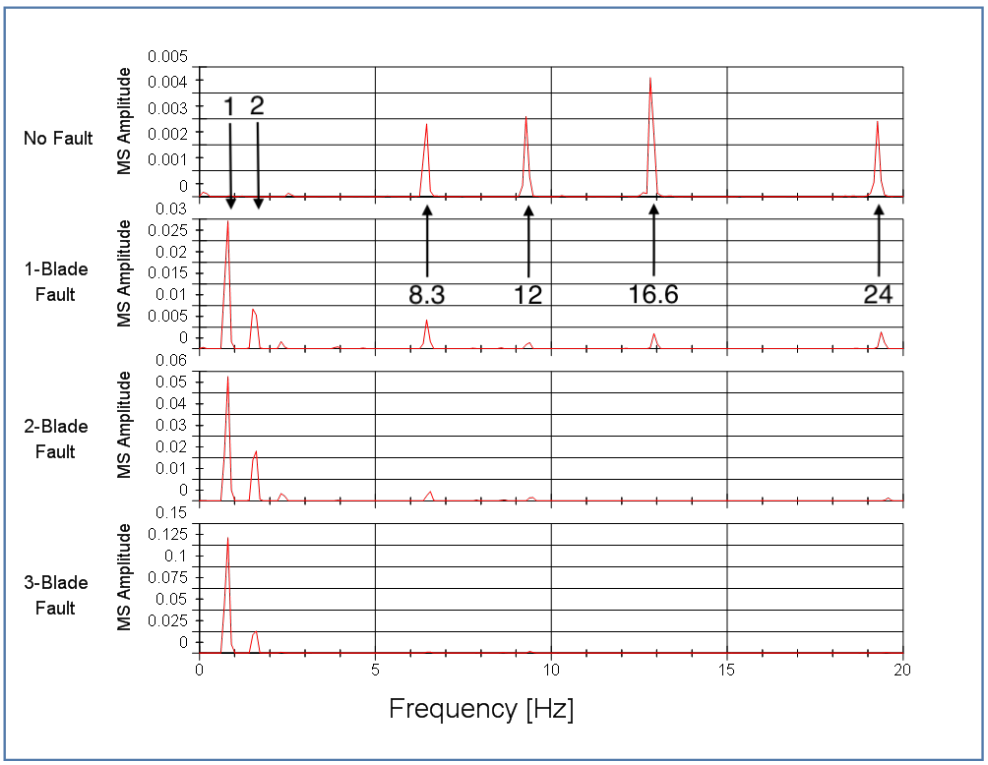

(a) TSR = 0.5

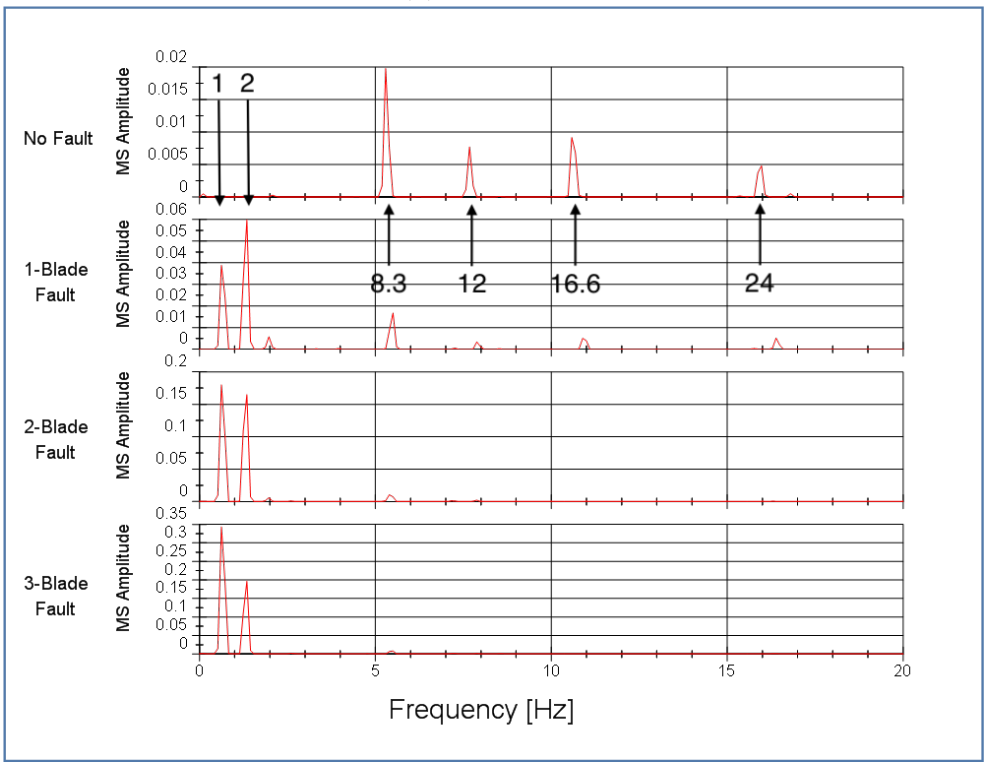

(b) TSR = 0.4

Figure 5.8: Healthy and Faulted Frequency Domain Plots ($J_{wt} = 2.02\,kgm^2$, $V_w = 7\,ms^{-1}$)

been set up using laser alignment tools.

At a given wind velocity, TSR is reduced by increasing load stiffness and this leads to higher system bandwidth. Figure 5.8 also shows the amplitude of spectral components at two different emulated TSRs, with all other parameters fixed. Figure 5.8b shows that by reducing TSR, from 0.5 to 0.4, the amplitude of fault related frequency components are increased at the WTE output as expected. The accompanying frequency shift, due to reduced rotor speed, is also clearly apparent. Table 5.5 provides results showing that, at a fixed wind velocity, blade-fault frequency component amplitude decreases with TSR, and increases with fault severity. Table 5.6 is provided to show the effect of wind velocity variation when TSR is held constant. The blade-fault frequency component amplitude is seen to increase with both wind velocity and fault severity.

Table 5.5: Fundamental Fault Frequency Component Amplitude Variation with TSR and Fault Severity ($J_{wt} = 2.02\,kgm^2$, $V_w = 7\,ms^{-1}$)

TSR	0.4	0.5	0.6
No Blade Fault	0.000	0.000	0.000
1-Blade Fault	0.039	0.030	0.010
2-Blade Fault	0.180	0.058	0.024
3-Blade Fault	0.340	0.134	0.057

Table 5.6: Fundamental Fault Frequency Component Amplitude Variation with Wind Velocity and Fault Severity ($J_{wt} = 2.02\,kgm^2$, TSR = 0.5)

Wind Velocity	$4\,ms^{-1}$	$7\,ms^{-1}$	$10\,ms^{-1}$
No Blade Fault	0.0000	0.000	0.000
1-Blade Fault	0.0004	0.030	0.178
2-Blade Fault	0.0008	0.058	0.341
3-Blade Fault	0.0012	0.134	0.653

The corresponding graphs for an emulated WT with $J_{wt} = 10\,kgm^2$ are shown in Figures 5.9 and 5.10. The waveforms all follow a similar pattern to the $J_{wt} = 2.02\,kgm^2$ cases. The main differences are that all amplitudes are higher and that the frequency components associated with the servomotor shaft are now visible at multiples of 11.4 times the fundamental (per revolution) frequency. This accords with the emulated gearbox ratio in use. Component frequencies are also reduced, by a constant factor, because the larger emulated WT has a reduced angular velocity for a given TSR. Table 5.7 shows that, at a fixed wind velocity, blade-fault frequency component amplitude decreases with TSR, and increases with fault severity. Table 5.8 shows the effect of wind velocity variation when TSR is held constant. The blade-fault frequency component amplitude is seen to increase with both wind velocity and fault severity.

Table 5.7: Fundamental Fault Frequency Component Amplitude Variation with TSR and Fault Severity ($J_{wt} = 10\,kgm^2$, $V_w = 7\,ms^{-1}$)

TSR	0.4	0.5	0.6
No Blade Fault	0.000	0.000	0.000
1-Blade Fault	0.39	0.20	0.074
2-Blade Fault	1.49	0.61	0.179
3-Blade Fault	2.58	1.05	0.463

Table 5.8: Fundamental Fault Frequency Component Amplitude Variation with Wind Velocity and Fault Severity ($J_{wt} = 10\,kgm^2$, TSR = 0.5)

Wind Velocity	$4\,ms^{-1}$	$7\,ms^{-1}$
No Blade Fault	0.000	0.00
1-Blade Fault	0.012	0.20
2-Blade Fault	0.033	0.61
3-Blade Fault	0.059	1.05

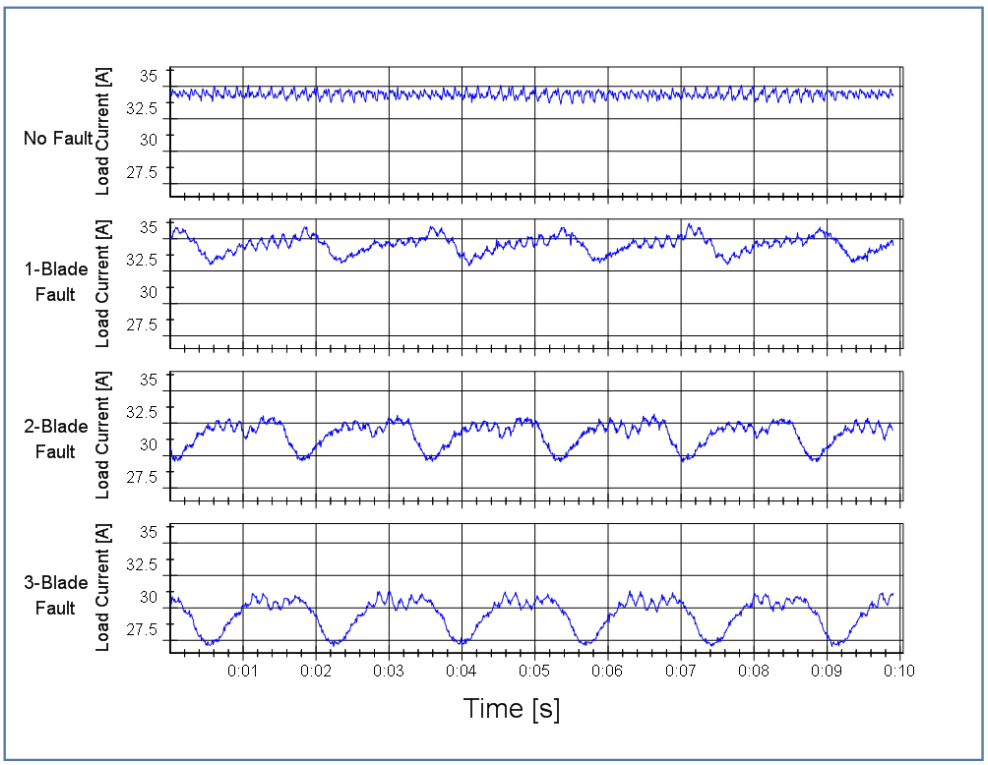

(a) Healthy and Faulted Time Domain Graphs

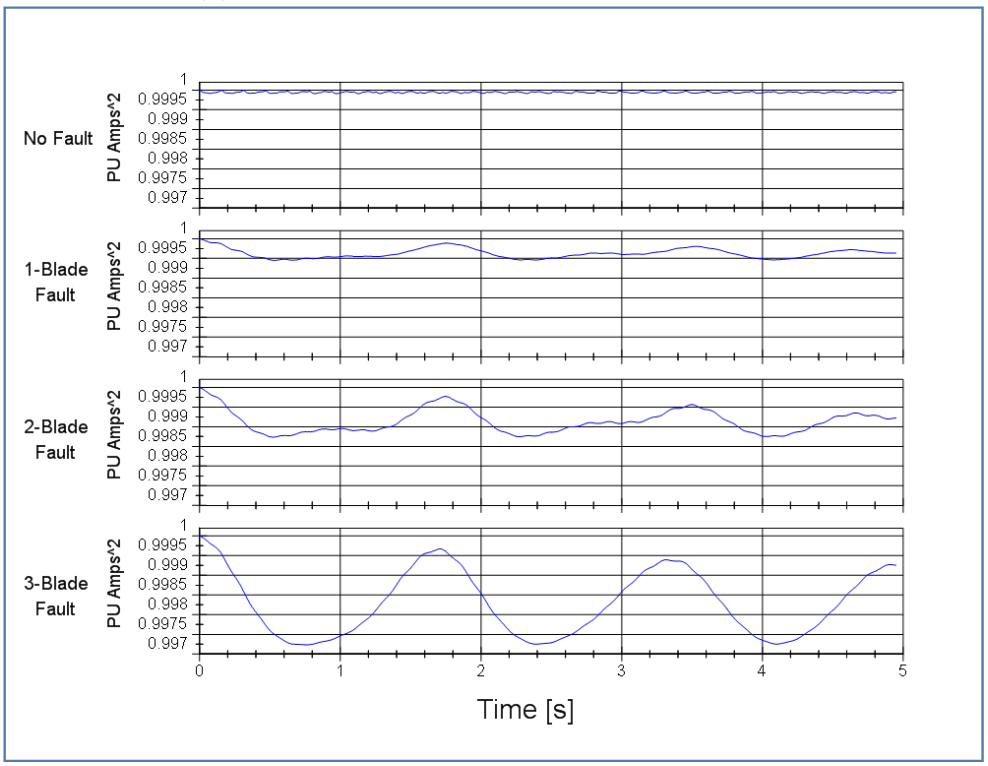

(b) Normalised Healthy and Faulted Auto Correlation Graphs

Figure 5.9: WTE Behaviour with $J_{wt} = 10\,kgm^2$, $V_w = 7\,ms^{-1}$ and TSR = 0.5

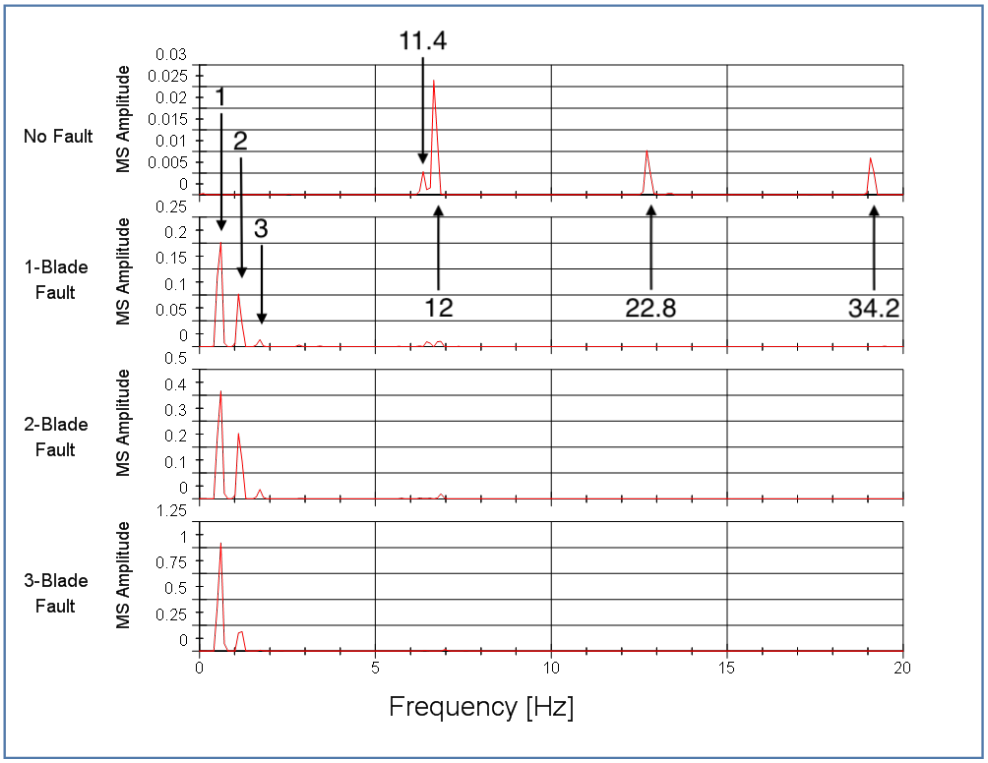

(a) TSR = 0.5

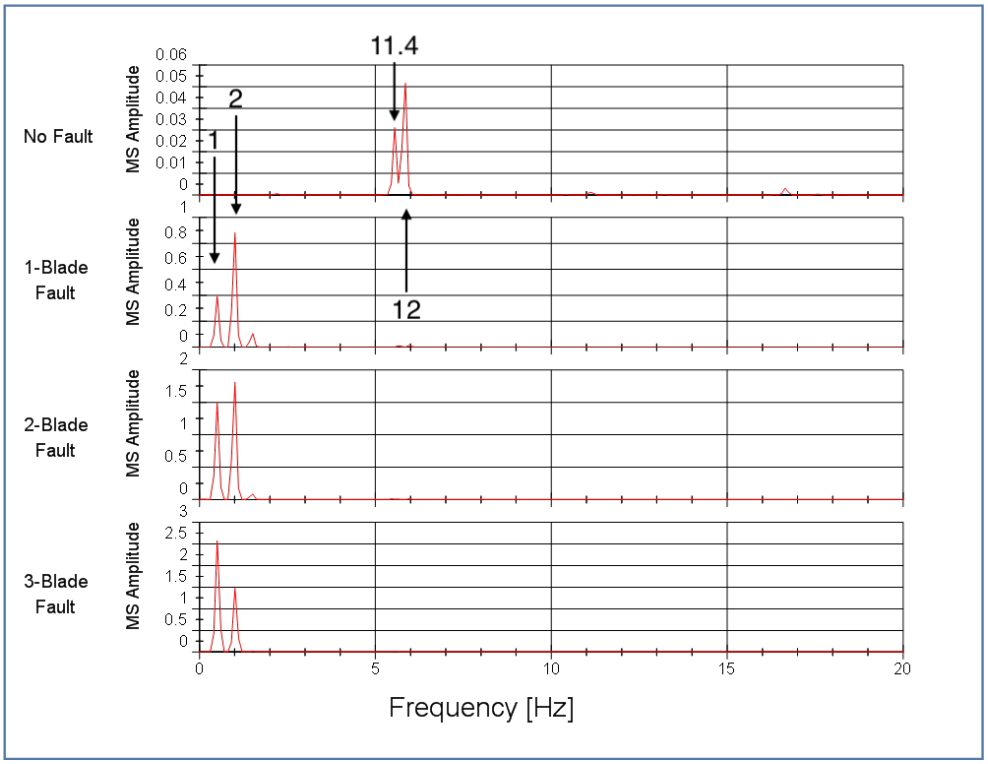

(b) TSR = 0.4

Figure 5.10: Healthy and Faulted Frequency Domain Plots ($J_{wt} = 10\,kgm^2$, $V_w = 7\,ms^{-1}$)

5.5 Summary

The test procedures required to ascertain the ability of the WTE system to meet the research aim stated in Chapter 2 and the design specification presented in Chapter 3 have been fully described in this chapter. The detailed procedures, results, and discussions have been set out. The following three aspects of WTE performance were assessed:

(I) The spectral response.

(II) The ability to generate correct mean torque and power outputs.

(III) The ability of the system to be used as a test bench for developing CBM methods based on the analysis of generator current signals.

The following chapter draws conclusions from the test results and discussions presented in this chapter before summarising the work achieved, the research contributions made and finally making recommendations for further work and research.

Chapter 6

Conclusions and Further Work

6.1 Conclusions

The conclusions follow directly from the experimental test results and discussions set out in Chapter 5. The order in which tests were carried out, and therefore the corresponding order of conclusions, is significant. For the Wind Turbine Emulator (WTE) system to be useful for the investigation of Vertical Axis Wind Turbine (VAWT) fault and Condition Based Maintenance (CBM) issues, the spectral response and reproduction of mean torque and power must be accurate. To meet the more onerous spectral requirements for VAWT emulation it was necessary to create a novel inertia compensation technique. It was appropriate, therefore, that this aspect was tested and verified first. Having achieved the required frequency response, using the new inertia compensation method, the accurate reproduction of average torque and power values across all turbine configurations was verified. Finally, it was possible to test and establish the suitability of the system for incipient fault and CBM investigations.

6.1.1 Frequency Response

To achieve the WTE performance required for CBM development purposes, accurate frequency response is necessary. For the Wind Turbine (WT) used in the design of this system,

an accurate emulated response up to $10\,Hz$ was specified. The final bode plots, shown in Chapter 5, Figure 5.4, show that, by using a novel inertia compensation scheme, this is achieved. For the case where $J_{wt} = 2.02\,kgm^2$, the deviation from the ideal of $-33\,dB$ at fifty times the mechanical system bandwidth ($10\,Hz$), is only $2\,dB$. For the scaled case with $J_{wt} = 13\,kgm^2$, the emulated mechanical system bandwidth is $0.05\,Hz$ and at fifty times this value, the deviation from the ideal of $-33\,dB$ is again only $2\,dB$. The original requirement for accuracy up to $10\,Hz$ is based on the torque ripple frequency associated with the number of turbine blades and the maximum rotor angular velocity. Dimensional analysis, for the higher moment of inertia turbine, leads to a requirement for an accurate response up to $6.9\,Hz$. At this point the deviation from the ideal of $-42\,dB$ is only $4\,dB$ and the magnitude of this deviation from ideal remains constant up to a frequency of $10\,Hz$. It is concluded, therefore, that the frequency response of the WTE is sufficiently accurate to support the development of fault diagnosis and CBM methods as intended.

6.1.2 Mean Torque and Power Response

In addition to accurate frequency response, the WTE must also accurately reproduce the Computational Fluid Dynamics (CFD) predicted mean rotor output torque and power over the emulated device's range of operation. The tables and graphs shown in Chapter 5, Section 5.3 show clearly that this is the case. For the emulated WT with $J_{wt} = 2.02\,kgm^2$, the maximum errors in mean torque and power output, within the operational range, are -3.2% and -4.2% respectively. The corresponding average error values over the range are -1.2% and -1.3%. For the emulated WT with $J_{wt} = 13\,kgm^2$, the maximum errors in mean torque and power output within the operational range are -5.5% and -6.3% respectively. The corresponding average error values over the range are -2.3% and -2.8%. The error bounds associated with the calculation of mean rotor torque and power output are $\pm 7.5\%$ and $\pm 8.7\%$ respectively.

The test results all lie within the expected measurement error bounds, so it is concluded that the WTE accurately reproduces CFD predicted steady state mean torque and power outputs for all the healthy and faulty rotor profiles analysed.

6.1.3 Generator Current Analysis for CBM

The analyses and resulting plots shown in Chapter 5, Section 5.4 demonstrate that, in all instances, emulated blade faults are identifiable from the generator current output signal. While the presence of a fault is clearly evident in the time-domain plots, the frequency-domain plots convey more detailed information. In addition to the components associated with blade faults it was also possible to discern components associated with a servomotor shaft issue. This was not evident from the time-domain plots. The frequencies associated with blade faults are relatively low but are, nevertheless, well above the breakpoint frequency of the emulated WT system. For example, from the analyses in Section 5.2, the breakpoint frequency for the $J_{wt} = 2.02\,kgm^2$ case is known to be $0.2\,Hz$. The associated blade-fault frequency is about $0.9\,Hz$ so this component has been attenuated by about $13\,dB$ and the second harmonic component by $19\,dB$. It can also be seen, from Tables 5.5 and 5.7, that the use of a 'forcing function' to artificially reduce Tip Speed Ratio (TSR) below optimal, thus increasing bandwidth, has the effect of highlighting frequency components, including those associated with faults.

Data captured during tests emulating healthy and faulty rotor profiles show that generator load current signals reflect rotor behaviour as expected. Faulty rotor behaviour was clearly visible in time domain plots, autocorrelation plots, and frequency domain plots. The effects could be seen at all wind speeds, TSRs and WT dimensions used. It is concluded, therefore, that the WTE system is suitable for the development of fault identification methods and CBM techniques as intended.

6.2 Summary of Work Achieved

The research aim, set out in Chapter 2, Subsection 2.5.1 has been achieved in full. A novel WTE technique has been devised to meet an identified need for the accurate emulation of recent complex multi-bladed Vertical Axis Wind Turbine (VAWT) designs. This is necessary because existing methods, used for Horizontal Axis Wind Turbine (HAWT) emulation, are inadequate for the development of fault detection and CBM methods for VAWTs. The reconfigurable WTE system has been implemented using industry standard hardware and software tools as intended. A servomotor and drive combination with a high resolution position encoder are employed because accurate control of output torque related to rotor position and velocity is required. The method uses CFD analyses data, loaded as a 2-D array, to generate instantaneous torque coefficient values based on emulated WT rotor position and TSR. The healthy or faulted operation of a particular emulated VAWT is associated with the array in use. The technique is compatible with simpler turbines, including HAWTs, by use of the appropriate CFD data. Dimensional aspects of the device to be emulated are loaded via the user interface. To achieve the frequency response required to model complex multi-bladed VAWT behaviour, it was necessary to devise and implement a novel inertia-compensation scheme based on real-time observation of system stiffness. A facility to capture near-real-time data, for offline analysis, was also successfully achieved. The duration of capture is reconfigurable with all available measurands and process variables being sampled at $5\,ms$ intervals using the Technical Data Management Streaming (TDMS) format. The completed system has been successfully used to capture, for offline analysis, all process measurands including generator output current data associated with emulated healthy and faulted WT behaviour.

A further achievement, underpinning the successful development and operation of the WTE

system, was the design and implementation of the Programmable Load. The creation of the load was necessary because no device was available commercially, at a viable cost or with sufficient flexibility, that would support the WTE application. The developed device is based on the control of power MOSFETs operated in 'linear mode' to act as a variable resistive load connected to an efficient, axial-flux, permanent-magnet, dc machine. Considerable effort was expended on the specification and design of the load to ensure that its operational flexibility and accuracy met the needs of the WTE system. The specification, design and implementation of the Programmable Load are set out in Appendix B.

6.3 Contribution

No instances of VAWT emulation incorporating accurate methods for modelling output torque based on intrinsic WT characteristics have been found in the literature. CFD is widely used to model VAWT behaviour and fault characteristics, however, accurate WTE is still necessary because CFD does not model dynamic behaviour associated with device moment of inertia and loading. The method developed here uses an existing technique (CFD) in a novel way to address this situation. The testing carried out in this research demonstrates that there is now a WTE method available that is capable of accurately simulating the predicted healthy and faulted behaviour of multi-bladed VAWTs designed for urban use. Testing also confirms that the technique facilitates the analysis of generator output signals on a WTE test bed for the development of fault diagnosis and CBM techniques. This work has extended the application and usefulness of both CFD and WTE techniques and is, therefore, a contribution to knowledge.

To achieve the more onerous frequency response capability required of a VAWT emulator, it was necessary to devise an original technique for inertia compensation. Existing meth-

ods based on an acceleration observer, necessarily include a Low Pass Filter (LPF) in the feedback path. The main purpose of the filter is to ensure stability but it is also required to eliminate noise. The presence of this filter, at settings that eliminate noise, reduces the system bandwidth unacceptably for this application. The improved technique eliminates the filter induced performance degradation by dynamically manipulating z-plane pole positions based on real-time observation of system stiffness and incorporating an adaptive 'lag-lead' pre-filter at the input to the torque compensation control loop. System behaviour is approximated by an s-plane model and pole manipulation is achieved by dynamic modulation of the WT moment of inertia quantity used in the feedback path. This is an original technique and has application wherever torque compensation based on an acceleration observer is used. It is, therefore, a contribution to knowledge. Details of the method and its implementation are set out in Chapter 4.

6.4 Further Work and Recommendations

Throughout this thesis, CFD analyses based on ideal uniform upwind velocity fields have been used. Site wind velocity profiles are, however, affected by the local topography including adjacent objects that induce turbulence. The resulting wind velocity profiles, therefore, vary with wind direction and velocity. CFD analyses, based on site topography, are currently used to assess aspects of WT performance in different target environments. Since these assessments are unable to model dynamic inertial response or provide a physical output, the WTE method developed in this thesis may be used to enhance this type of appraisal. For a complete analysis, of site condition effects, the use of multiple CFD profiles, relating to different wind velocities and directions, is required. The WTE system can accommodate this as CFD profiles may be changed quickly and easily to complete a series of tests based on a range of wind directions and velocities. The requirement to carry

out separate tests with multiple profiles may be eliminated, however, by increasing the WTE system array dimensions from two to four. This improvement in WTE functionality would additionally facilitate direct comparison of WTE system behaviour with that of a WT operating in the field. Such comparisons could be used to assess and improve WTE algorithms and the underpinning CFD analyses.

The ability to model WT behaviour in particular situations could also provide the basis for the derivation of comparative process models for CBM purposes. Increasing or excessive deviation from the expected WT behaviour could be used to identify incipient problems. Such a model would use site specific CFD data in conjunction with a process model. Expected rotor inertial response, within the model, could be predicted by use of an adaptive, first-order filter based on the stiffness observer developed in this thesis. To achieve this in practice, the target WT would have to equipped with rotor position and wind velocity transducers.

The TSR range of the CFD data used in this thesis is restricted to values of between zero and one and is sufficient to model performance at steady wind speeds and for situations where wind speed reductions are not rapid. TSR may, however, transiently take values greater than one, due to the effects of WT inertia, if wind velocity falls rapidly. Under these circumstances the current WTE system uses a TSR of one until the rotor slows sufficiently to bring the TSR back in range. Using CFD profiles that include TSR values greater than one would improve the accuracy of WTE system response for this situation.

The generator current signals, analysed in Chapter 5, were made artificially stationary by using a constant wind velocity and TSR for each test run covering healthy and faulty profiles. This ensured that the resulting plots were easily comparable. In the field, wind

speed varies unpredictably resulting in non-stationary signals. This makes comparisons using frequency analysis, for example, difficult. A solution is to carry out sampling based on rotor position. The WTE system is equipped with an accurate position transducer so implementation of this sampling method on the emulator is easily achieved. To use this technique in the field for CBM purposes, it would be necessary to equip the WT with a position transducer.

It has been assumed that predicted performance at one particular wind velocity can be scaled, using the torque or power coefficient, to predict performance at other wind velocities. This is a technique widely used in the wind energy industry to reduce computational effort and is considered valid within the operational wind speed range of the device to be modelled. To model WT behaviour where this condition is not valid, the method could be extended by using a 3-D array to generate torque coefficient values. To achieve this, a significant increase in the number of CFD analyses is required.

6.4.1 Recommendations

To extend the contribution to research in the area of urban wind and its economic deployment, the following further work should be implemented.

(I) To obtain and use CFD models for multiple specific WT environments in order to predict WT behaviour in the field. Site wind velocity is not uniform across the WT aperture and the wind velocity profile varies with upwind velocity and direction due to turbulence induced by adjacent objects. It is envisaged that the dimensions of the array used to store a CFD profile could be extended to accomodate the required

functionality.

(II) To research methods for using site specific CFD data to derive comparative process models for incipient fault detection and CBM. Rotor inertial response, within a process model, could be predicted by use of an adaptive first-order digital filter based on the system-stiffness observer developed in this thesis. To achieve this in practice the target WT would need to be equipped with rotor position and wind velocity transducers.

(III) To obtain and use CFD models for the situation where a VAWT rotor is decelerating due to a rapid fall in wind velocity. Under these circumstances the TSR will be transiently higher than one for a crossflow VAWT due to rotor momentum. Obtaining CFD profiles covering higher TSRs would facilitate more accurate emulation of WT transient behaviour for this situation.

(IV) Generator current signals used for CBM, are not stationary w.r.t time due to rotor speed variation. The use of positional data to allow sampling by position rather than time should be investigated. This would facilitate the identification of incipient faults in the more realistic situation where wind velocity varies.

Appendix A

WTE Hardware Specifications

Details of the industrially available hardware used to implement the WTE system is provided here together with references to relevant specifications.

Table A.1: Servomotor Parameters [73]

Motor Type	Emerson Unimotor fm: 6-Pole Brushless Servomotor	
Frame Size	115	
Moment of Inertia	0.00128	kgm^2
Motor Voltage	400	V, 3ϕ
Rated Current	4.5	A
Stall Current	5.2	A
Rated Speed	2000	rpm
Rated Torque	10.8	Nm
Stall Torque	12.5	Nm
Peak Torque	18.7	Nm
Rated Power Output	2.26	kW
Torque Constant K_t	2.40	Nm/A
Speed Constant K_e	147	$V/krpm$
Feedback Device	Incremental Encoder 4096 ppr A, B, Z signals	

Table A.2: Drive Parameters [75]

Drive Type	Emerson Unidrive SP1406
Supply Voltage	(380 - 480) V, Three-Phase, (48 - 65) Hz
Maximum Supply Current	13.4 A
Maximum Motor Current	11.0 A
Typical Output Power	5.5 kW
Encoder Input	Incremental Encoder with A, B, Z signals and U, V, W Commutation Signals
Analog Inputs	A.1: $\pm 10\,V$, 16-bit plus sign, $4\,ms/250\,\mu s, 100\,k\Omega$ A.2: $\pm 10\,V$, 10-bit plus sign, $4\,ms/250\,\mu s, 100\,k\Omega$ A.3: $\pm 10\,V$, 10-bit plus sign, $4\,ms/250\,\mu s, 100\,k\Omega$
Analog Outputs	A.1: $\pm 10\,V$ dc/0 or 4-20 mA, 10-bit plus sign, $4\,ms$ A.2: $\pm 10\,V$ dc/0 or 4-20 mA, 10-bit plus sign, $4\,ms$ or $250\,\mu s$ in closed loop 'fast-update' mode
Digital In/Out	D.(1-3): In/Out $24\,V$, $4\,ms/250\,\mu s$ closed loop D.(4-6): In $24\,V$, $4\,ms/250\,\mu s$ closed loop
Serial Communication	RS 485
Output Torque Estimation	Torque Estimate: $\pm 2\%$, 10-bit plus sign, $250\,\mu s$ update.
High Speed Torque Control Frequency Response	$3\,dB$ point: $1100\,Hz$ $-45°$ point: $400\,Hz$
Drive Capabilities	Configurable via keypad, smartcard and communications link to PC or network. Programmable for accurate position, speed, acceleration and torque control in isolation, or with other drives.

Table A.3: Data Acquisition (DAQ) Card Parameters [74]

Data Acquisition Interface	NI PCI-6229
Measurement Types	Quadrature Encoder, Digital, Frequency, Voltage
Analog Inputs	32 Single-Ended/16 Differential Channels: $\pm 10\,V$ dc, 16-bit, $250\,kS/sec$, 4095 Sample Memory
Analog Outputs	4 Channels $\pm 10\,V$ dc, 16-bit, $833\,kS/sec$, $5mA$ Current Drive (Single)
Digital In/Out	48 Bi-Directional Channels: $(0-5)\,V$, TTL, Current Drive $24mA$ (Single), $448mA$ (All) Maximum Clock Rate $1\,MHz$
Counters/Timers	2 Counters, 2 DMA Channels:$(0-5)\,V$ Max f_{source} $80\,MHz$ Pulse Generation: 32-bit, TTL, Timebase Stability $50\,ppm$

Appendix B

Programmable Load Design

In order to use and test the WTE system that has been created for this work, it was necessary to design and implement a programmable load that would allow it to be used and tested reliably and accurately. Such a device was not available commercially at a cost that was feasible. The design of the programmable load to achieve the required functionality is set out here.

B.1 Generator and Programmable Load

The mechanical device chosen to load the WTE is a D135RAG dc motor manufactured by the Lynch Motor Company [76]. It is an axial-flux permanent-magnet device with low armature resistance and therefore high efficiency (typically 91% when operating as a motor). It is capable of operating at high speed ($4000\,rpm$) and high torque ($39\,Nm$). In order to characterise the motor as a generator, tests were carried out using the Unidrive and Unimotor set-up. A fixed resistance electrical load was connected to the generator output terminals to provide an electromagnetic load torque proportional to speed. The speed of the generator was increased incrementally and corresponding values of speed, torque, output voltage and output current were recorded. From these results values for the machine constant (K_m) the armature resistance (R_a) and starting torque were estimated.

The results, together with manufacturer's data, are summarised in Table B.1.

Table B.1: Relevant Generator Parameters

Machine Type	L.M.C. D135RAG dc Axial Flux Permanent Magnet	
Speed Range	$(0-4032)$	rpm
Torque Range	$(0-39.9)$	Nm
Moment of Inertia	0.0187 (From tests)	kgm^2
Starting Torque	0.61 (From tests)	Nm
Armature Resistance (R_a)	16.95 (22.00 From tests)	$m\Omega$
Armature Inductance (L_a)	16	μH
Machine Constant (K_m)	0.196 (0.203 From tests)	NmA^{-1}

Generator electromagnetic torque and EMF are given by:

$$T = K_m I_a \tag{B.1}$$

$$E = K_m \omega \tag{B.2}$$

where:

T = Generator Electromagnetic Torque(Nm), K_m = Machine Constant(NmA^{-1}),

I_a = Generator Armature Current(A) and ω = Shaft Angular Velocity($rads^{-1}$).

From (B.1), assuming that the frictional torque associated with starting the generator remains constant, it is possible to map armature current to load (generator) torque. Similarly, from (B.2), generator EMF may be mapped to shaft velocity. By taking account of the gear ratio (1:8.3) a graph was plotted (Figure B.1) describing the WT's operation at different wind velocities and TSRs. Three TSRs (0.4, 0.5 and 0.6) have been plotted at six different wind velocities. For example, at a wind velocity of $12\,ms^{-1}$, and a TSR of 0.6, the shaft will be rotating at $815\,rpm$ with an applied torque of $7.7\,Nm$. This equates

to a generator EMF of 16.8 V and an armature current of 36 A. The ratio of voltage to current, at any point, specifies the total resistance required to apply this load to the WT. The product of voltage and current specifies the rating of that resistance. The graph thus shows clearly the range of load resistance required and the corresponding power, voltage and current ratings. (It should be noted that the resistance values derived include the armature resistance of the generator (22 $m\Omega$). Table B.2 summarises the requirements.

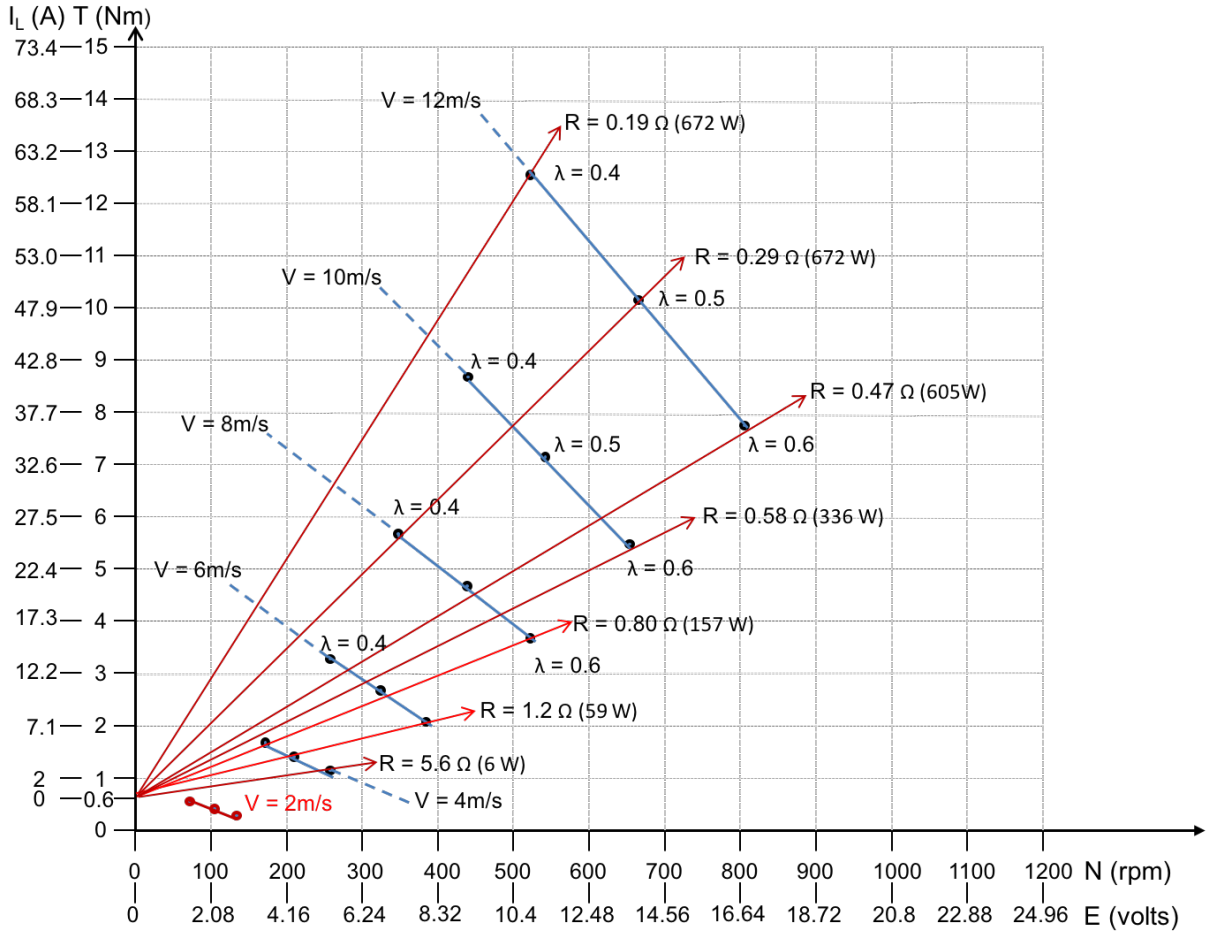

Figure B.1: Graph used to Estimate Programmable Load Resistance Parameters

To facilitate smooth operation of the load it was decided to utilise power MOSFETs operating in 'linear mode'. An inner analogue control loop was used to linearise the MOSFET response and, using a Finite State Machine (FSM) program, an outer digital control system

Table B.2: Programmable Load Requirements

V_{gen} Range	$(0-20)$	V
I_{gen} Range	$(0-70$	A
Power Dissipation Capacity	$(0-700)$	W
Resistance Range	$(0.15-6.0)$	Ω
Frequency Response	200	Hz

was used to implement the following load regimes:

- Constant Current control giving a constant Torque regardless of Speed.
- Constant Resistance control giving a rising linear Torque/Speed characteristic.
- System Standby.

The functional diagram for the programmable load components can be seen in Figure B.2.

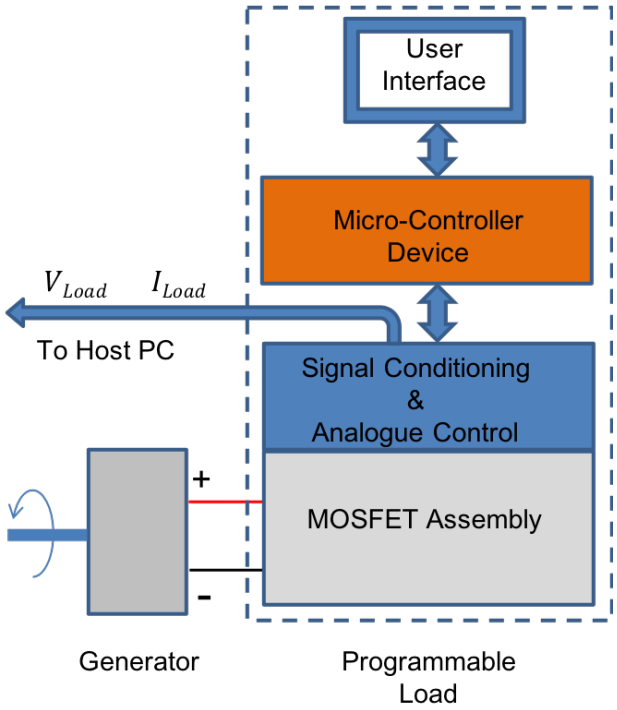

Figure B.2: Programmable Load Functional Diagram

B.1.1 MOSFET Assembly

The data derived from Figure B.1 was used to specify the type and number of Power MOSFETs required for the application. Two IXFN 100N50P [77] N-Channel devices were chosen and the black lines in Figure B.3 indicate the Forward Biased Safe Operating Area (FBSOA) for dc operation. The diagram has been annotated to show the application constraints and requirements that led to the choice of this device. The 'Required Operating Area' is shown within those constraints and is derived by mapping data from Figure B.1. The black arrows show how this area would move, within the constraints, for similarly rated, higher voltage, lower current generators.

The $1\,kW$ limit line represents the maximum power dissipation capability of the device, based on the case temperature being maintained at $25°\,C$. The MOSFET datasheet [77] states that the junction temperature should not exceed $150°\,C$ and, with the case temperature maintained at $25°\,C$, the maximum power rating is $1040\,W$. This rating is not easily achieved in practice. Each device was attached to a heatsink with fan-based air-cooling as shown in Figure B.13 and the relevant thermal resistivity values for the assembly are shown in Table B.3. For this application it was decided that, under the most onerous loading conditions, the Junction temperature (T_{jMAX}) should not be allowed to exceed $130°\,C$. Furthermore, a relatively high ambient air temperature (T_{AMB}) of $25°\,C$ was assumed. Finally, the thermal calculations were based on steady state terminal values with the thermal capacity of the heatsinks not being taken into account. Overall, the calculations are designed to err on the side of caution.

Table B.3: Thermal Values for MOSFET Assembly Design

R_{thJC} (Junction to Case)	$0.12\,°C/W$
R_{thCS} (Case to Sink)	$0.05\,°C/W$
R_{thSA} (Sink to Air)	$0.12\,°C/W$
T_{jMAX} (Junction Temperature)	$130°\,C$
T_{AMB} (Ambient Temperature)	$25°\,C$

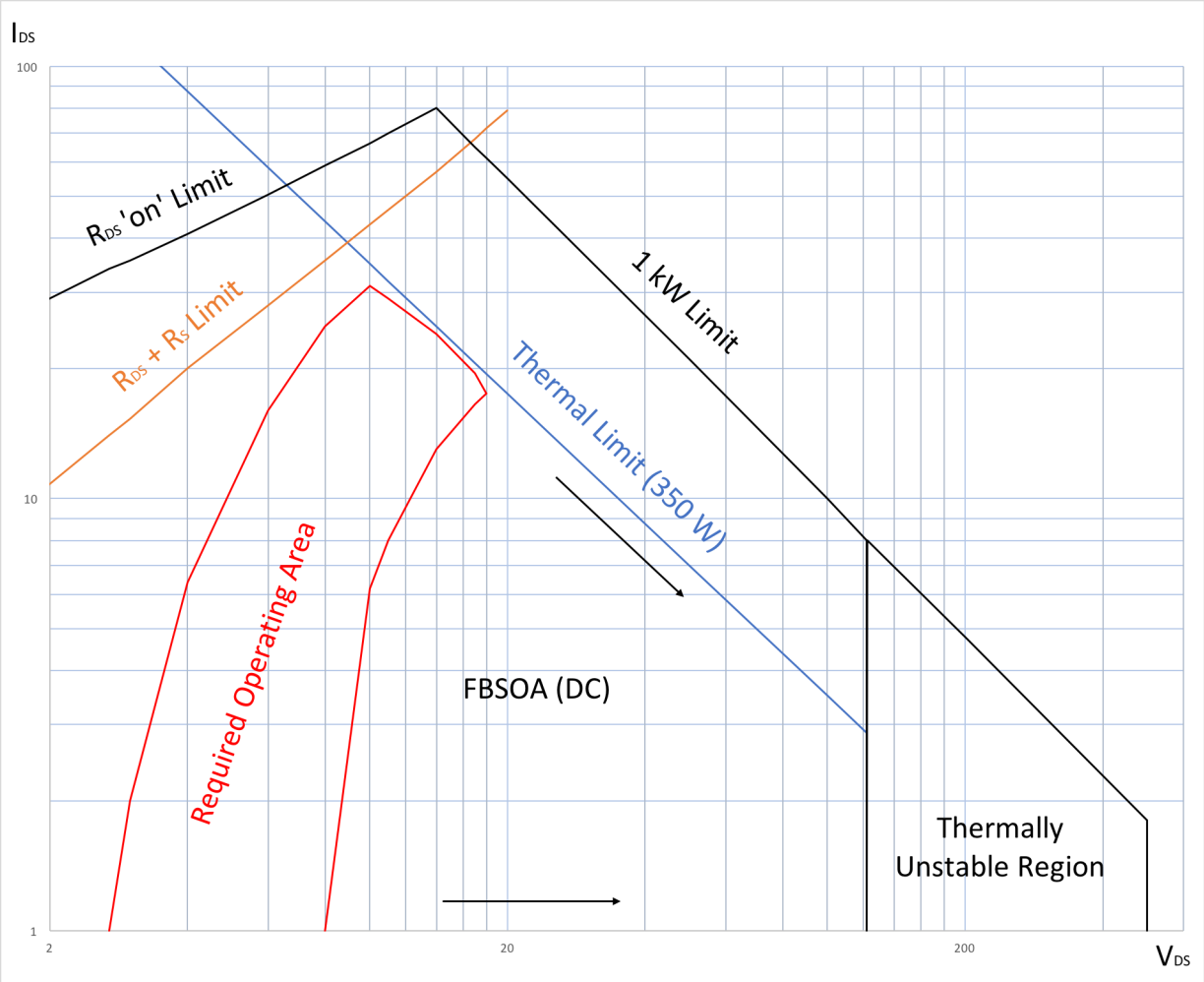

Figure B.3: FBSOA (DC) and Operational Constraints for Device IXFN 100N50P

In the steady state the maximum power dissipation is given by:

$$P_{max} = \left[\frac{T_{jMAX} - T_{AMB}}{R_{thJC} + R_{thCS} + R_{thSA}} \right] \tag{B.3}$$

where:

$P_{max} =$	Maximum Power Dissipation	(W)
$R_{thJC} =$	Junction to Case Thermal Resisitivity	$(^{\circ}C/W)$
$R_{thCS} =$	Case to Sink Thermal Resisitivity	$(^{\circ}C/W)$
$R_{thJC} =$	Sink to Air Thermal Resisitivity	$(^{\circ}C/W)$
$T_{jMAX} =$	Maximum Allowable Junction Temperature	$(^{\circ}C)$
$T_{AMB} =$	Ambient Air Temperature	$(^{\circ}C)$

Substituting the values from Table B.3 into (B.3) gives:

$$\begin{aligned} P_{max} &= \left[\frac{130 - 25}{0.12 + 0.05 + 0.12} \right] \\ &= 362\,W \end{aligned}$$

From Figure B.1 it can be seen that the maximum required power dissipation is $672\,W$. This exceeds the safe rating for one MOSFET, hence the requirement for two devices operating in parallel. Rounding up to the rating given in Table B.2 ($700\,W$) and dividing by two gives a requirement for each device to handle $350\,W$. This is below the $362\,W$ limit calculated above and the lower value of $350\,W$ is set as the 'Thermal Limit' line in Figure B.3.

Current measurement, for control and instrumentation purposes, is achieved using precision wire-wound resistors (two in parallel per MOSFET) attached to each heatsink. These

gold-coloured devices can be seen clearly in Figure B.13. For each MOSFET assembly the parallel resistance of the sensing resistors is $50\,m\Omega$. The required current range for the application is $(0 - 70)\,A$ or $(0 - 35)\,A$ per MOSFET assembly. This equates to output signals in the range $(0 - 1.75)\,V$.

The use of sensing resistors in series with the load has two main effects. Firstly, some of the load's required energy dissipation takes place in the resistors, especially at higher current levels. This reduces the thermal load on the MOSFETs slightly. It also had to be taken into account when mapping data from Figure B.1 to the 'Required Operating Area' illustrated in Figure B.3. Secondly, it places a further constraint on operation beyond that implied by the R_{DS} on limit in the FBSOA diagram. This limit is set by the lowest resistance value that the MOSFET may exhibit which is $49\,m\Omega$. The series sensing resistors, however, add another $50\,m\Omega$ to this value; the effect is shown by the $R_{DS} + R_S$ limit line in Figure B.3.

B.1.2 MOSFET Analogue Control

The MOSFET control circuit shown in Figure B.4 is based on an application example set out in [78]. This provided a starting point for the inner analogue control loop design required to linearise the MOSFET characteristic for use with an outer digital control system. Since two MOSFETs are required, there are two such circuits. Each exercises independent current control based on a common current demand set point (I_d).

The source-common voltage (V_{sc}), which is proportional to the drain-source current, is compared to the current demand setpoint (I_d), and the resulting error signal is subject to a very high level of proportional gain (A). The gate-common voltage (V_{gc}) is thus controlled so that the gate-source voltage (V_{gs}) brings about a change in drain-source current (I_{ds}) reducing the error signal to virtually zero.

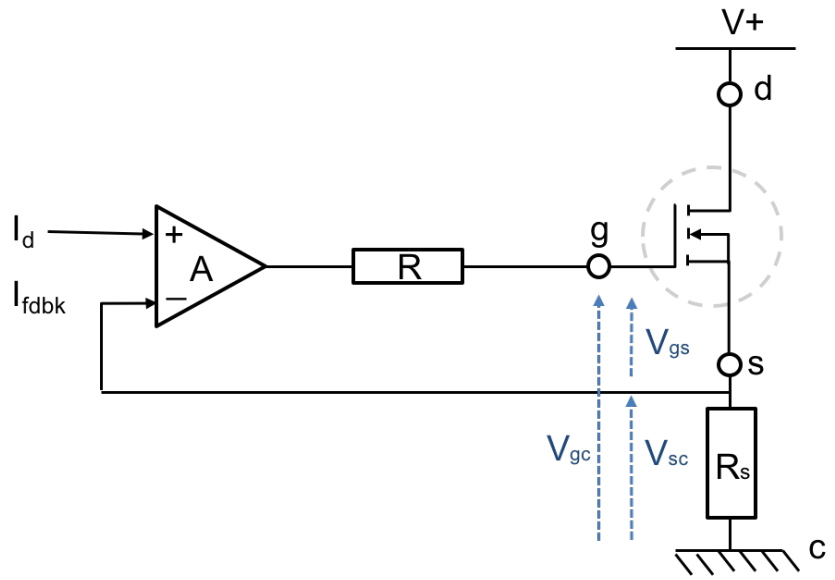

Figure B.4: Initial MOSFET Current Control Circuit

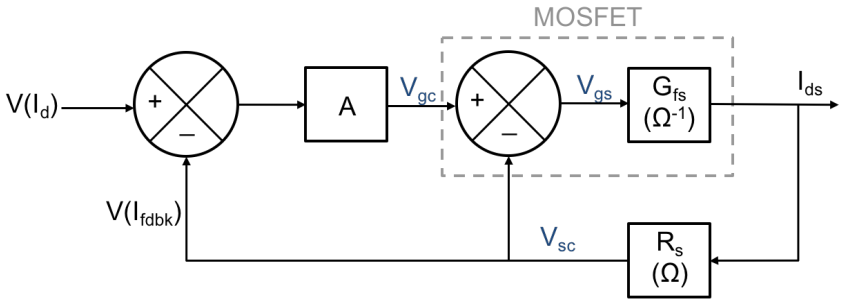

Figure B.5: Initial MOSFET Control Schematic

Tha associated control schematic diagram is shown in Figure B.5 and the transfer function is given by:

$$G(s) = \left[\frac{A\,G_{fs}}{1 + R_s\,A\,G_{fs} + R_s\,G_{fs}} \right] \tag{B.4}$$

where:

$$\begin{aligned} A = &\quad \text{Amplifier Gain} \\ G_{fs} = &\quad \text{MOSFET Transconductance} \qquad (\Omega^{-1}) \\ R_s = &\quad \text{Sensing Resistor Value} \qquad (\Omega) \end{aligned}$$

It can be seen that the term $(R_s\, G_{fs})$ appears in the denominator due to the sensing resistor arangement. This is because changes in I_{ds} affect V_{gs} due to associated variations in volt-drop (V_{sc}) across R_s. Since the operational amplifier gain (A) is extremely high the $(1 + R_s\, G_{fs})$ terms in the denominator can be neglected and the overall gain of the closed-loop system is effectively:

$$G(s) = \left[\frac{1}{R_s}\right] \tag{B.5}$$

From the datasheet [77], the MOSFET transconductance (G_{fs}) varies between $(10-60)\,\Omega^{-1}$ depending on drain-source current and Junction Temperature. The transconductance of the closed loop system with a sense resistor value of $50\,m\Omega$ is virtually constant,however, at $20\,\Omega^{-1}$ per device or $40\,\Omega^{-1}$ (ie. $40\,AV^{-1}$) for the complete assembly.

The system was built and initial cursory tests were carried using a Hameg HMP4040 Programmable DC Power Supply [79] and handheld instruments designed for analogue use. Values for drain-source current appeared to accurately correspond to the setpoint values across the required range of operation. When further tests were carried out, using a fast ADC via the chosen microcontroller, however, it became clear that the arrangement was inadequate. Sampled values varied significantly, and apparently randomly, rendering the feedback signal of no use for control purposes. Using an oscilloscope, it was discovered that,

in addition to the desired dc current value, a superimposed high frequency noise component was present. The MOSFET control circuit was modified to include a PI controller in the forward path and it was quickly established that any degree of proportional control introduced noise onto the current output. It was concluded that the presence of inductive reactance in the DC power supply resulted in slow response times relative to the controlling action. To slow down control action, an integral controller, giving a closed-loop minimum bandwidth of approximately twenty times that of the required outer digital control system, was introduced. Since the WTE is required to reproduce blade-torque ripple up to $10\,Hz$ the required outer loop bandwith was $40\,Hz$. The required minimum inner-loop bandwidth value was, therefore, $800\,Hz$.

Replacing the gain term in Figure B.5 with an integrator yields the following transfer function:

$$G(s) = \left[\frac{A\,G_{fs}}{s(1 + R_s\,G_{fs}) + R_s\,A\,G_{fs}}\right] \tag{B.6}$$

The 's' coefficient $(1 + R_s\,G_{fs})$ is necessarily greater than unity and its presence moves the s-plane pole position to the right reducing system bandwidth. It was decided to remove these terms from the transfer function by compensating for the effects of volt-drop across R_s as shown in Figure B.6. This leads to the simpler, equivalent control schematic shown in Figure B.7 and the corresponding transfer function is given by:

$$G(s) = \left[\frac{A\,G_{fs}}{s + R_s\,A\,G_{fs}}\right] \tag{B.7}$$

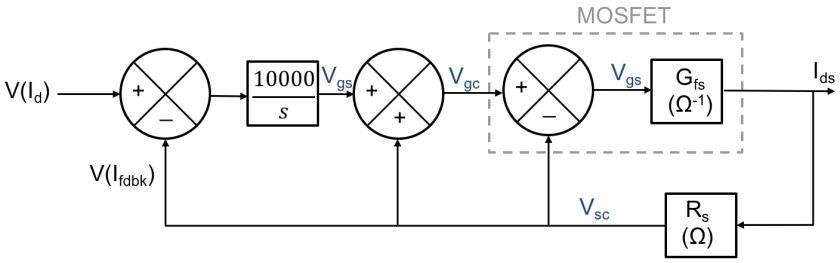

Figure B.6: Modified MOSFET Control Schematic

The sensing resistor value (R_s) is fixed at $0.05\,\Omega$ and the MOSFET transconductance (G_{fs}) is in the range $(10 - 60)\,\Omega^{-1}$. Taking a mid-range value of $30\,\Omega^{-1}$ for transconductance and setting the gain (A) at 10 000 gives an s-plane pole position of $-15\,000\,rad\,s^{-1}$. This equates to a bandwidth of approximately $2\,400\,Hz$. This varies with transconductance, however, and can thus take values from $800\,Hz$ to $4\,800\,Hz$.

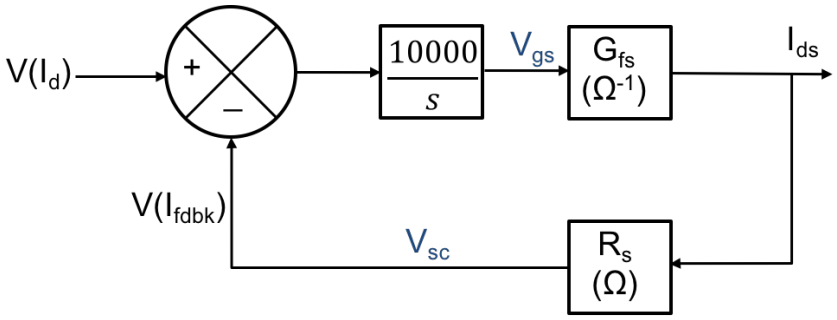

Figure B.7: Equivalent Modified Control Schematic

The control system was implemented as described, and tests across the required range of operation were repeated. It was found that the high frequency noise problem had been completely eliminated. This allowed it to be sucessfully incorporated into a digital constant current control application implemented on a microcontroller. Unfortunately, a further problem became evident once control of load resistance was implemented and attempted with the dc generator rather than the Hameg Power Supply.

B.1.3 MOSFET Biassing

As discussed in the previous section, microcontroller use facilitates flexible implementation of the specified load regimes. The Constant Resistance regime is of particular importance for testing the overall performance of the WTE system as it provides a rising linear Torque/Speed characteristic. This application monitors Load Voltage (V_{dc}) and Load Current (I_{ds}) to derive a Load Resistance feedback value for comparison with the required setpoint. Although the process variable within the digital control loop is Resistance, its value is manipulated via the current setpoint (V_{Id}) supplied to the faster acting inner analogue control loop.

The Constant Resistance regime was initially tested over the required range of operation using the Hameg dc power supply and performed as intended. The tests were then repeated using the dc generator driven by the Unidrive/Unimotor combination. To emulate the final WTE application the drive was configured for Torque control and the generator was driven with ascending torque values across the range of required load resistances. At low speeds, with corresponding low voltages, the application worked as expected. At higher speeds, and low to medium torque settings, an audible sound was evident. This resulted from speed and voltage oscillations at a frequency of approximately $400\,Hz$. Regardless of the speed or torque setting, when this phenomena occurred, the frequency was identical suggesting a resonant effect due to the disturbing effects of generator voltage noise.

MOSFETs may be operated in their 'ohmic' or 'triode' area as controllable resistors. In this region the graph of V_{ds} versus I_{ds} is approximately linear and the slope may be varied via the gate-source voltage (V_{gs}) setting. As V_{ds}, at any particular value of V_{gs}, is increased, however, the slope of the V_{ds}/I_{ds} graph decreases and becomes almost horizontal. When this happens the device is operating in the 'saturation' 'pentode' or 'pinch-off' region. Here

V_{ds} variations bring about no significant corresponding changes in I_{ds} so generator voltage noise produces associated resistance variations in the MOSFET load device. This is effectively noise superimposed on the process variable 'resistance' within the control loop. The generator is a dc, eight-brush device with a 135-segment commutator, so commutations are staggered at quarter-segment intervals across the 4-brush pairs. At a speed of 600 rpm, therefore, brush-noise pulses occur at intervals of 31 μs. The digital control system cannot deal with this disturbance since its loop time is 550 μs. It was noticed, however, that this phenomena did not occur in the MOSFET's 'ohmic' area of operation or at higher loads where a positive V_{ds}/I_{ds} slope was evident due to the more significant effects of 'channel length modulation'.

The use of drain-gate biassing is a technique used to 'straighten' the approximately linear characteristic of MOSFETs in the 'ohmic' area to improve their performance as controllable resistors [80]. Drain-gate feedback alters current flow in response to drain voltage fluctuations as would be expected in a resistive device. It was decided to use this technique to present an effective positive (resistive) slope to rapid transient voltages appearing on the generator output voltage when the MOSFET is operating in its 'saturation' region. Such biassing would not affect the more slowly varying values of V_{gs} associated with control of the process variable as feedback determines the correct value.

Figure B.8 shows the initial Drain-Gate feedback arrangement and, by superposition, the gate-common voltage (V_{gc}) is given by:

$$V_{gc} = V_{out}\left[\frac{R_2}{R_1 + R_2}\right] + V_{dc}\left[\frac{R_1}{R_1 + R_2}\right] \tag{B.8}$$

where:

$V_{gc} =$ Gate-Common Voltage

$V_{out} =$ Amplifier Output Voltage

$V_{dc} =$ Drain-Common Voltage

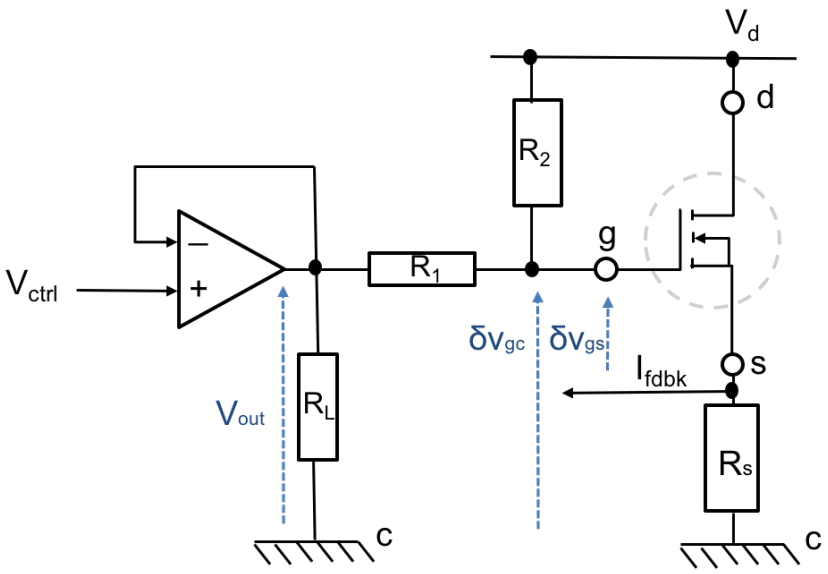

Figure B.8: Initial MOSFET Drain-Gate Feedback Circuit

In this arrangement the gate-common voltage (V_{gc}) comprises two components. A controlling voltage, due to feedback, and transient elements operating at frequencies above the capabilities of the control system. For the former, the first term in (B.8) provides the controlling action, while the magnitude of the second term is determined solely by the drain-common voltage. Transient voltages, superimposed on V_{dc}, only contribute to the second term and thus to changes (δv_{gc}) about the quiescent, controlled value of V_{gc}. Any associated changes in volt-drop across the sensing resistor (R_s), due to biassing, are compensated for by the arrangement shown in Figure B.6. The transfer function for the changes about the quiescent gate-source voltage (δv_{gs}) can, therefore, be described by

modifying the second term in (B.8) as shown below:

$$\delta v_{sc} = \delta V_{dc}\left[\frac{R_1}{R_1 + R_2}\right] \tag{B.9}$$

The second term in (B.8) limits the range of control that the system may exert over V_{gc} so values for R_1 and R_2 are constrained, since it must always be possible to turn the MOSFET 'off'. The minimum gate-threshold voltage ($V_{gs(th)}$) for the MOSFETs was determined to be no less than $4\,V$, and the highest drain-common voltage (V_{dc}), in this application, is $20\,V$. The resulting resistor value requirement is given by:

$$\frac{4}{20} > \left[\frac{R_1}{R_1 + R_2}\right] \tag{B.10}$$

Values of $10\,k\Omega$ and $50\,k\Omega$ were chosen for R_1 and R_2 respectively, providing a maximum possible contribution to gate-common voltage of $3.\dot{3}\,V$. The bias circuit improved, but did not completely eliminate, the audio frequency oscillation problem, so the circuit was modified as shown in Figure B.9. The additional, parallel RC series path provides an ac-bias path, to increase feedback for transient voltages, without compromising the dc-bias requirements. The modified transfer function is given by:

$$\frac{\delta v_{sc}}{\delta V_{dc}} = \left[\frac{sC_3(R_1R_2 + R_1R_3) + R_1}{sC_3(R_1R_2 + R_1R_3 + R_2R_3) + (R_1 + R_2)}\right] \tag{B.11}$$

The chosen values for C_3 and R_3 were $680\,nF$ and $50\,k\Omega$ respectively. This places a zero at $-14.7\,rad\,s^{-1}$ and a pole at $-25.2\,rad\,s^{-1}$ in the s-plane giving a maximum phase shift of $+15.3\,^\circ$ at $-20\,rad\,s^{-1}$. For dc components the 'gain' remains the same at $0.1\dot{6}$, however, as frequency increases the 'gain' approaches 0.286 due to the parallel combination of R_2 and R_3.

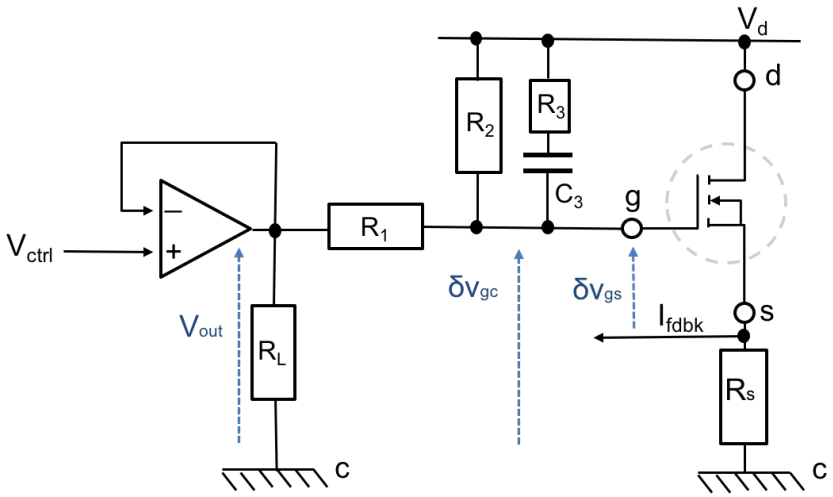

Figure B.9: Improved MOSFET Drain-Gate Feedback Circuit

Testing, over the required range of use, proved that the modification had resulted in the complete elimination of the acoustic noise problem. The biassing networks can be seen on the MOSFET assembly in Figure B.13.

B.1.4 MOSFET Digital Control

The required WTE load regimes were implemented via a digital control application running on an Arduino Due based on the SAM3XE ARM Cortex-M3 CPU. This is a 32-bit CPU device which runs at $84\,MHz$ on this device. It includes twelve ADCs and two DACs, each capable of 12-bit resolution. Independent loops are easily implemented making it particularly suitable for real-time control applications. This device was, therefore, chosen for its low cost, ease of use, and relatively high specification.

The digital controller User Interface (UI), shown in Figure B.14, comprises a two by sixteen segment LCD display and three push-buttons. Figure B.10 shows the Finite State Machine (FSM) diagram for the program. After initialisation, the user may select one of the available modes by scrolling up or down via push-buttons one and two. The selection is then

implemented via push-button three. Using push-button three again takes the user back to the selection screen, however, the previous mode continues to execute until the next chosen mode is confirmed. The current demand setpoint (V_{Id}) for the analogue controller is maintained through transitions to provide a 'bumpless' transfer. There are two main control modes, one for load current (I_Mode), the other for load resistance (R_Mode). In each case the required setpoint is adjusted via push-buttons one and two. Standby mode simply runs its inherited value for (V_{Id}) down exponentially to zero. It is also the default state running after initialisation.

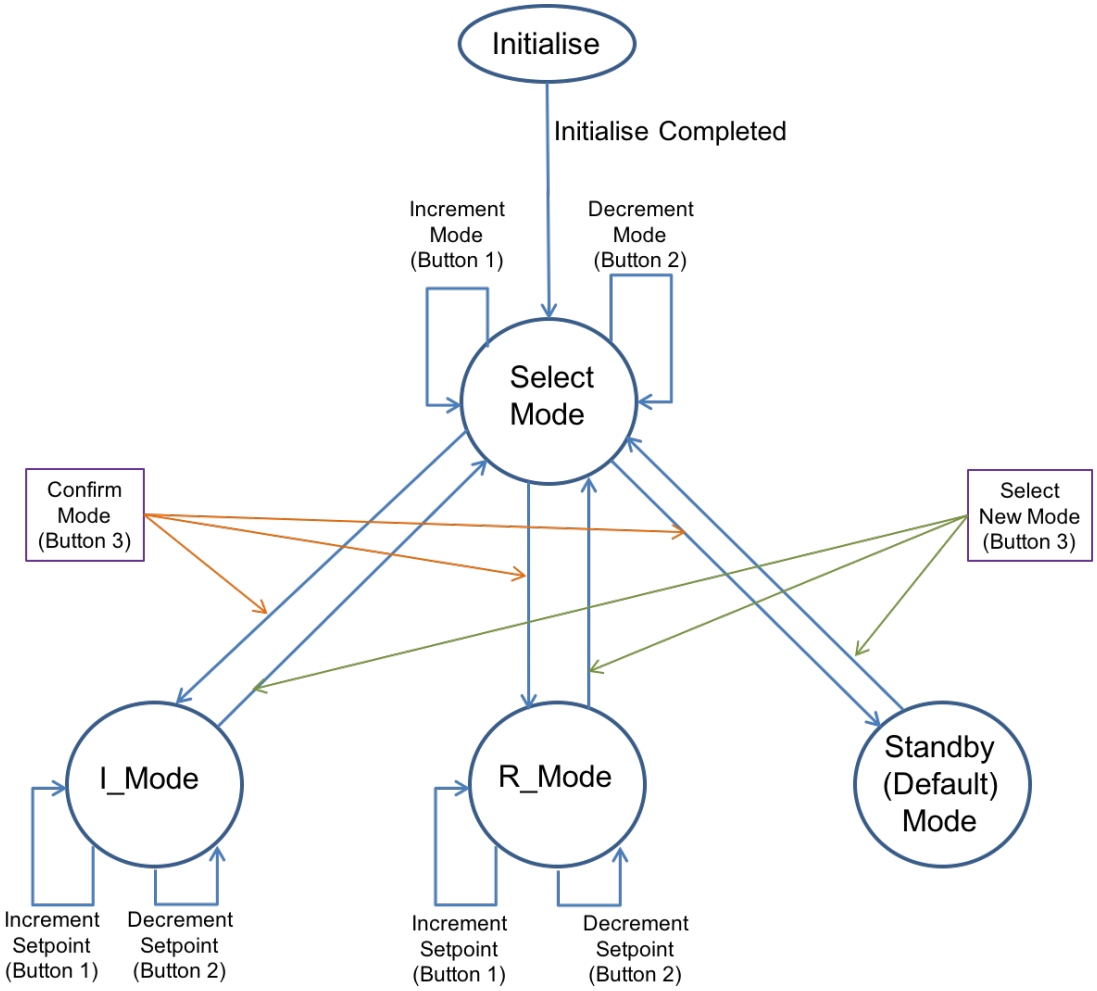

Figure B.10: Microcontroller Application FSM Diagram

Functionality is achieved using three separate program loops. Loop one runs at $2\,Hz$ and updates the display. Loop two runs at $40\,Hz$ executing actions based on the current mode, the previous mode, and push-button status. Loop three operates at $1.82\,kHz$ running the chosen real-time control algorithm. This loop 'yields' to the other processes during a defined 'delay' period.

The Current and Resistance algorithms are based on the same 'backward-integrating' PI-control transfer function of the form:

$$H(z) = \frac{X(z)}{E(z)} = k_p\left[1 + \frac{\Delta t}{T_i}\Big(\frac{1}{1 - z^{-1}}\Big)\right] \tag{B.12}$$

where:

$$\begin{aligned} X(z) &= \text{ Controller Output} \\ E(z) &= \text{ Controller Input (Error Signal)} \\ \Delta t &= \text{ Sampling Interval} \\ T_i &= \text{ Integral Time} \\ k_p &= \text{ Proportional Gain} \end{aligned}$$

Rearranging gives:

$$X(z) = z^{-1}X(z) + k_p\Big[E(z)(1 + k_i) - z^{-1}E(z)\Big] \tag{B.13}$$

where:

$$k_i = \frac{\Delta t}{T_i} = \text{Integral Gain}$$

(B.13) leads to the following difference equation used for programming:

$$x_{[m]} = x_{[m-1]} + k_p[e_{[m]}(1 + k_i) - e_{[m-1]}] \tag{B.14}$$

Figure B.11 shows the overall control schematic for the programmable load system. $H(z)$ is the transfer function for the digital controller given by (B.12) and $Z[G(s)]$ is the pulse-transfer function for the inner analogue control system whose transfer function is $G(s)$ as given in (B.7).

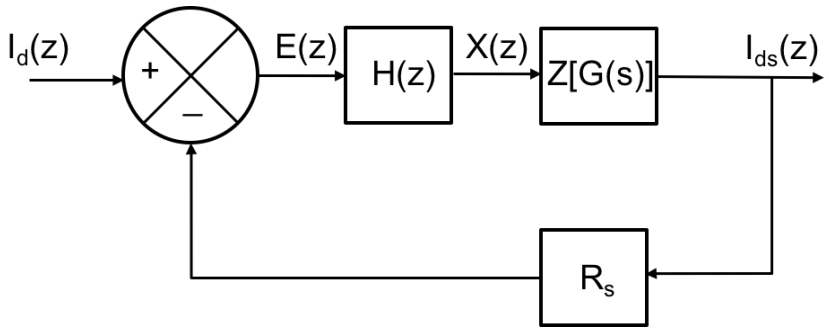

Figure B.11: Digital Control Loop Schematic

The controller settings used are:

$$\Delta t = 550\,\mu\,s$$

$$T_i = 227\,\mu\,s$$

$$k_p = \ 0.06$$

Giving:

$$H(z) = 0.1922\left[\frac{z - 0.3122}{z - 1}\right] \tag{B.15}$$

The inner, analogue, control loop comprises two, parallel, MOSFET assemblies so the

transconductance value (G_{fs}) used to derive $G(s)$ is doubled. The lowest value of $10\,\Omega^{-1}$ per assembly, associated with the lowest possible bandwidth, has been used in the following calculation. The required parameter values (A) and (G_{fs}) are, therefore, 10 000 and $20\,\Omega^{-1}$ respectively giving the following transfer function:

$$G(s) = 40\left[\frac{5000}{s+5000}\right] \tag{B.16}$$

The pulse-transfer function $G(z)$ is given by:

$$\begin{aligned} G(z) &= \left[\frac{z-1}{z}\right] \times \mathcal{Z}\left[\frac{40\times 5000}{s(s+5000)}\right] \\ &= \left[\frac{40(1-e^{-5000\,\Delta t})}{z-e^{-5000\,\Delta t}}\right] \\ &= \left[\frac{40\times 0.936}{z-0.0639}\right] \end{aligned} \tag{B.17}$$

$$\Rightarrow G(z) \approx \left[\frac{40}{z}\right] \tag{B.18}$$

The approximation to a single-step delay, given by (B.18), improves at higher, more typical, values of G_{fs}. Substituting these transfer functions, and the combined parallel value for R_s of $0.025\,\Omega$ yields the control schematic shown in Figure B.12. The overall transfer function is, therefore, given by:

$$Y(z) = \frac{I_d(z)}{I_{ds}(z)} = \left[\frac{7.6872(z - 0.3122)}{(z + 0.0685)(z - 0.8763)} \right] \tag{B.19}$$

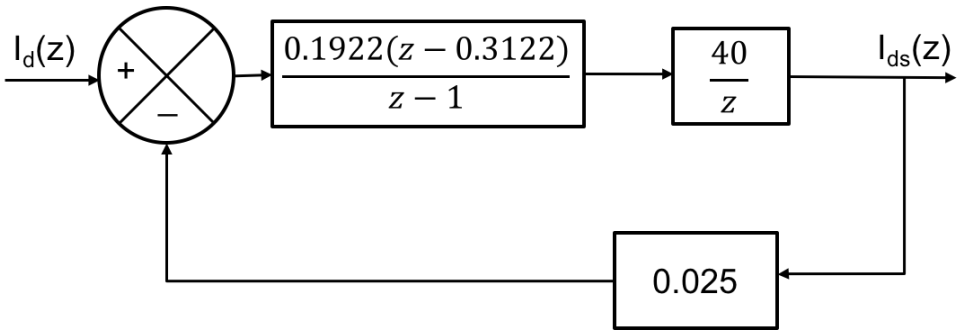

Figure B.12: Digital Control Loop Values

The estimated bandwidth of the mechanical system to be emulated is $1.01\,Hz$. The WTE application is, however, intended to replicate blade-torque ripple up to a maximum frequency of $10\,Hz$. Substituting for z in (B.19), with a sampling frequency of $1818\,Hz$, gives a gain of $-0.287\,dB$ ($-3.25\,\%$) and a phase shift of $-15°$. This level of performance from the programmable load controller was considered to be adequate for the application.

B.1.5 Signal Conditioning

Figure B.16 shows the detailed subsystem interface requirements for the Programmable Load. The Signal Conditioning/Analogue Control subsystem interfaces with the MOSFET Assembly, the Arduino Due, and a DAQ card associated with the WTE. There is no requirement for negative voltages so the design utilises LM324-N operational amplifiers with single positive supplies. These devices operate from $0\,V$ to $(V^+ - 1.5\,V)$ where V^+ is the supply voltage. A 'mains' to $24\,V$ dc switched-mode power supply feeds the PSU which, in turn, provides supplies at $+15\,V$, $+12\,V$ and $+5\,V$. The $15\,V$ supply is used to interface with the MOSFET Assembly and limits the maximum gate-common voltage (V_{gc})

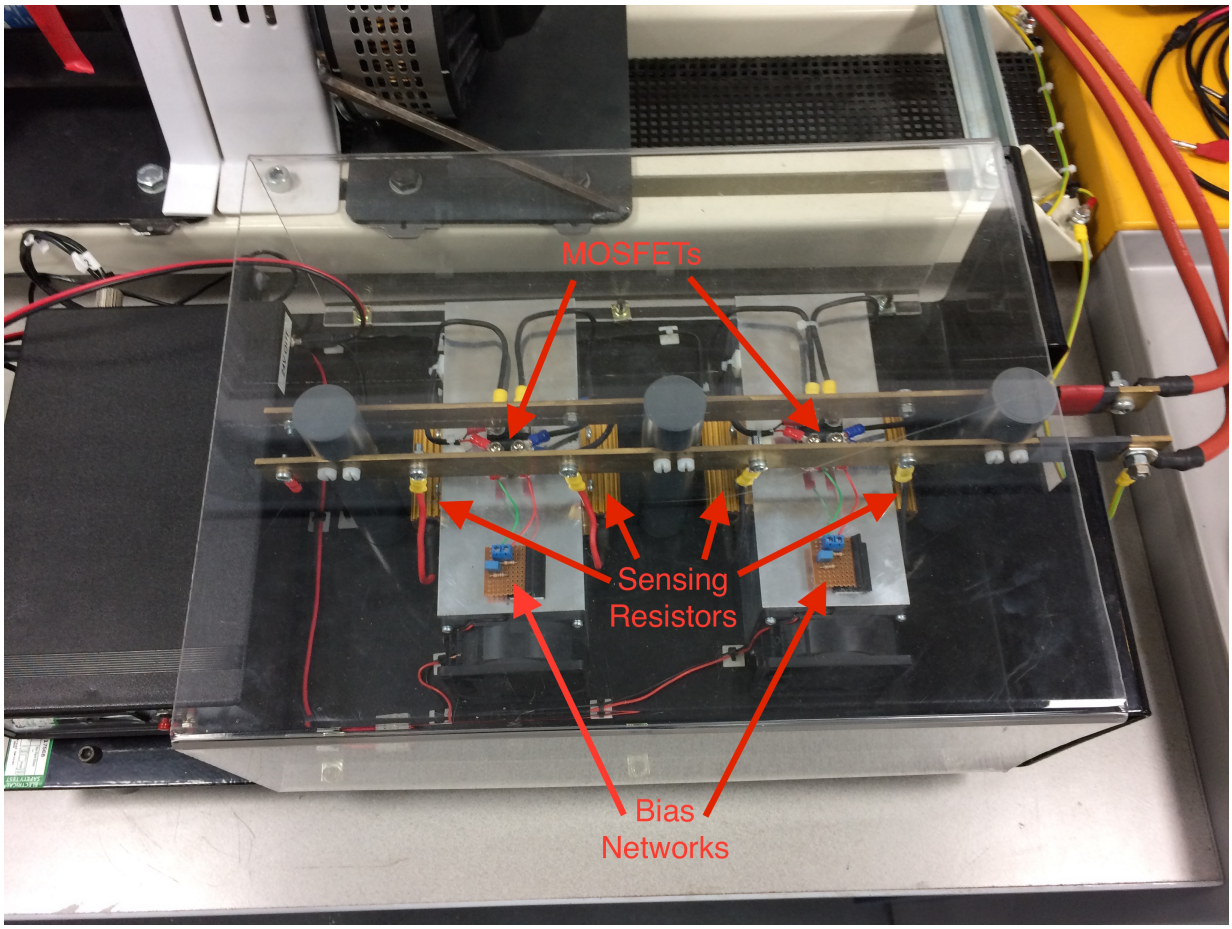

Figure B.13: MOSFET Load Assembly

(a) Select Mode Screen

(b) Resistance Mode

Figure B.14: Controller Front-Panel

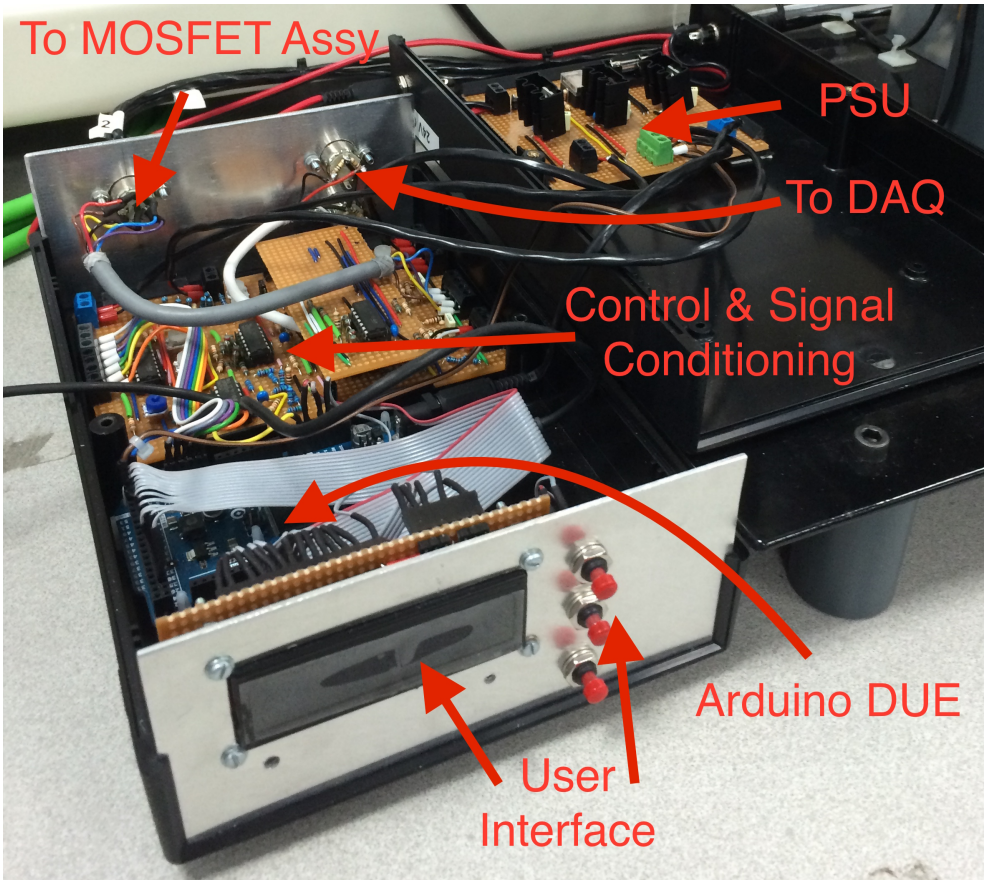

Figure B.15: Programmable Load Control Box

to $13.5\,V$ which is within the MOSFET rating and sufficient for the application. DAQ analog inputs are specified to be in the range $\pm\,10\,V$ so the $12\,V$ supply is used here restricting the output voltage swing to $10.5\,V$. Similarly, Arduino analog inputs are specified to be in the range $0\,V$ to $3.3\,V$, so the $5\,V$ supply is used here restricting the output voltage swing to $3.5\,V$. On power-up the Arduino turns on the heatsink fans via a relay located on the PSU board.

The digital controller, running on the Arduino, passes a common current demand setpoint (I_D) to the analogue controller associated with each MOSFET. These, in turn, control the respective gate-common voltages (V_{gc1}) and (V_{gc2}). Current feedback values (V_{s1}) and (V_{s2}) are returned separately for the analogue controllers but are summed and scaled to feedback the total generator armature current value (I_a) for the digital controller. Generator armature voltage (V_a) is also made available to the digital controller for use when operating in Resistance mode. Armature voltage and current values are also suitably scaled and made available to the WTE application via its DAQ interface.

The PSU and Signal Conditioning/Analogue Control subsystem were built and housed in a single enclosure together with the Arduino DUE and its User Interface. Figure B.15 shows a photograph of this Control Box opened for illustration.

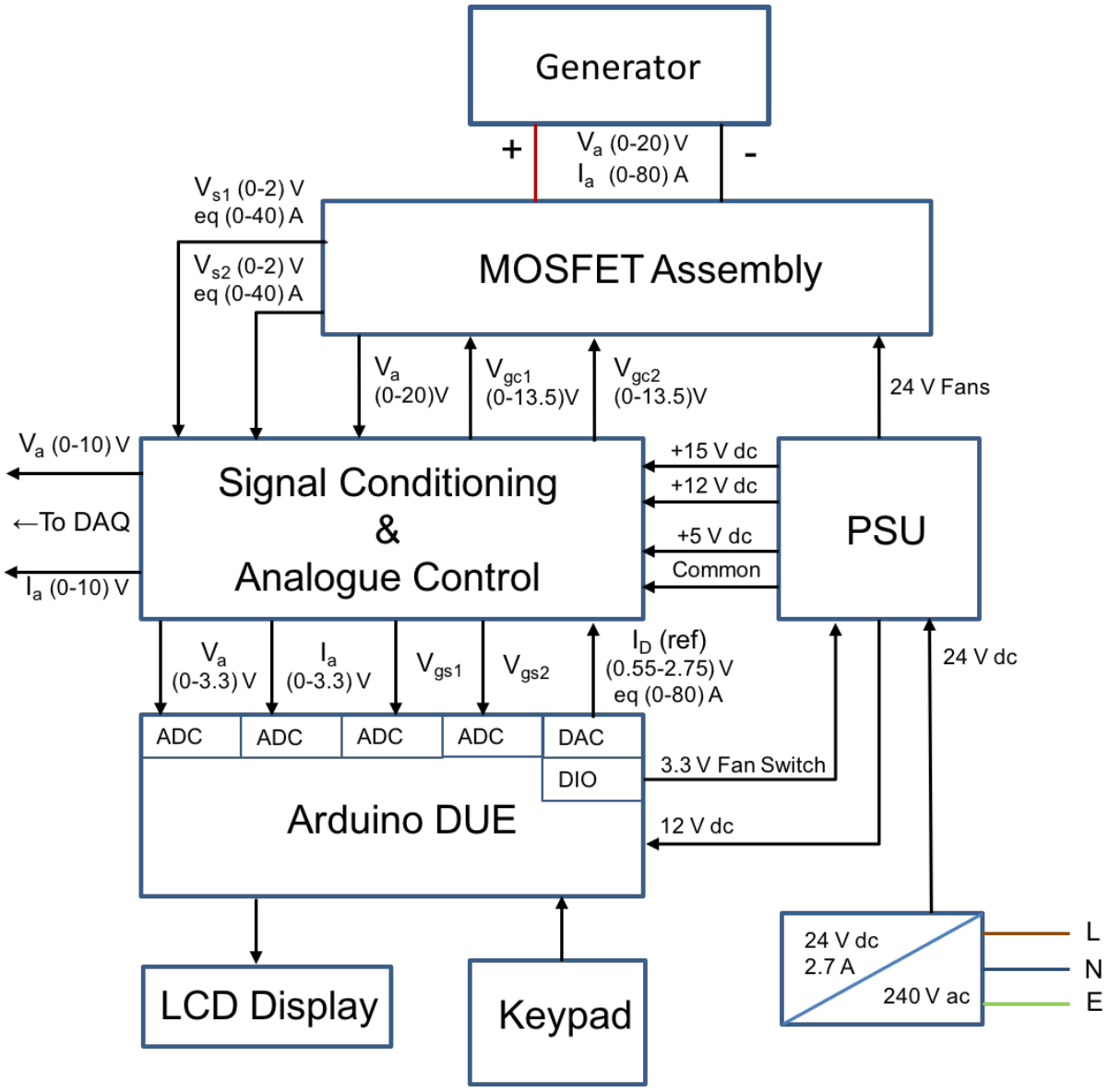

Figure B.16: Programmable Load Detailed Functional Diagram

B.2 Controller Code Listing

/*Programmable Load Program*/
/*
File: Prog_Loadv1
Author: M Dales
Version: 1.0

Settings:

Arduino Due(Programming Port)
AVRISP mkII
IDE: Arduino 1.5.6

Hardware Connections:

Programming: USB Prog Port
Power:
Power Barrel Jack 12V Plug from SC Board
3.3V to LCD VDD Grey Ribbon (2) Adj Gnd to LCD VSS Grey Ribbon (1)Red Stripe

Analog Inputs from SC Board:
A8 Total Armature Current (Ia) Orange
A9 Armature Voltage (Va) Green
A10 Mosfet 1 Gate Source Voltage (Vgs1) Purple
A11 Mosfet 2 Gate Source voltage (Vgs2) Grey
Gnd Yellow
Analog Output to SC Board:
DAC0 Current demand setpoint signal to Mosfet analog PI control (Id) White
Gnd Blue
Digital Outputs to LCD via Grey Ribbon (core no):
50 RS (3)
48 R/W(4)
46 E (5)
44 DB0 (6)
42 DB1 (7)
40 DB2 (8)
38 DB3 (9)
36 DB4 (10)
34 DB5 (11)
32 DB6 (11)
30 DB7 (12)
Digital Output to switch fans via PS Board:

53 Brown
Gnd Black
Digital Inputs via Grey Ribbon:
Reset Reset Button (17)PU Closed Low
24 Push Button 1 (16)PD Closed High
26 Push Button 2 (15)PD
28 Push Button 3 (14)PD

Program Description:

This program is intended to control the load presented to a DC generator connected to a small wind turbine or wind turbine emulator. The system operates in the following modes:
1 Select/confirm operating mode
2 Constant Current
3 Constant Resistance
4 Peak Power Tracking (Not used or tested in project)
5 Standby
In mode 2, Ia is monitored, a Current demand (Id) is derived (based on a PI algorithm) and output to the analog controller. This provides a constant load torque to the generator which can only be maintained within the output characteristics of the wind turbine (emulator). The Current setpoint may be ramped up or down by the user via pushbuttons 1 & 2. In mode 3, Armature Voltage (Va) and Current (Ia) are monitored. Load Conductance (Ia/Va) is calculated and a conductance demand (Gd) is derived (based on a PI algorithm) a corresponding current demand (Id) is then output to the analog controller. This provides a load torque characteristic that rises linearly with generator angular velocity. The Conductance setpoint may be ramped up or down by the user via pushbuttons 1 & 2. nb.The setpoint is displayed as Resistance. This alters the gradient of the load torque characteristic wrt angular velocity. In mode 5 the Current demand (Id) is ramped down exponentially from the present value to zero. The system starts up in Select mode. Any mode may be selected by the user. Transition between modes involves calculating the relevant setpoint to avoid step changes.
*/

```
//include files
#include <Scheduler.h>
#include <LiquidCrystal.h>

//function prototypes
int GetPbStatus();
void I_PI();
void G_PI();
void MPPT();
void STBY();
```

```
float IaAct();
float Gd_Act();
float P_Act();
float V_Act();
void IdOut(float Id);

//program constants
const int IaPin = 8; // select the input pin for Armature Current(Ia)8
const int VaPin = 9; // select the input pin for Armature Voltage (Va)9
const int Vgs1Pin = 10; // select the input pin for Vgs(1)
const int Vgs2Pin = 11; // select the input pin for Vgs(2)
const int FanPin = 53; // select output pin for fan control
const int IdPin = DAC0; // select the output pin for (Id)
const int Pb1Pin = 24; // select Push Button 1 input pin
const int Pb2Pin = 26; // select Push Button 2 input pin
const int Pb3Pin = 28; // select Push Button 3 input pin
const int deltaT = 500; // RT Controller loop time (microseconds)
const int ITi = 227; // Integral time (microseconds) for PI(I_Mode)
const float IkP = 0.06; // Proportional Gain for PI (I_Mode)0.2
const int GTi = 227; // Integral time (microseconds) for Conductance PI (R_Mode)
const float GkP = 0.06; // Proportional Gain for Conductance PI (R_Mode)
const float Imax = 88; // Full scale Current range
const float Vmax = 20; // Full scale Voltage range
const float Gmax = 100; // Full scale Conductance Mho (0.01 Ohms)
const float Gmin = 0.1; // Min Conductance Mho (10 Ohms)
LiquidCrystal lcd(50, 48 ,46 , 44, 42, 40, 38, 36, 34, 32, 30);
byte omega[8] = //Ohms symbol
{ B00000,
B01110,
B10001,
B10001,
B01010,
B11011,
B00000,};
byte UpDnArrow[8] = //Up Down arrow for PB1/2 symbol
{ B00100,
B01110,
B10101,
B00100,
B00100,
B10101,
B01110,
B00100};
```

```
byte RtArrow[8] = //Right Arrow for Pb3 symbol
{ B00000,
B00100,
B00010,
B11111,
B00010,
B00100,
B00000,};

//global variables
int IaValue = 0; // variable to store the value coming Ia
int VaValue = 0; // variable to store the value coming Va
int Vgs1Value = 0; // variable to store the value coming from Vgs1
int Vgs2Value = 0; // variable to store the value coming from Vgs2
int IdValue = 0; // variable to store the value going to Id

int Pb1EarlierState = 0;// Variables to store data associated with
int Pb1LastState = 0; // push button status. Inititialised outside of
int Pb1CurrState = 0; // function called by loop 2
int Pb1State = 0;
int Pb1HeldState = 0;
int Pb2EarlierState = 0;
int Pb2LastState = 0;
int Pb2CurrState = 0;
int Pb2State = 0;
int Pb2HeldState = 0;
int Pb3EarlierState = 0;
int Pb3LastState = 0;
int Pb3CurrState = 0;
int Pb3State = 0;
int Pb3HeldState = 0;

int ModeNum = 0;//Variable to store current machine mode. Initialised to Select Mode
int LastModeNum = 4;//Ensures on first entering Select IdSetPoint is controlled in STBY
int NextModeNum = 1;//Initialised to a valid value to follow select mode(2 - 4)

enum PbStateNoPB, PB1, PB1Held, PB2, PB2Held, PB3, PB3Held, MultiPB;//enumerated
variable
for PB status
enum PbState xAction;
enum ModeSELECT, I_Mode, R_Mode, P_Mode, STANDBY;//enumerated variable for
mode status
enum Mode yAction;
```

```
float IaActual = 0; //variable to store scaled and corrected current value from Ia
float IaRaw = 0; //variable to store scaled value from measurement before correction
float IaSum = 0; //Used to average Ia readings
float IaLastSum =0;
float IaNow = 0;
float VaActual = 0; //variable to store scaled voltage value from Va
float VaSum = 0;
float VaLastSum = 0;
float IaSF = (Imax/4095); //Scale Factors to convert actual values
float VaSF = (Vmax/4095);
float IdSF = (Imax/4095);
float GaActual = 0; //variable to store calculated load conductance
float Power_Watts = 0; //variable to store calculated power in Watts
float Vgs1Volts = 0; //Not necessary. Only used during program dev
float Vgs2Volts = 0; //Not necessary. Only used during program dev
float IdNow = 0; //variable to store scaled current Id demand (setpoint for Mosfet PI)
float IdLast = 0; //Previous Id demand
float GdNow = 0; //variable to store scaled conductance Gd demand
float GdLast = 0; //Previous Gd demand
float P_Now = 0; //Present Load Power
float P_Last = 0; //Previous Load Power
float deltaP = 0; //P difference
float P_Max = 800; //Max P difference
float V_Now = 0; //Present Load Voltage
float V_Last = 0; //Previous Load Voltage
float deltaV = 0; //V difference
float V_Max = 20; //Max V difference
float dP_by_dV = 0; //Rate of change of P wrt V

float IkI = (deltaT/ITi); //Integral Gain for Current PI
float IerrNow = 0; //Present Current error
float IerrLast = 0; //Previous Current error
float IdSetPoint = 0; //Amps
float IdStPtLast = 0; //Last setpoint (Amps)
float IdecFac = 0.97; //Decrement factor per iteration for IdSetPoint.(STBY Mode)
float GkI = (deltaT/GTi); //Integral Gain for Conductance PI
float GerrNow = 0; //Present Conductance error
float GerrLast = 0; //Previous Conductance error
float GdSetPoint = 0.1; //Mho (10 Ohms)
float kMPT = 0.035; //Scale Factor for dP/dV in MPPT Controlle. Max dP/dV about
50A 0.004
int DisDir = -1; //Dist direction to ensure setpoint is moved up from the bottom and down
```

```
from the top
void setup()
{
Scheduler.startLoop(loop2);
Scheduler.startLoop(loop3);
pinMode(Pb1Pin, INPUT);
pinMode(Pb2Pin, INPUT); pinMode(Pb3Pin, INPUT);
pinMode(FanPin, OUTPUT);
pinMode(DAC0, OUTPUT);
lcd.begin(16, 2);
lcd.createChar(1, omega);
lcd.createChar(2, UpDnArrow);
lcd.createChar(3, RtArrow); // use with lcd.write();
lcd.clear();
Serial.begin(9600); //for testing
digitalWrite(FanPin, HIGH); //turn the fan on
}

void loop()
{ // Display Handler updates @ 2 Hz
lcd.clear(); static void (*DispFuncPtr[5])() = Disp01,Disp02,Disp03,Disp04,Disp05;
yAction = (enum Mode) ModeNum;
(*DispFuncPtr[yAction])();
delay(500);
}

void loop2()
{ // Faster Loop. Determine and execute actions depending on mode and pushbutton
status
static void (*funcPtr[8][5])()=

Act00,Act01,Act02,Act03,Act04,
Act10,Act11,Act12,Act13,Act14,
Act20,Act21,Act22,Act23,Act24,
Act30,Act31,Act32,Act33,Act34,
Act40,Act41,Act42,Act43,Act44,
Act50,Act51,Act52,Act53,Act54,
Act60,Act61,Act62,Act63,Act64,
Act70,Act71,Act72,Act73,Act74
;
xAction =(enum PbState) GetPbStatus();
yAction = (enum Mode) ModeNum;
(*funcPtr[xAction][yAction])();
```

```
delay(25);
}

void loop3() //Fastest Loop
{
if (ModeNum == 2 || LastModeNum == 2) G_PI();//Call Conductance PI control.
else I_PI(); //Call Current PI control for anything else. Current setpoint provided
globally.
//delay(20);
delayMicroseconds(deltaT);
yield();
}

//function definitions
/* GetPbStatus
Purpose: To read and debounce 'fleeting' pushbutton presses
and to detect 'held' pushbuttons.
Parameters:None passed, input derived from digital reads.
Return Value:Integer value in the range 0 to 7
0 = No buttons pressed
1 = Pb1 only
2 = Pb1 held
3 = Pb2 only
4 = Pb2 held
5 = Pb3 only
6 = Pb3 held
7 = Multiple buttons pressed
*/
int GetPbStatus()
{
Pb1EarlierState = Pb1LastState;
Pb1LastState = Pb1CurrState;
Pb1CurrState = digitalRead(Pb1Pin);
if ((Pb1CurrState == 1 && Pb1LastState == 1) && (Pb1EarlierState != 1))
{
Pb1State = 1;
Pb1HeldState = 0;
}
else if ((Pb1CurrState == 1 && Pb1LastState == 1) && (Pb1EarlierState == 1))
{
Pb1State = 1;
Pb1HeldState = 1;
```

```
}
else
{
Pb1State = 0;
Pb1HeldState = 0;
}
//Determine Pb2 state including 'held' status
Pb2EarlierState = Pb2LastState;
Pb2LastState = Pb2CurrState;
Pb2CurrState = digitalRead(Pb2Pin);
if ((Pb2CurrState == 1 && Pb2LastState == 1) && (Pb2EarlierState != 1))
{
Pb2State = 1;
Pb2HeldState = 0;
}
else if ((Pb2CurrState == 1 && Pb2LastState == 1) && (Pb2EarlierState == 1))

Pb2State = 1;
Pb2HeldState = 1;
}
else
{ Pb2State = 0;
Pb2HeldState = 0;
}
//Determine Pb3 state including 'held' status
Pb3EarlierState = Pb3LastState;
Pb3LastState = Pb3CurrState;
Pb3CurrState = digitalRead(Pb3Pin);
if ((Pb3CurrState == 1 && Pb3LastState == 1) && (Pb3EarlierState != 1))
{
Pb3State = 1;
Pb3HeldState = 0;

else if ((Pb3CurrState == 1 && Pb3LastState == 1) && (Pb3EarlierState == 1))
{
Pb3State = 1;
Pb3HeldState = 1;
}
else
{
Pb3State = 0;
Pb3HeldState = 0;
}
```

```
//Derive return value
if (!(Pb1State == 1 || Pb2State == 1 || Pb3State ==1) == 1)
{
return 0;//No Pbs pressed
}
else if ((Pb1State == 1) && (!(Pb2State ==1 || Pb3State ==1 || Pb1HeldState ==1)
== 1))

return 1;//Pb1 only
}
else if ((Pb1HeldState == 1) && (!(Pb2State == 1 || Pb3State == 1)== 1))
{
return 2;//Pb1 held
else if ((Pb2State == 1) && (!(Pb1State == 1 || Pb3State == 1 || Pb2HeldState ==1)
== 1))
{
return 3;//Pb2 only
}
else if ((Pb2HeldState == 1) && (!(Pb1State == 1 || Pb3State == 1)== 1))
{
return 4;//Pb2 held
}
else if ((Pb3State == 1) && (!(Pb1State == 1 || Pb2State == 1 || Pb3HeldState ==1)
== 1))
{
return 5;//Pb3 only
}
else if ((Pb3HeldState == 1) && (!(Pb1State == 1 || Pb2State == 1)== 1))
{
return 6;//Pb3 held
}
else
{
return 7;//Multiple buttons pressed
}
}
//PI Current Controller
void I_PI()
{
IerrLast = IerrNow;
IerrNow = (IdSetPoint - IaAct());
IdLast = IdNow;
IdNow = IdLast + IkP*(IerrNow*(1 + IkI) - IerrLast);
```

```
IdNow = constrain(IdNow,0,Imax);//Apply bounds
IdOut(IdNow);
//IdOut(IdSetPoint);
}
//Get current scaled Ia value
float IaAct()
{
IaSum = 0;
IaLastSum = 0;
for (int x = 0; x ¡ 4; x++)
{
IaLastSum = IaSum;
analogReadResolution(12);
IaNow = analogRead(IaPin);
IaSum = IaLastSum + IaNow;
delayMicroseconds(10);
} IaRaw = ((IaSum/4)*IaSF);
IaActual = ((0.0003*pow(IaRaw, 2))+(0.9794*IaRaw)+0.3084);//correction for non linearity in sig cond.

return(IaActual);
} //Send correctly scaled Id value to analog controller
void IdOut(float Id)
{
IdValue = (Id/IdSF);
analogWriteResolution(12);
analogWrite(IdPin, IdValue);
}
//PI Conductance Controller
void G_PI()
{
GerrLast = GerrNow;
GerrNow = (GdSetPoint - GdAct());
GdLast = GdNow;
GdNow = GdLast + GkP*(GerrNow*(1 + GkI) - GerrLast);
GdNow = constrain(GdNow,Gmin,Gmax);//Apply bounds
IdNow = (GdNow*VaActual);
IdNow = constrain(IdNow,0,Imax);//Apply bounds
IdOut(IdNow);
}
//Get current correctly scaled G load value (mohs)
float GdAct()
{
```

```
IaActual = IaAct();
VaActual = V_Act();
VaActual = constrain(VaActual,0.001,Vmax);//Avoid 'ill-conditioned' calcs
GaActual = (IaActual/VaActual);
return (GaActual); //Return Load Conductance(Mhos)
}
//MPPT Controller
void MPPT()
{
if (IdSetPoint < 2) DisDir = -1;
else DisDir =1;
P_Last = P_Now;
P_Now = P_Act();
deltaP = (P_Now - P_Last);//dP/dt
deltaP = constrain (deltaP,-P_Max,P_Max);
V_Last = V_Now;
V_Now = V_Act();
deltaV = (V_Now - V_Last);//dV/dt
deltaV = constrain (deltaV,-V_Max,V_Max);
if (abs(deltaV) < 0.1) deltaV = 0.1;//Avoids 'ill-conditioned' calcs
dP_by_dV = (deltaP/deltaV);//Max for this system is 50A. Min for effect 1A.
if (abs(dP_by_dV) < 0.0001) dP_by_dV = 0.05*DisDir;//V will always be 'disturbed' to
obtain a subsequent valid dP/dV
IdStPtLast = IdSetPoint;
IdSetPoint = IdStPtLast - kMPT * dP_by_dV;//Constant kMPT constrains rate of change
of IdSetPoint wrt time.
IdSetPoint = constrain(IdSetPoint,0,Imax);
}

//Get current correctly scaled P load value
float P_Act()
{
IaActual = IaAct();
VaActual = V_Act();
return (VaActual*IaActual); //Return Load Power (Watts)
}
//Get current correctly scaled V load value
float V_Act()
{
VaSum = 0;
VaLastSum = 0;
for (int x = 0; x < 4; x++)
{
```

```
VaLastSum = VaSum;
analogReadResolution(12);
VaValue = analogRead(VaPin);
VaSum = VaLastSum + VaValue;
delayMicroseconds(10);
}
/*
analogReadResolution(12);
VaValue = analogRead(VaPin);
*/
VaActual = ((VaSum/4)*VaSF);//Convert to Volts
return (VaActual); //Return Load Voltage
}
//STBY Controller
void STBY()
{
IdSetPoint = (IdSetPoint*IdecFac); //run setpoint down
}
//Display Functions
void Disp01()
{
lcd.print("Select NextMode");
lcd.write(2);
lcd.setCursor(0,1);
lcd.print("Confirm ");
lcd.write(3); if (NextModeNum == 1) lcd.print("AMPS");
else if (NextModeNum == 2) lcd.print("OHMS");
else if (NextModeNum == 3) lcd.print("MPPT");
else if (NextModeNum == 4) lcd.print("STBY");
else lcd.print("????"); //shouldn't happen
lcd.write(3);
}
void Disp02()
{
lcd.print("StPt");
lcd.write(2);
lcd.setCursor(5,0);
lcd.print(IdSetPoint,2);
lcd.setCursor(10,0);
lcd.print("A");
lcd.write(3);
lcd.print("MODE");
lcd.setCursor(0,1);
```

```
lcd.print("Meas:");
lcd.setCursor(5,1);
if (IaAct() < 0.31) lcd.print("LOW.");
else lcd.print(IaAct(),2);
lcd.setCursor(10,1);
lcd.print("A");
lcd.print(" AMPS");
}
void Disp03()
{
lcd.print("StPt");
lcd.write(2);
lcd.setCursor(5,0);
lcd.print(1/GdSetPoint,2);
lcd.setCursor(10,0);
lcd.write(1);
lcd.write(3);
lcd.print("MODE");
lcd.setCursor(0,1);
lcd.print("Meas:");
lcd.setCursor(5,1);
lcd.print(1/(GdAct()),2);
lcd.setCursor(10,1);
lcd.write(1);
lcd.print(" Ohms");
}
void Disp04()
{
lcd.print("MODE: ");
lcd.write(3);
lcd.print("MPPT");
lcd.setCursor(0,1);
lcd.print("Power:");
lcd.print(P_Act(),1);
lcd.setCursor(11,1);
lcd.print("Watts");
}
void Disp05()
{
lcd.print("StPt");
lcd.write(2);
lcd.setCursor(5,0);
lcd.print(IdSetPoint,2);
```

```
lcd.setCursor(10,0);
lcd.print("A");
lcd.write(3);
lcd.print("MODE");
lcd.setCursor(0,1);
lcd.print("Meas:");
lcd.setCursor(5,1);
if (IaAct() ¡ 0.31) lcd.print("LOW.");
else lcd.print(IaAct(),2);
lcd.setCursor(10,1);
lcd.print("A");
lcd.print(" STBY");
}
void Act00()
{
if (LastModeNum == 3) MPPT();
else if (LastModeNum == 4) STBY();
}
void Act01() {//do nothing}
void Act02() {//do nothing}
void Act03() {MPPT();}
void Act04() {STBY();}
void Act10()
{
if (LastModeNum == 3) MPPT();
else if (LastModeNum == 4) STBY();
if (NextModeNum ¡ 4) ++NextModeNum;
else if (NextModeNum = 4) NextModeNum = 1;//Wrap
}
void Act11()
{
if (IdSetPoint <= (Imax - 0.06)) IdSetPoint = IdSetPoint + 0.06;//60 mA increments
}
void Act12()
{
if (GdSetPoint >= (Gmin + 0.005)) GdSetPoint = GdSetPoint - 0.005;// 0.5Mho incre-
ments
}
void Act13() {MPPT();}
void Act14() {STBY();}
void Act20()
{
if (LastModeNum == 3) MPPT();
```

```
else if (LastModeNum == 4) STBY();
}
void Act21()
{
if (IdSetPoint <= (Imax - 0.06)) IdSetPoint = IdSetPoint + 0.06;
}
void Act22()
{
if (GdSetPoint >= (Gmin + 0.005)) GdSetPoint = GdSetPoint - 0.005;// 0.5Mho incre-
ments
}
void Act23()/{MPPT();}
void Act24() {STBY();}
void Act30()
{
if (LastModeNum == 3) MPPT();
else if (LastModeNum == 4) STBY();
if (NextModeNum > 1) –NextModeNum;//Next mode cannot be select while in select.
else if (NextModeNum = 1) NextModeNum = 4;//Wrap
}
void Act31()
{
if (IdSetPoint >= 0.05) IdSetPoint = IdSetPoint - 0.05;
else (IdSetPoint = 0);
}
void Act32()
{
if (GdSetPoint <= (Gmax - 0.005)) GdSetPoint = GdSetPoint + 0.005;
}
void Act33() {MPPT();}
void Act34() {STBY();}
void Act40()
{
if (LastModeNum == 3) MPPT();
else if (LastModeNum == 4) STBY();
}
void Act41()
{
if (IdSetPoint >= 0.05) IdSetPoint = IdSetPoint - 0.05;
else (IdSetPoint = 0);
}
void Act42()
{
```

```
if (GdSetPoint <= (Gmax - 0.005)) GdSetPoint = GdSetPoint + 0.005;
}
void Act43() {MPPT();}
void Act44() {STBY();}
void Act50()
{
if (LastModeNum == 3) MPPT();
else if (LastModeNum == 4) STBY();
LastModeNum = ModeNum; //Last Mode becomes Select Mode
IdSetPoint = IaAct(); //Set point set to actual value to avoid step changes
GdSetPoint = Gmin;
ModeNum = NextModeNum; //Change Mode
NextModeNum = 0; //Next Mode becomes Select Mode
}
void Act51()
{
LastModeNum = ModeNum;//Last mode becomes I_Mode
ModeNum = NextModeNum;//Mode becomes Select
NextModeNum = LastModeNum;//Next defaults to last
}
void Act52()
{
LastModeNum = ModeNum;
ModeNum = NextModeNum;
NextModeNum = LastModeNum;
}
void Act53()
{
MPPT();
LastModeNum = ModeNum;
ModeNum = NextModeNum;
NextModeNum = LastModeNum;
}
void Act54()
{
STBY();
LastModeNum = ModeNum;
ModeNum = NextModeNum;
NextModeNum = LastModeNum;
}
void Act60()
{
if (LastModeNum == 3) MPPT();
```

```
else if (LastModeNum == 4) STBY();
}
void Act61() {//do nothing}
void Act62() {//do nothing}
void Act63() {MPPT();}
void Act64() {STBY();}
void Act70()
{
if (LastModeNum == 3) MPPT();
else if (LastModeNum == 4) STBY();
}
void Act71() {//do nothing}
void Act72() {//do nothing}
void Act73() {MPPT();}
void Act74() {STBY();}
```

Appendix C

LabVIEW Code

C.1 Host Front Panels

Relevant LabVIEW front panel user displays and code are reproduced here. Section C.1 shows two important user interface panels. The first is used to monitor the WTE system behaviour, the second is used to set up data capture. Section C.2 shows some important sections of real-time code used to implement emulation and carry out the improved inertia compensation algorithm.

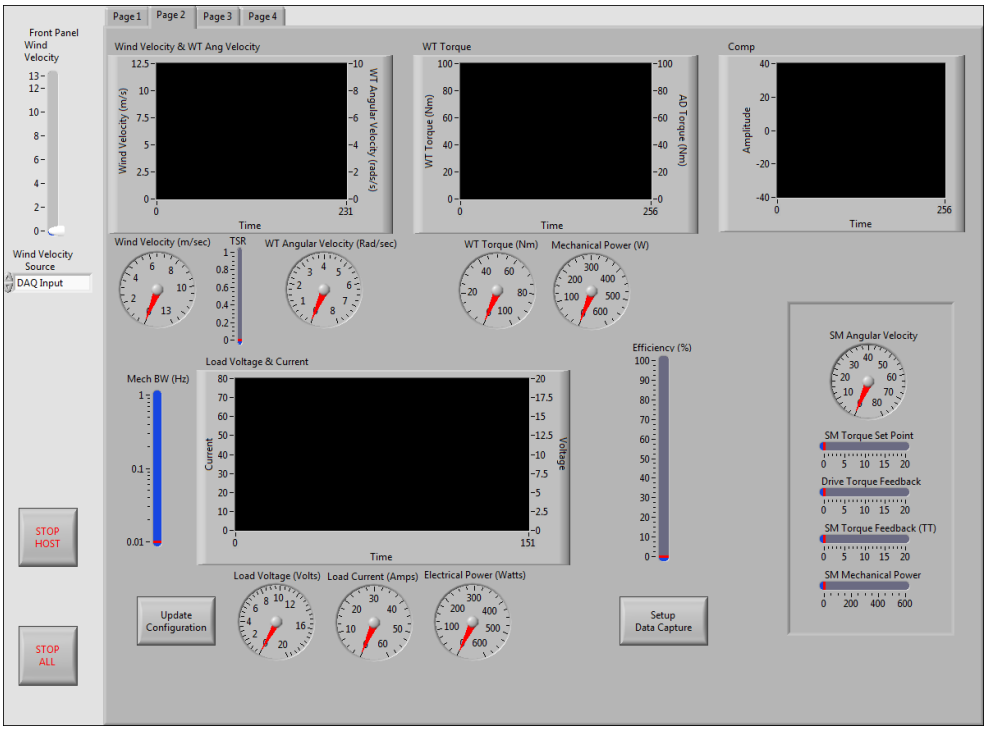

Figure C.1: Host Front Panel for Monitoring WTE System

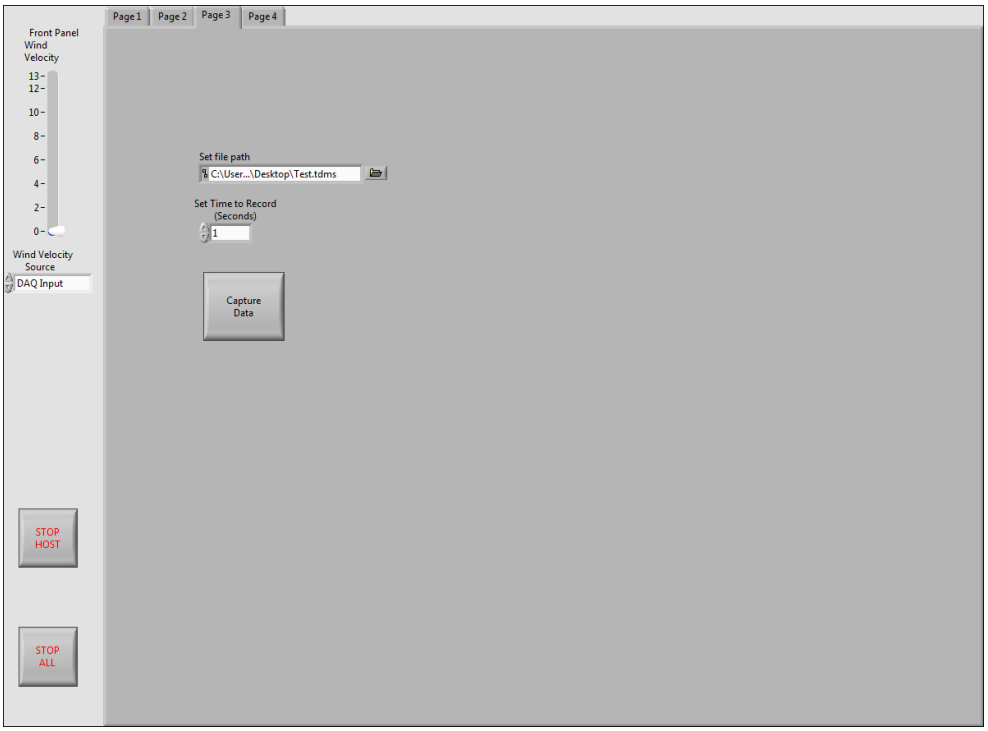

Figure C.2: Host Front Panel for Setting Up Data Capture

C.2 Real-Time WTE Code

On startup, all Network and RT Variables are initialised to meaningful values and the signal input and output Tasks are initiated. This ensures that the RT Controller can operate autonomously. Network Variables are available to, and may also be updated by, the Host system, when it is running. RT Variables operate within the RT loops. Process signals are acquired and transmitted via the NI PCI-6229 acquisition device (DAQ) mentioned in Table A.3. Signal input and output Tasks are pre-defined using the DAQMax interface to make them available to the program. These Task definitions specify the parameters to be included together with associated scalings, ranges and units.

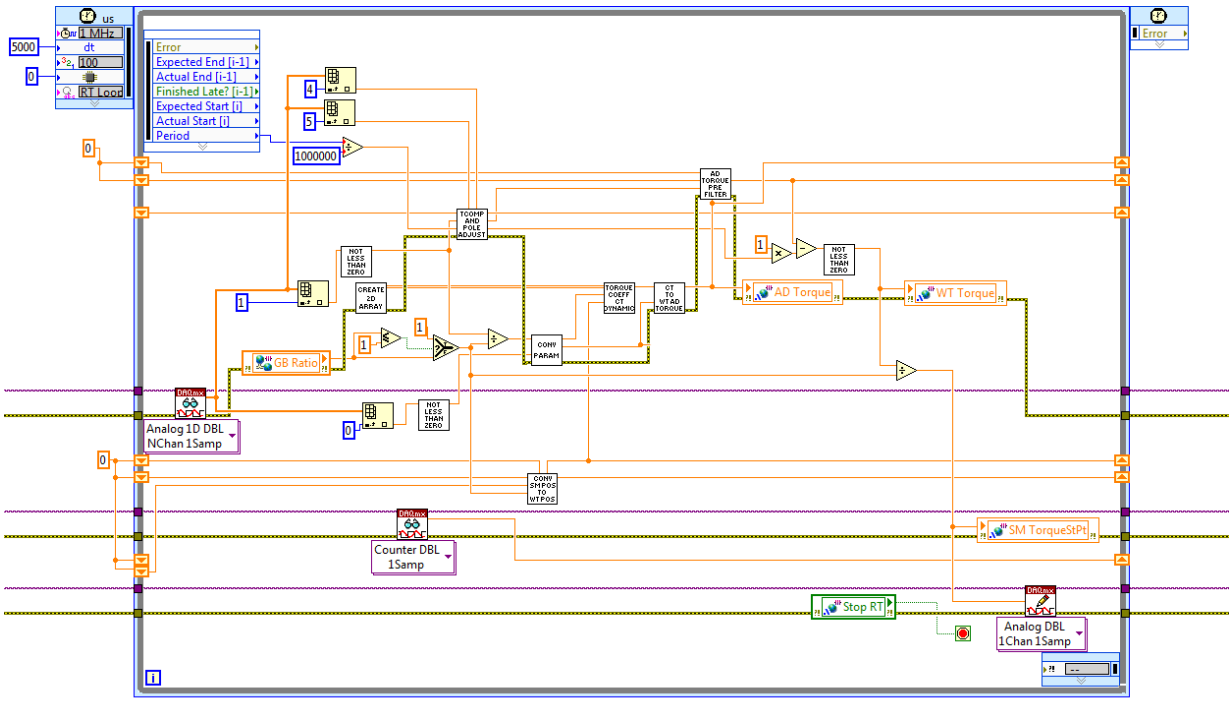

Figure C.3: WTE System Real Time Control Loop

Within the WTE control loop key tasks are implemented using 'SubVIs'. The code for these is reproduced below and their functionality explained.

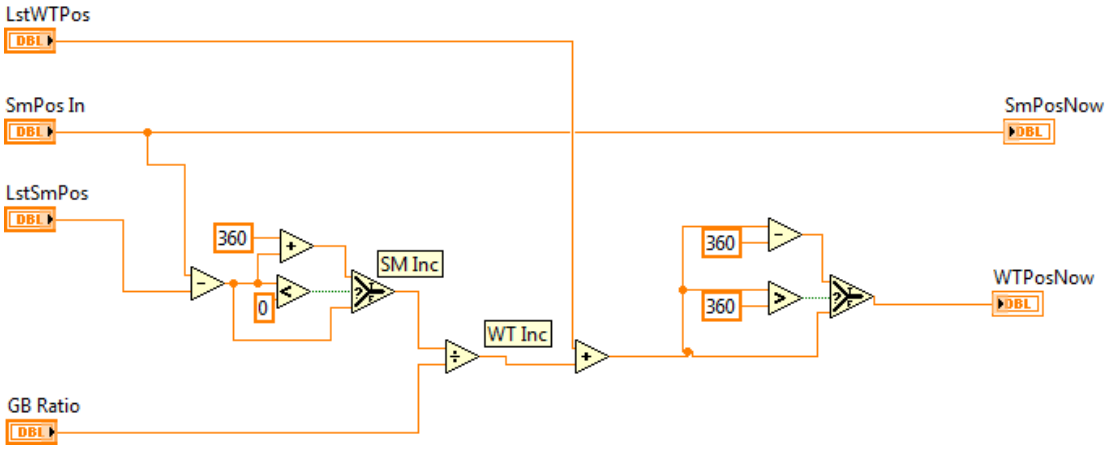

Figure C.4: SubVI to Convert Servomotor Position to Emulated WT Position

Figure C.4 shows the code to convert servomotor position to WT position based on the gearox ratio. At startup position variables are intitiated to zero and positional data relative to this point are maintained. The code handles 'rollover' for the servomotor and the WT.

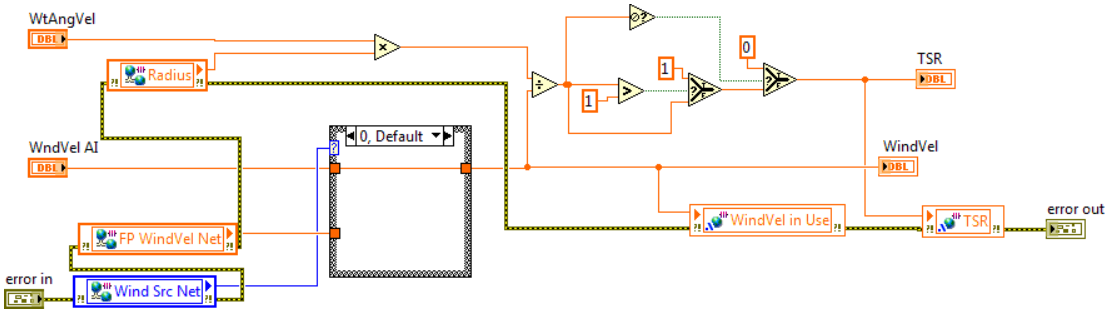

Figure C.5: SubVI to Generate WT TSR

Figure C.5 shows the code to calculate Tip Speed Ratio (λ) from wind velocity (V_w), WT angular velocity (ω) and rotor radius (R). The code constrains the maximum value to one and deals appropriately with the 'divide by zero' issue when wind velocity is zero.

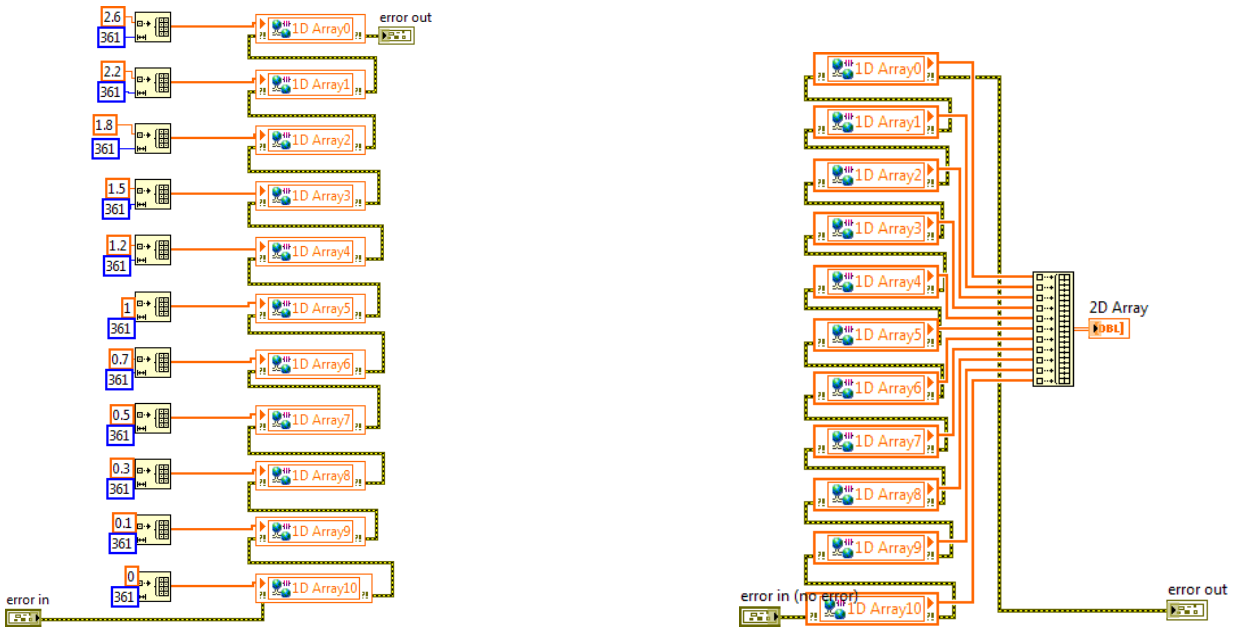

(a) Create 1-D Arrays (b) Assemble 1-D Vars

Figure C.6: SubVIs to Create 2-D Array Representing $C_t(\theta, \lambda)$

Figure C.6 shows the code used to generate the 2-D array representing $C_T(\theta, \lambda)$. Part (a) shows a SubVI executed during the initialisation process. It is not possible to pass 2-D arrays into a RT loop so a set of 1-D arrays is created and populated with valid data. Part (b) shows the creation of a 2-D array from the 1-D arrays within the RT loop. The constituent 1-D arrays, and therefore the 2-D array may be updated from the Host interface as required.

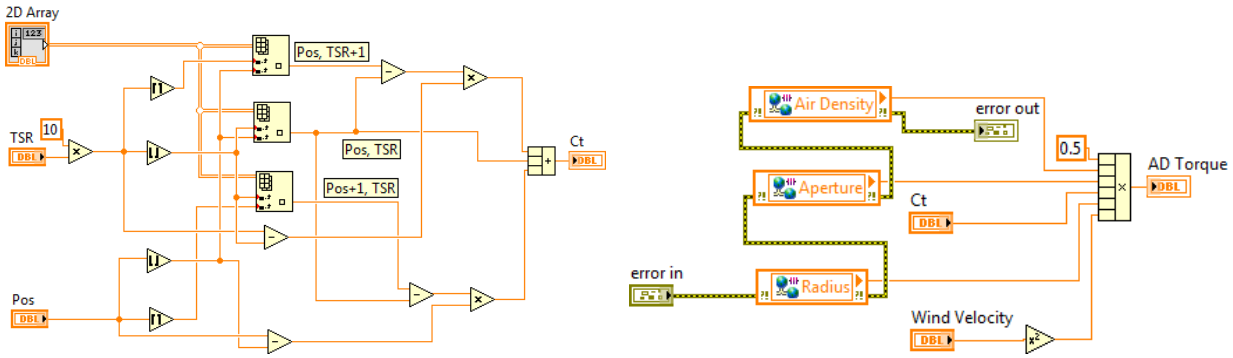

(a) Generate Torque Coefficient (b) Generate Aerodynamic Torque from C_T

Figure C.7: SubVIs to Generate Aerodynamic Torque

Figure C.7 shows how values for aerodynamic torque (T_{ad}) are derived. Firstly, part (a) shows how TSR and WT position are used to 'look up' values for Torque Coefficient (C_t) using Linear 2-D interpolation. Secondly, the SubVI in part (b) implements the formula to calculate T_{ad} from C_t.

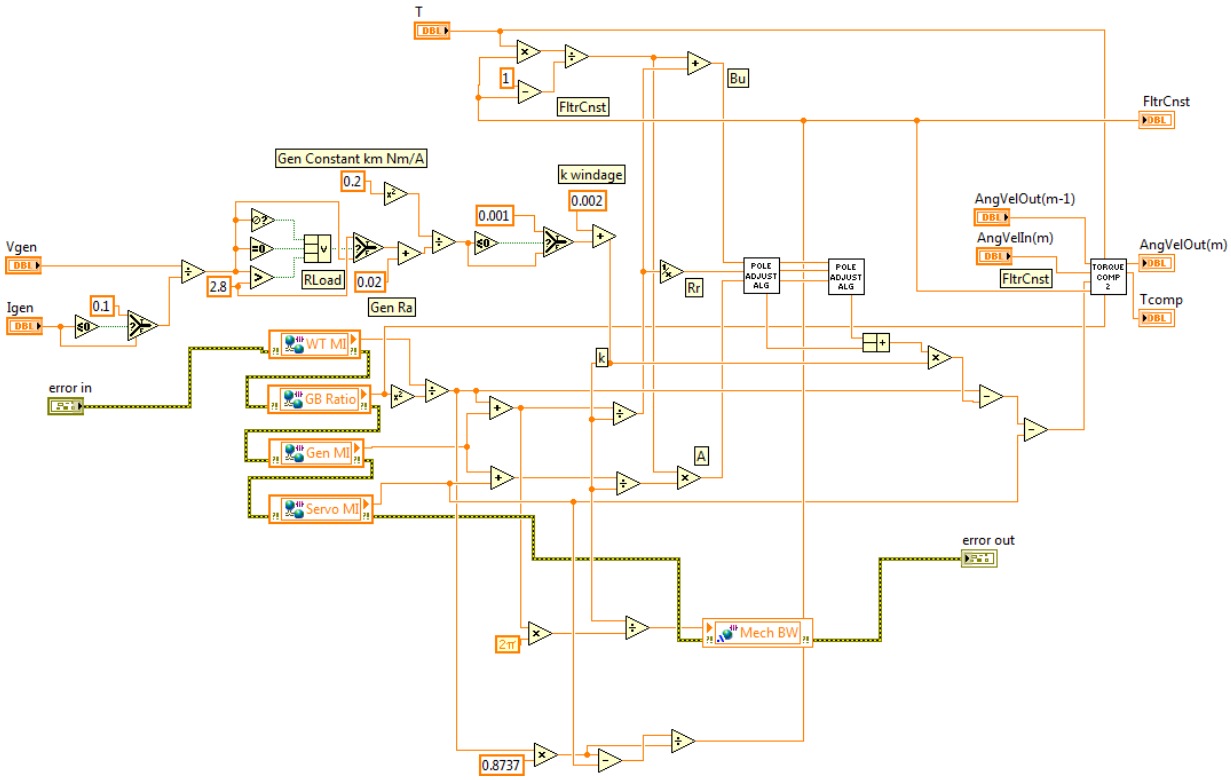

Figure C.8: Code to Adjust Main Pole and Generate T_{comp}

Figure C.8 shows the code to calculate the correct pole adjustment and subsequent generation of the required compensating torque. The subVI incorporates a system stiffness observer and further subVIs to calculate, pole adjustment, and compensating torque. The pole adjustment algorithm is implemented twice as discussed in Chapter 4 and Figure C.9 shows the details. The subVI for generating compensating torque is shown in Figure C.10.

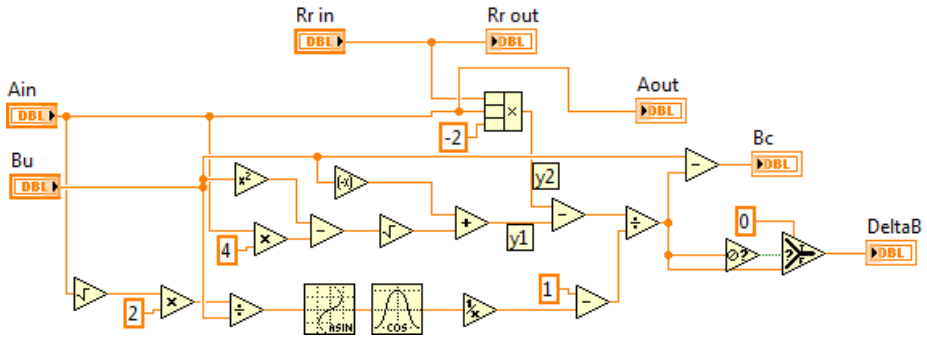

Figure C.9: Pole Adjustment Algorithm

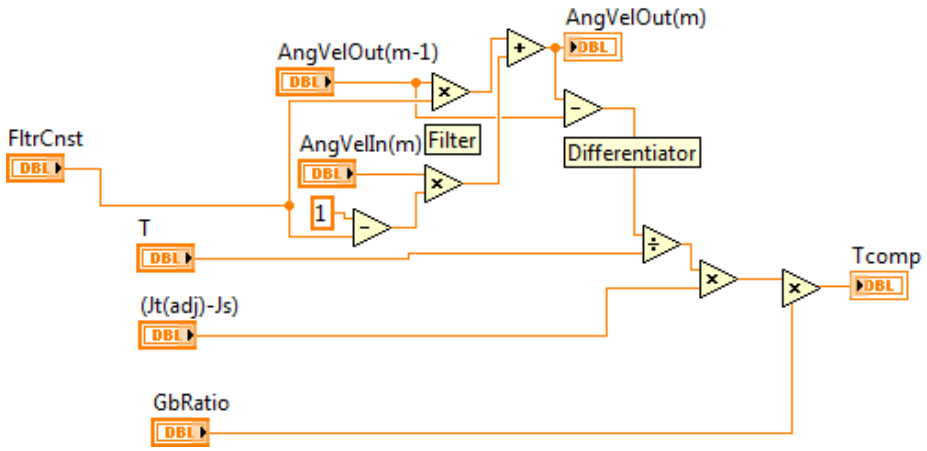

Figure C.10: Code to Generate Compensating Torque

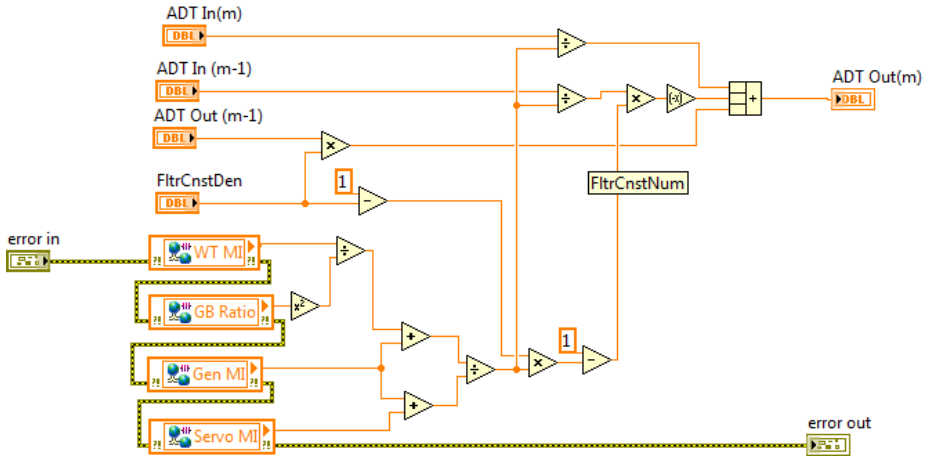

Figure C.11: T_{ad} Pre-Filter

The subVI implementing the pre-filter, discussed in chapter 4, is shown in figure C.11.

Appendix D

Improved Scheme Verification Spreadsheets

The improved inertia compensation scheme relies on the ability to correct z-domain pole positions by means of a system stiffness observer and a pre-filter as discussed in Chapter 4. The algorithm designed to achieve this is based on an s-domain approximation. To confirm accuracy, over the intended range of system stiffnesses and moments of inertia, a set of spreadsheets were created. These calculate percentage error in z-plane pole positioning, with respect to the unit circle for three situations. Figure D.1 shows pole positioning prior to algorithm use. Figure D.2 shows pole positioning after the first iteration and D.3 shows the situation after two iterations.

	Percentage Error in Pole Distance from Unit Circle (No Correction)											
	J'_T (kgm^2)											
k (Nms/Rad)	0.04		0.05		0.06		0.07		0.08		0.09	
0.013	-1.7	1.6	-1.6	1.6	-1.5	1.4	-1.3	1.3	-1.2	1.2	-1.1	1.1
0.025	-3.2	3.1	-3.1	3.0	-2.8	2.7	-2.6	2.5	-2.4	2.3	-2.2	2.1
0.05	-6.6	6.2	-6.2	5.9	-5.7	5.4	-5.2	4.9	-4.8	4.5	-4.4	4.2
0.075	-10.2	9.3	-9.5	8.7	-8.7	8.0	-7.9	7.3	-7.2	6.7	-6.6	6.2
0.1	-14.0	12.3	-12.9	11.4	-11.7	10.5	-10.6	9.6	-9.7	8.8	-8.8	8.1
0.125	-18.0	15.3	-16.4	14.1	-14.8	12.9	-13.4	11.8	-12.1	10.8	-11.1	10.0
0.15	-22.2	18.1	-20.0	16.7	-17.9	15.2	-16.2	13.9	-14.7	12.8	-13.4	11.8
0.175	-26.5	20.9	-23.7	19.1	-21.1	17.5	-19.0	16.0	-17.2	14.7	-15.7	13.6
0.2	-30.9	23.6	-27.4	21.5	-24.4	19.6	-21.9	17.9	-19.8	16.5	-18.0	15.3
0.225	-35.5	26.2	-31.3	23.8	-27.7	21.7	-24.8	19.9	-22.4	18.3	-20.4	16.9
Root >	Low	High	Low	High	Low	High	Low	High	Low	High	Low	High

Figure D.1: Uncorrected Pole Positioning.

	Percentage Error in Pole Distance from Unit Circle (First Correction Iteration)											
	J'_T (kgm^2)											
k (Nms/Rad)	0.04		0.05		0.06		0.07		0.08		0.09	
0.013	-0.1	0.1	-0.1	0.1	-0.1	0.1	-0.1	0.1	0.0	0.0	0.0	0.0
0.025	-0.1	0.1	-0.1	0.1	-0.1	0.1	-0.1	0.1	-0.1	0.1	-0.1	0.1
0.05	0.1	-0.1	0.1	-0.1	0.0	0.0	0.0	0.0	0.0	0.0	0.0	0.0
0.075	0.5	-0.5	0.4	-0.4	0.3	-0.3	0.2	-0.2	0.1	-0.1	0.1	-0.1
0.1	1.3	-1.3	1.0	-1.0	0.7	-0.7	0.5	-0.5	0.4	-0.4	0.3	-0.3
0.125	2.5	-2.6	1.8	-1.9	1.4	-1.4	1.0	-1.0	0.8	-0.8	0.6	-0.6
0.15	4.3	-4.5	3.1	-3.2	2.2	-2.3	1.7	-1.7	1.3	-1.3	1.0	-1.0
0.175	6.7	-7.2	4.6	-4.9	3.4	-3.5	2.5	-2.6	2.0	-2.0	1.5	-1.6
0.2	10.0	-11.1	6.7	-7.1	4.8	-5.0	3.6	-3.7	2.8	-2.8	2.2	-2.2
0.225	14.5	-17.0	9.2	-10.1	6.5	-6.9	4.8	-5.1	3.7	-3.9	2.9	-3.0
Root >	Low	High	Low	High	Low	High	Low	High	Low	High	Low	High

Figure D.2: Pole Positioning after One Iteration.

	Percentage Error in Pole Distance from Unit Circle (Second Correction Iteration)											
	J'_T (kgm^2)											
k (Nms/Rad)	0.04		0.05		0.06		0.07		0.08		0.09	
0.013	-0.1	0.1	-0.1	0.1	-0.1	0.1	-0.1	0.1	-0.1	0.1	-0.1	0.1
0.025	-0.2	0.2	-0.2	0.2	-0.1	0.1	-0.1	0.1	-0.1	0.1	-0.1	0.1
0.05	-0.3	0.3	-0.3	0.3	-0.3	0.3	-0.3	0.3	-0.2	0.2	-0.2	0.2
0.075	-0.5	0.5	-0.5	0.5	-0.4	0.4	-0.4	0.4	-0.4	0.4	-0.3	0.3
0.1	-0.7	0.7	-0.6	0.6	-0.6	0.6	-0.5	0.5	-0.5	0.5	-0.4	0.4
0.125	-0.8	0.8	-0.8	0.7	-0.7	0.7	-0.6	0.6	-0.6	0.6	-0.5	0.5
0.15	-0.8	0.8	-0.8	0.8	-0.8	0.8	-0.7	0.7	-0.7	0.7	-0.6	0.6
0.175	-0.6	0.6	-0.8	0.8	-0.9	0.9	-0.8	0.8	-0.8	0.8	-0.7	0.7
0.2	0.1	-0.1	-0.7	0.7	-0.8	0.8	-0.9	0.9	-0.8	0.8	-0.8	0.8
0.225	1.8	-1.8	-0.2	0.2	-0.7	0.7	-0.9	0.9	-0.9	0.9	-0.9	0.9
Root >	Low	High	Low	High	Low	High	Low	High	Low	High	Low	High

Figure D.3: Pole Positioning after Two Iterations.

Appendix E

Faulty Rotor Mean Torque and Power Results

The test results demonstrating the accuracy of the WTE system mean torque and power outputs for various rotor fault conditions are discussed in the main text but are set out here. These results show the same degree of accuracy as the emulations of healthy rotor configurations.

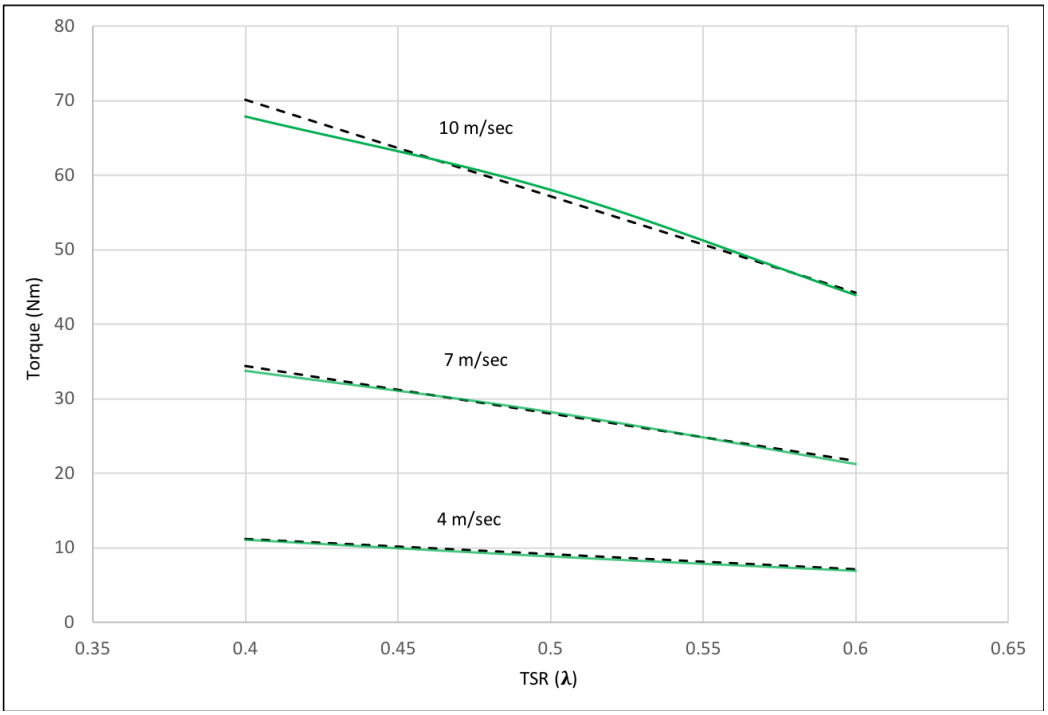

(a) Predicted Torque (Dashed Black Lines) v WTE Torque (Green lines)

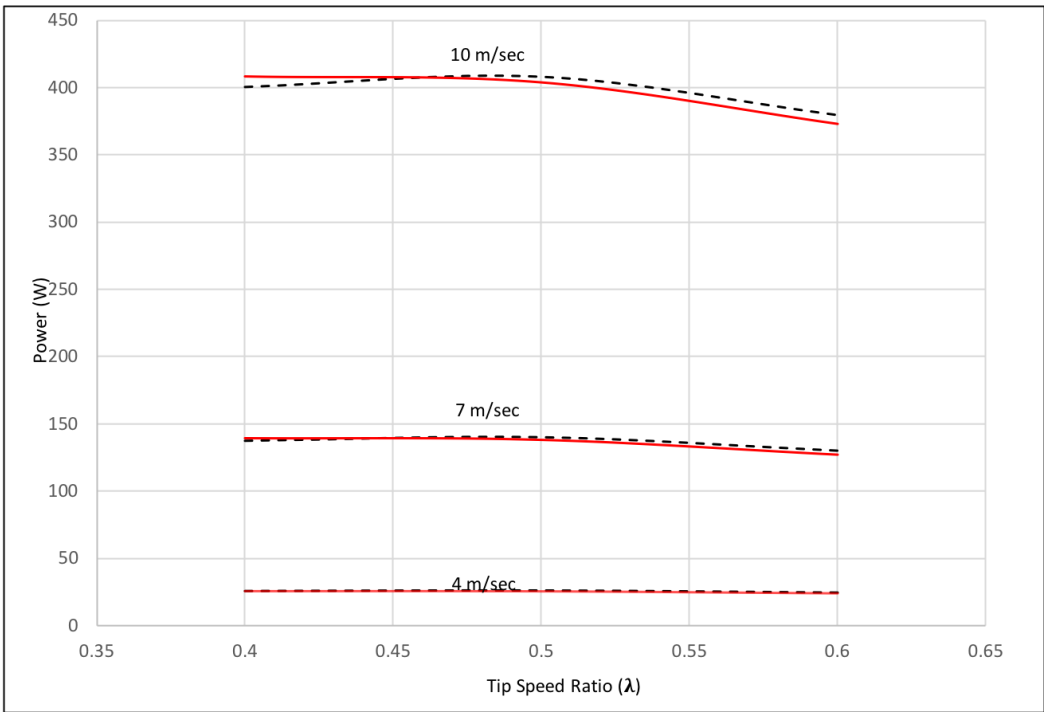

(b) Predicted Power (Dashed Black Lines) v WTE Power (Red lines)

Figure E.1: Comparison of Predicted and Actual Behaviour at Differing Wind Velocities for WT with One Missing Blade ($J_{wt} = 2.02\,kgm^2$)

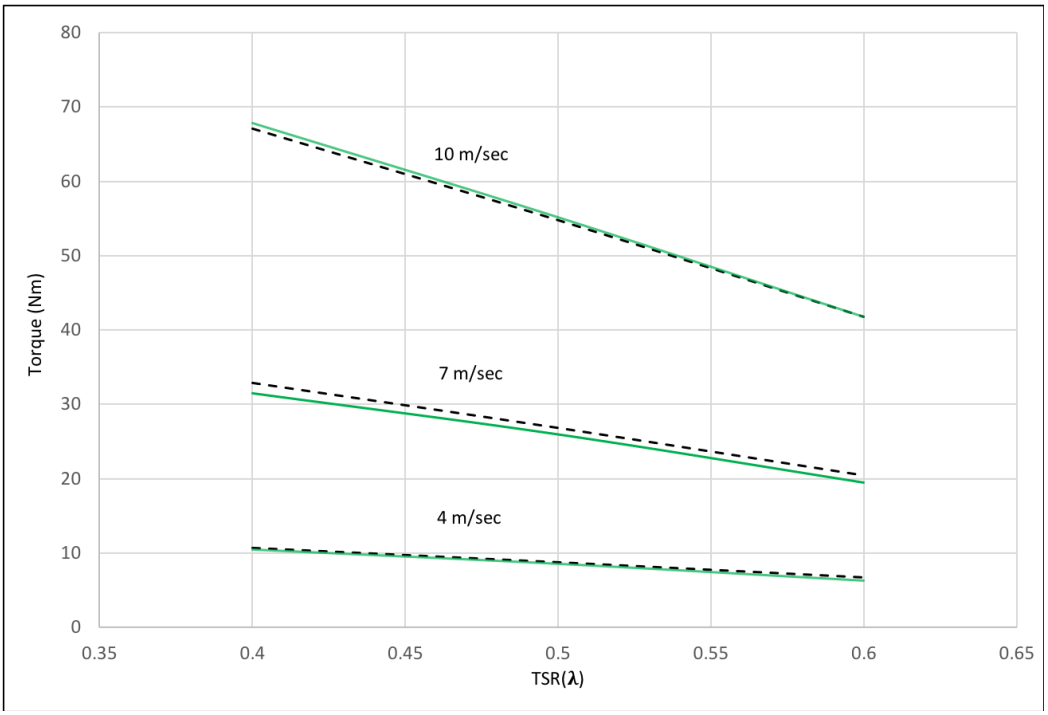

(a) Predicted Torque (Dashed Black Lines) v WTE Torque (Green lines)

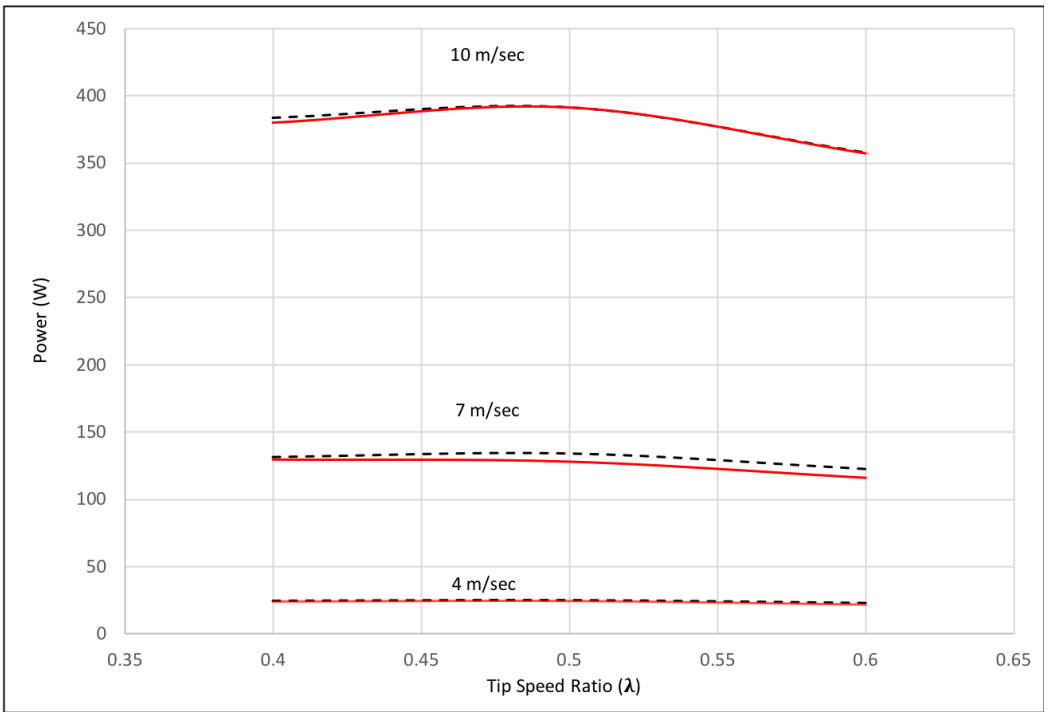

(b) Predicted Power (Dashed Black Lines) v WTE Power (Red lines)

Figure E.2: Comparison of Predicted and Actual Behaviour at Differing Wind Velocities for WT with Two Missing Blades ($J_{wt} = 2.02\,kgm^2$)

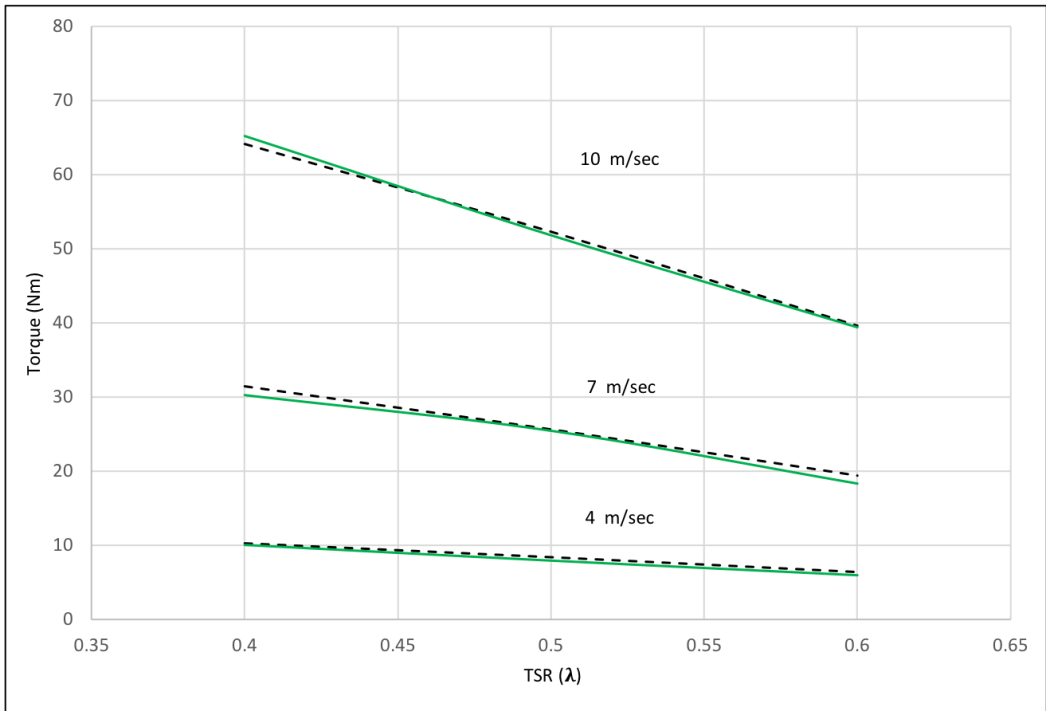

(a) Predicted Torque (Dashed Black Lines) v WTE Torque (Green lines)

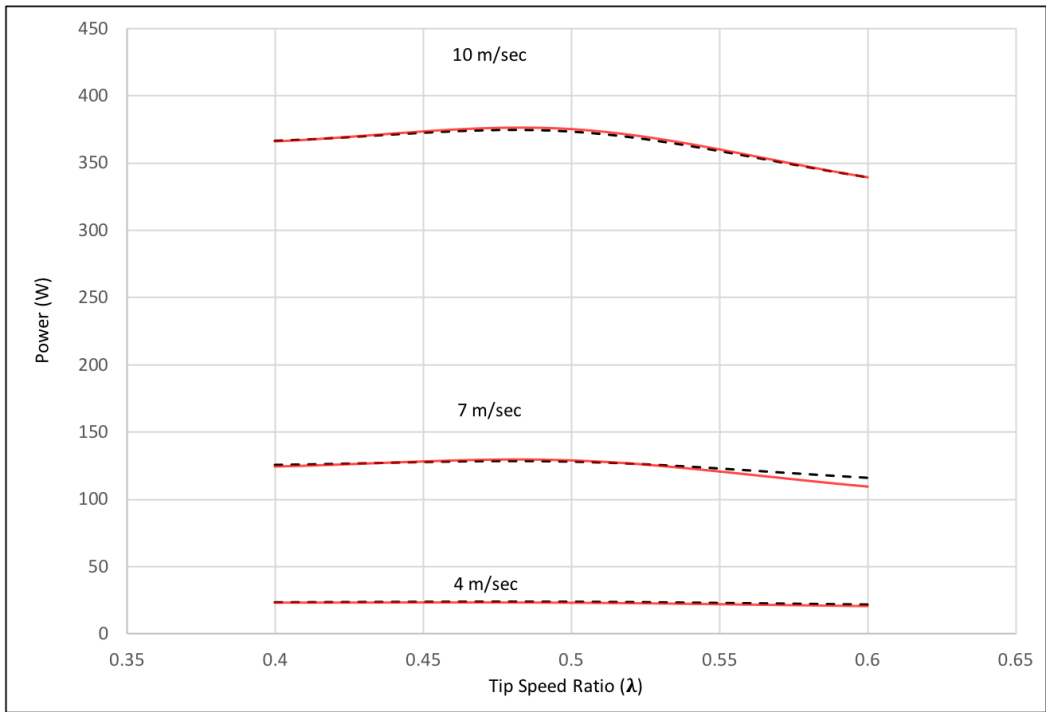

(b) Predicted Power (Dashed Black Lines) v WTE Power (Red lines)

Figure E.3: Comparison of Predicted and Actual Behaviour at Differing Wind Velocities for WT with Three Missing Blades ($J_{wt} = 2.02\,kgm^2$)

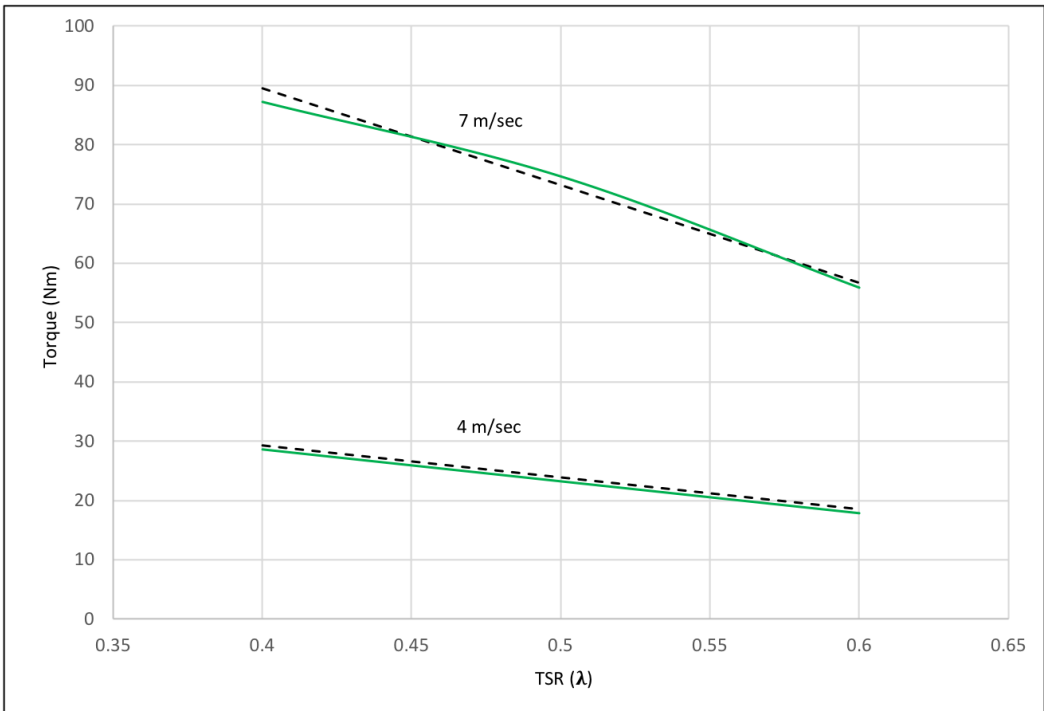

(a) Predicted Torque (Dashed Black Lines) v WTE Torque (Green lines)

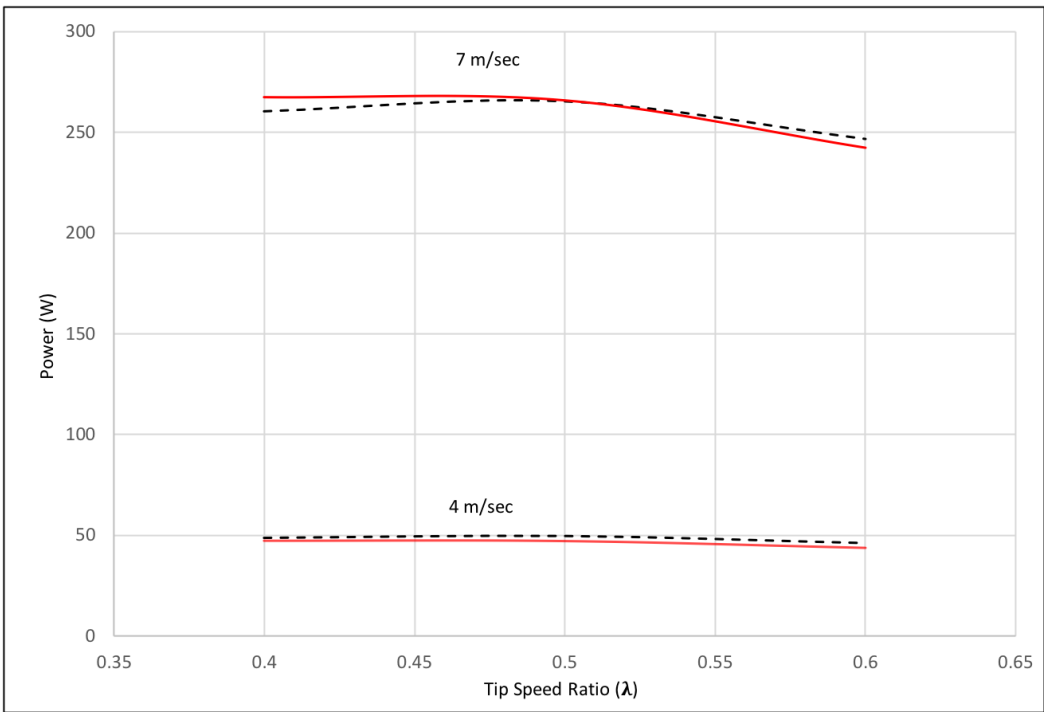

(b) Predicted Power (Dashed Black Lines) v WTE Power (Red lines)

Figure E.4: Comparison of Predicted and Actual Behaviour at Differing Wind Velocities for WT with One Missing Blade ($J_{wt} = 10\,kgm^2$)

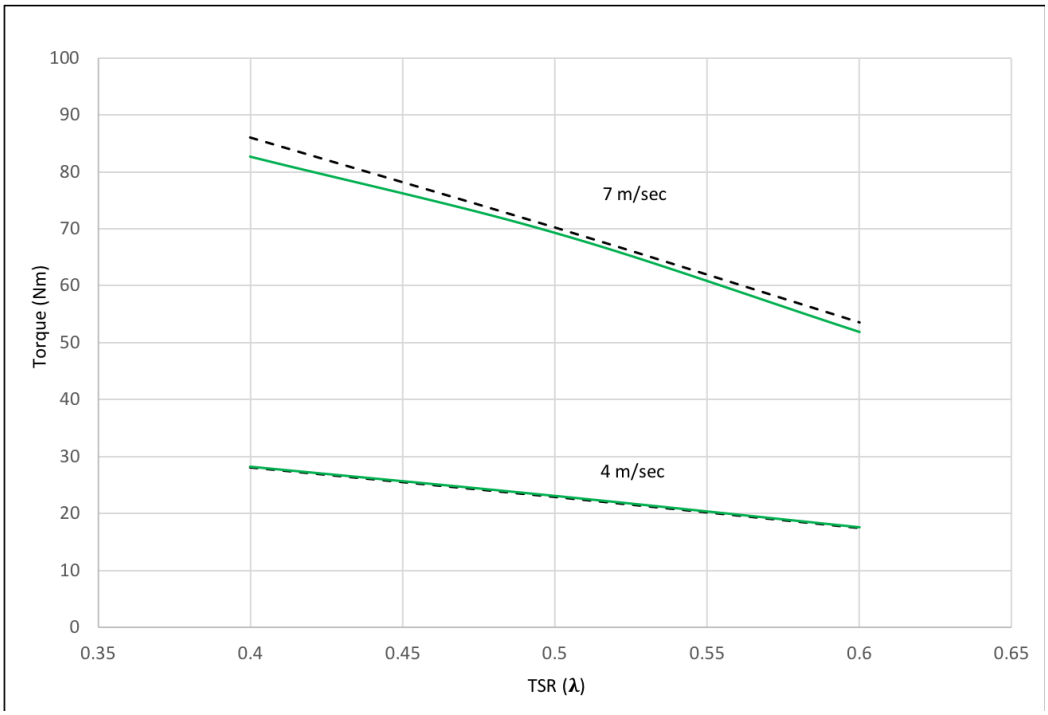

(a) Predicted Torque (Dashed Black Lines) v WTE Torque (Green lines)

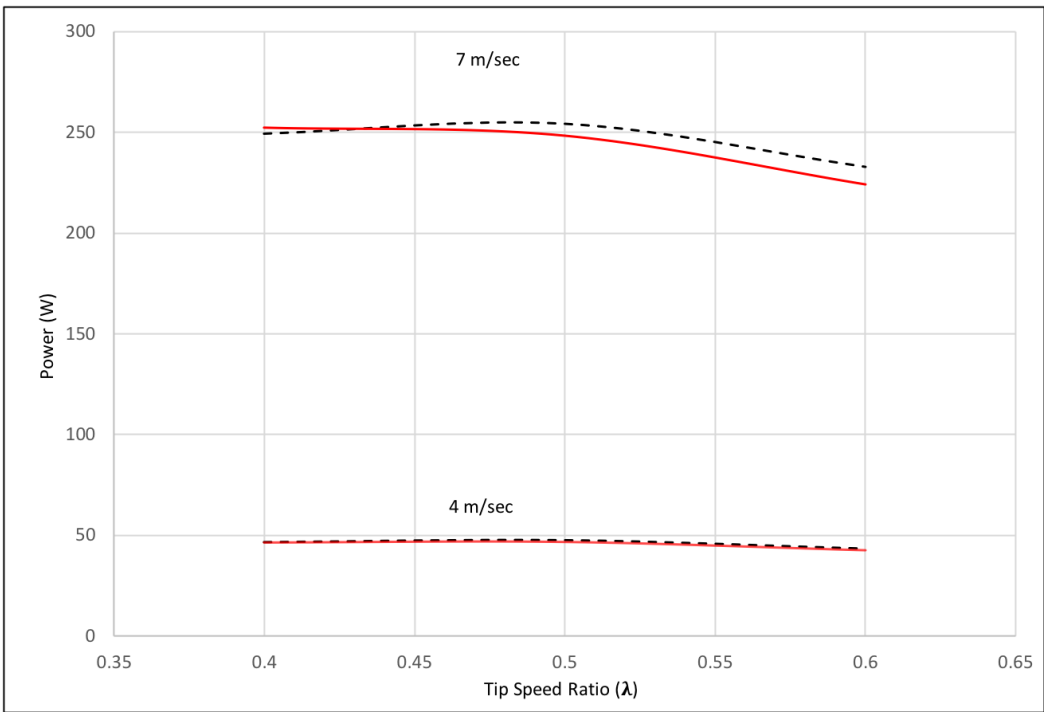

(b) Predicted Power (Dashed Black Lines) v WTE Power (Red lines)

Figure E.5: Comparison of Predicted and Actual Behaviour at Differing Wind Velocities for WT with Two Missing Blades ($J_{wt} = 10\,kgm^2$)

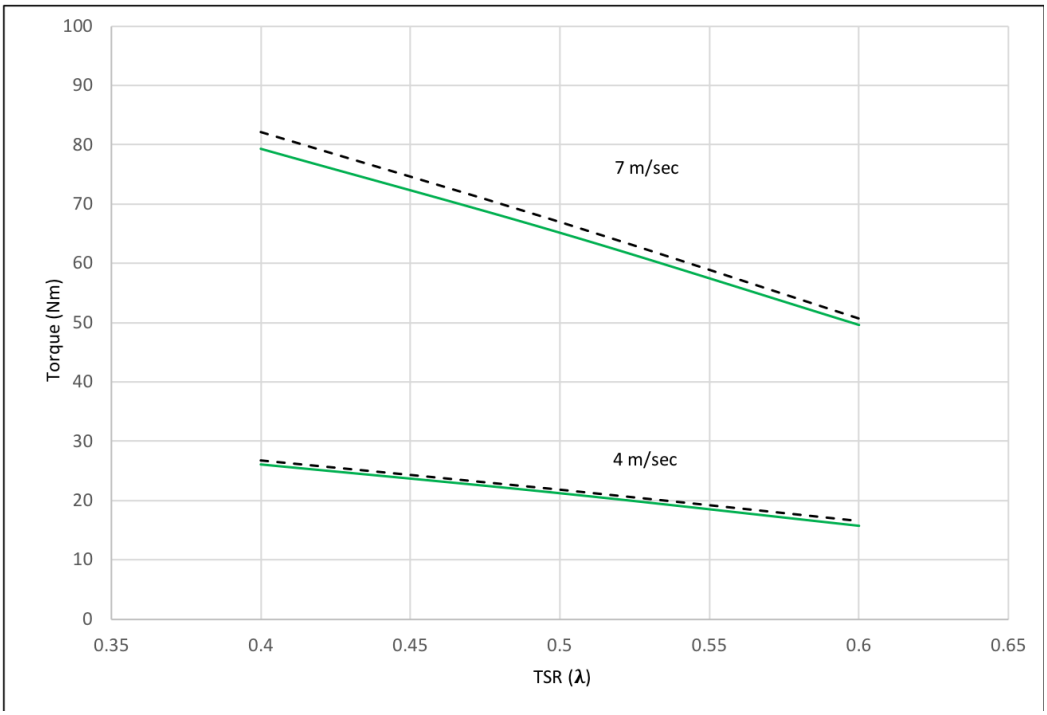

(a) Predicted Torque (Dashed Black Lines) v WTE Torque (Green lines)

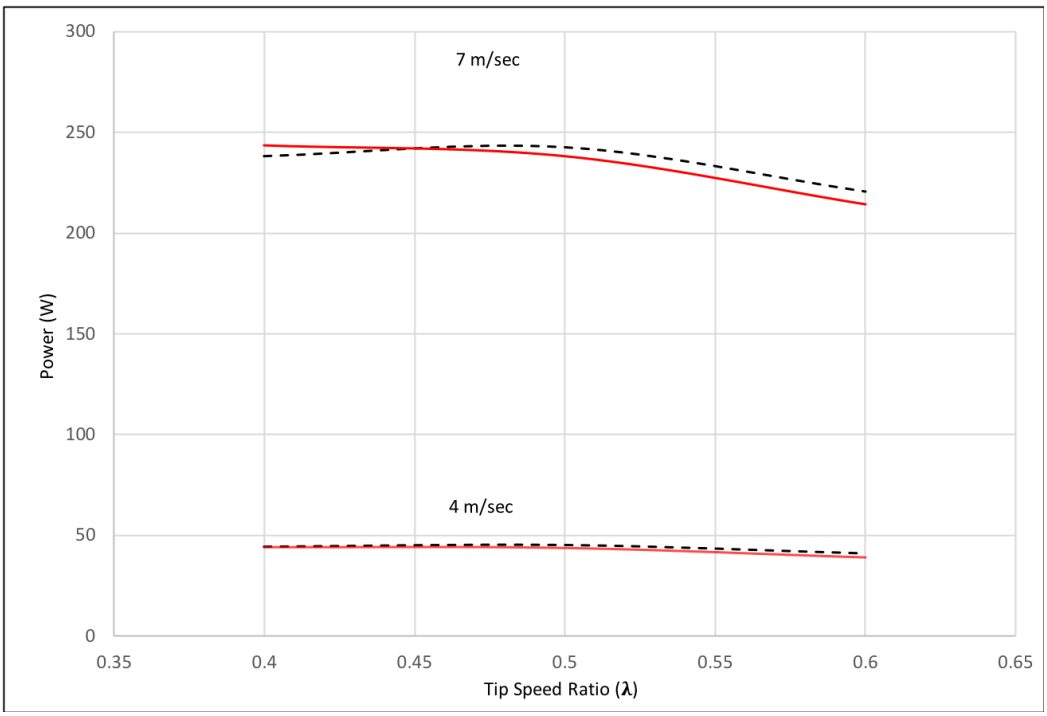

(b) Predicted Power (Dashed Black Lines) v WTE Power (Red lines)

Figure E.6: Comparison of Predicted and Actual Behaviour at Differing Wind Velocities for WT with Three Missing Blades ($J_{wt} = 10\,kgm^2$)

Appendix F

Wind Turbine Emulator Rig

Figure F.1a shows an annotated photograph of the Wind Turbine Emulator Rig developed during this research. Figure F.1b, immediately below it shows, for comparison, a correctly scaled photograph of the VAWT used during the development of the WTE.

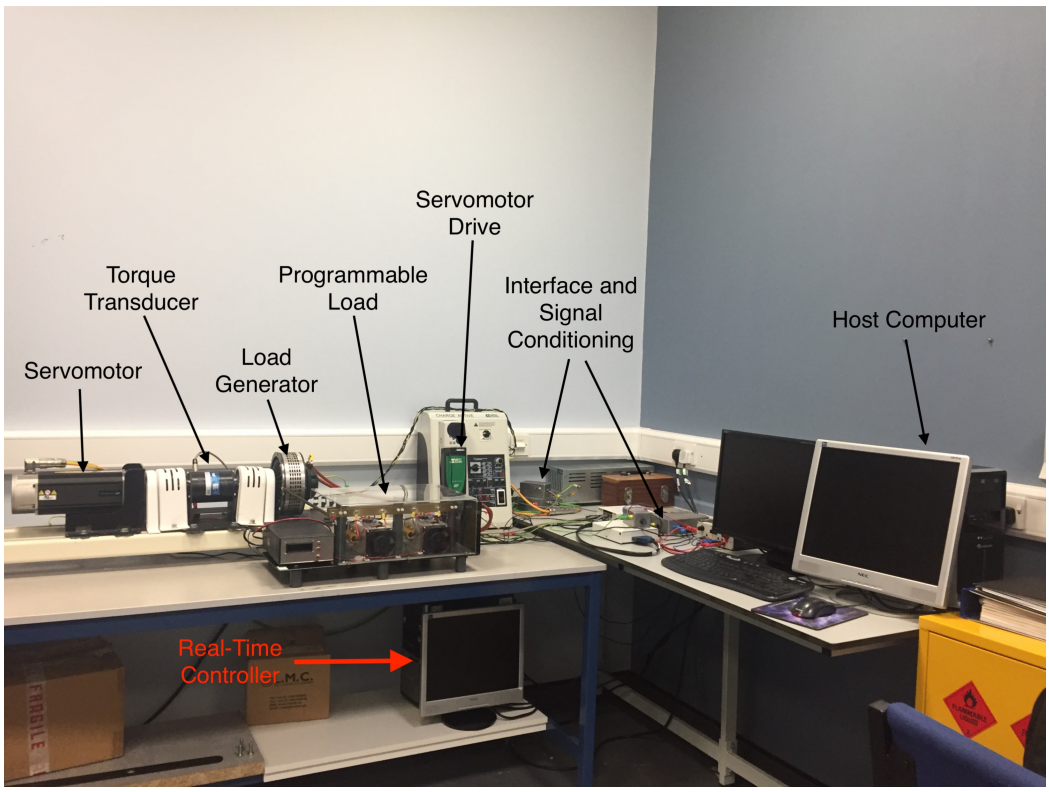

(a) Wind Turbine Emulator Rig

(b) Emulated VAWT

Figure F.1: Comparison of Emulator Rig and VAWT

References

[1] HM Government, *Climate Change Act 2008,* HMSO, 2008, ch. 27.

[2] The European Parliament and the Council of the European Union, *Directive 2009/28/EC on the promotion of renewable energy sources.* 4–2009.

[3] HM Government, *The UK Renewable Energy Strategy,* TSO, 2009, ISBN: 9780101768627.

[4] HM Government, Dept for BEIS, "Energy Trends: December 2017," HMSO, 12–2017, p. 63.

[5] Renewable Energy Foundation. (Nov. 2016). Renewable Energy Totals, [Online]. Available: http://www.ref.org.uk/energy-data (visited on 10/10/2017).

[6] HM Government, Dept for BEIS, "Energy Trends: September 2017," HMSO, 9–2017, p. 62.

[7] WindEurope. (2018). Wind in power 2017: Annual combined onshore and offshore wind energy statistics. I Pineda, Ed., WindEurope asbl/vzw, [Online]. Available: https://windeurope.org/wp-content/uploads/files/about-wind/statistics/WindEurope-Annual-Statistics-2017.pdf.

[8] HM Government, *Energy Act 2008,* HMSO, 2008, ch. 32.

[9] RenewableUK, "Small and Medium Wind UK Market Report," *renewableUK*, Mar. 2015. [Online]. Available: http://c.ymcdn.com/sites/www.renewableuk.com/resource/resmgr/publications/reports/smallmediumwindukmarket.pdf (visited on 12/02/2017).

[10] RenewableUK, "Small and Medium Wind Strategy," *renewableUK*, Nov. 2014. [Online]. Available: https://cdn.ymaws.com/www.renewableuk.com/resource/resmgr/Docs/small_medium_wind_strategy_r.pdf (visited on 08/05/2016).

[11] Energy Saving Trust. (2009). Location, location, location: Domestic small-scale wind field trial report, [Online]. Available: http://www.energysavingtrust.org.uk/sites/default/files/reports/Location_Location_Location_field_trial_small-scale_wind_report%20%282%29.pdf (visited on 09/12/2017).

[12] HM Government. (2016). Quarterly and Annual Load Factors, Dept for BEIS, [Online]. Available: https://www.gov.uk/government/publications/quarterly-and-annual-load-factors (visited on 01/15/2018).

[13] R. Fowler, "Electric dreams: The Future for EVs," National Grid UK, Online Article, 2018. [Online]. Available: https://www.nationalgrid.com/uk/articles/electric-dreams-future-evs (visited on 02/30/2018).

[14] C. Barteczko-Hibbert, "After Diversity Maximum Demand (ADMD) Report," Customer-Led Network Revolution, Report CLNR-L217, Feb. 23, 2015. [Online]. Available: http://www.networkrevolution.co.uk/wp-content/uploads/2015/02/After-Diversity-Maximum-Demand-Insight-Report.pdf (visited on 10/10/2017).

[15] Nissan. (2017). Nissan Leaf: Range and Charging, [Online]. Available: https://www.nissan.co.uk/vehicles/new-vehicles/leaf/charging-range.html#findacharger? (visited on 10/10/2017).

[16] F. Toja-Silva, A.Colmenar-Santos, and M. Castro-Gil, "Urban wind energy exploitation systems: Behaviour under multidirectional flow conditions-Opportunities and challenges," *Renewable and Sustainable Energy Reviews*, vol. 24, pp. 364–378, 2013.

[17] S. Eriksson, H. Bernhoff, and M. Leijon, "Evaluation of different turbine concepts for wind power," *Renewable and Sustainable Energy Reviews*, vol. 12, pp. 1418–1434, 2008.

[18] G Colley, "Design, Operation and Diagnostics of a Vertical Axis Wind Turbine," PhD, The University of Huddersfield, 2012, ch. 2, p. 30.

[19] B. Shahizare, N. Nik-Ghazali, W. Chong, S. Tabatabaeikia, N. Izadyar, and A. Esmaeilzadeh, "Novel investigation of the different Omni-direction guide-vane angles effects on the urban vertical axis wind turbine output power via three-dimensional numerical simulation," *Energy Conversion and Management*, vol. 1117, pp. 206–217, 2016.

[20] S. McTavish, D. Feszty, and T. Sancar, "Steady and rotating computational fluid dynamics simulations of a novel vertical axis wind turbine for small-scale power generation," *Renewable Energy*, vol. 41, pp. 171–179, 2012.

[21] A. Rezaeiha, H. Montazeri, and B. Blocken, "Towards accurate CFD simulations of vertical axis wind turbines at different tip speed ratios and solidities: Guidelines for azimuthal increment, domain size and convergence," *Energy Conversion and Management*, vol. 156, pp. 301–316, 2018.

[22] M. Elkhoury, T. Kiwata, and E. Aoun, "Experimental and numerical investigation of three-dimensional vertical-axis wind turbine with variable-pitch," *Journal of Wind Engineering and Industrial Aerodynamics*, vol. 139, pp. 111–123, 2015.

[23] A. Bianchini, F. Balduzzi, P. Bachant, G. Ferrara, and L. Ferrari, "Effectiveness of two-dimensional CFD simulations for Darrieus VAWTs: a combined numerical and experimental assessment," *Energy Conversion and Management*, vol. 136, pp. 318–328, 2017.

[24] I. Abohela, N. Hamza, and S. Dudek, "Effect of roof shape, wind direction, building height and urban configuration on the energy yield and positioning of roof mounted wind turbines," *Renewable Energy*, vol. 50, pp. 1106–1118, 2013.

[25] A. Tabrizi, J. Whale, T. Lyons, and T. Urmee, "Performance and safety of rooftop wind turbines: Use of CFD to gain insight into inflow conditions," *Renewable Energy*, vol. 67, pp. 242–251, 2014.

[26] P. Larin, M. Paraschivoiu, and C. Aygun, "CFD based synergistic analysis of wind turbines for roof mounted integration," *Journal of Wind Engineering and Industrial Aerodynamics*, vol. 156, pp. 1–13, 2016.

[27] D. Wekesa, C. Wang, Y. Wei, and J. Kamau, "A numerical analysis of unsteady inflow for site specific vertical axis wind turbine: A case study for Marsabit and Garissa in Kenya," *Renewable Energy*, vol. 76, pp. 648–661, 2015.

[28] A. Betz, *Wind-Energie und ihre Ausnutzung durch Windmühlen*. Vandenhoeck und Ruprecht, Göttingen, 1926.

[29] S. Heier, *Grid Integration of Wind Energy Conversion Systems*. John Wiley and Sons, Ltd, 2006, ch. 2, ISBN: 9780470868997.

[30] J. Manwell, J. McGowan, and A. Rogers, *Wind Energy Explained: Theory, Design and Application*. John Wiley and Sons, Ltd, 2009, ch. 3.

[31] B. Newman, "Multiple actuator-disc theory for wind turbines," *Journal of Wind Engineering and Industrial Aerodynamics*, vol. 24, pp. 215–225, Oct. 1986.

[32] H. A. Madsen, U. S. Paulsen, and L Vitae, "Analysis of vawt aerodynamics and design using the actuator cylinder flow model," *Journal of Physics: Conference Series*, vol. 555, no. 1, p. 012 065, 2014.

[33] F. Thőnnißen, M. Marnett, B. Roidl, and W. Schrőder, "A numerical analysis to evaluate Betz's Law for vertical axis wind turbines," *Journal of Physics: Conference Series*, vol. 753, 2016. DOI: 10.1088/1742-6596/753/2/022056.

[34] M. Casini, "Small Vertical Axis Wind Turbines for Energy Efficiency of Buildings," *Journal of Clean Energy Technologies 4(1)*, p. 58, 2016.

[35] M. Neammanee, S. Sirisumrannukal, and S. Chatratana, "Development of a Wind Turbine Simulator for Wind Generator Testing," *International Energy Journal 8*, pp. 21–28, 2007.

[36] M. Chinchilla, S. Arnaltes, and L. Rodriguez-Amenedo, "Laboratory Set-Up for Wind Turbine Emulation," presented at the IEEE International Conference on Industrial Technology, IEEE, vol. 1, Hammamet Tunisia, Dec. 8, 2004, pp. 553–557.

[37] S. Drouilhet, "WROC Wind Resource Assessment August 2003 to July 2004," Sustainable Automation LLC, Report, Jul. 1, 2005. [Online]. Available: http://renewables.morris.umn.edu/wind/documents/WindResourceAssessmentFinalReport.pdf (visited on 03/28/2018).

[38] D. Dolan and P. Lehn, "Simulation Model of Wind Turbine 3p Torque Oscillations due to Wind Shear and Tower Shadow," *IEEE Transactions on Energy Conversion*, vol. 21, no. 3, pp. 717–724, Sep. 2006.

[39] A. Causo, G. Dall'Aglio, and A. Sala, "Power Converter for Vertical Axis Micro-Wind Generators," presented at the International Conference on Clean Electrical Power, ICCEP, Ischia, Italy, Jun. 14, 2011. DOI: 10.1109/ICCEP.2011.6036303.

[40] A. Rezaeiha, H. Montazeri, and B. Blocken, "Characterization of aerodynamic performance of vertical axis wind turbines: Impact of operational parameters," *Energy Conversion and Management*, vol. 169, pp. 45–47, 2018.

[41] G. Darrieus, "Turbine Having its Rotating Shaft Transverse to the Flow of the Current," pat. US 1,853,018, Dec. 8, 1931.

[42] L. Battisti, A. Brighenti, E. Benini, and M. R. Castelli, "Analysis of Different Blade Architectures on Small VAWT Performance," *Journal of Physics: Conference Series*, vol. 753, no. 6, p. 062 009, 2016.

[43] S. Brusca, R. Lanzafame, and M. Messina, "Design of a vertical-axis wind turbine: How the aspect ratio affects the turbine's performance," *International Journal of Energy and Environmental Engineering*, vol. 5, no. 4, pp. 333–340, 2014, ISSN: 2251-6832.

[44] R. Dominy, P. Lunt, A. Bickerdyke, and J Dominy, "Self-starting capability of a Darrieus turbine," *Proceedings of the I MECH E part A: Journal of Power and Energy*, vol. 221, no. 1, pp. 111–120, 2007.

[45] S. Joo, H. Choi, and J. Lee, "Aerodynamic characteristics of a two-bladed H-Darrieus at various solidities and rotating speeds," *Energy*, vol. 90, no. 1, pp. 439–451, Jul. 2015.

[46] S. J. Savonius, "Rotor Adapted to be Driven by Wind or Flowing Water," pat. US 1,697,574, Jan. 1, 1929.

[47] B. Blackwell, R. Sheldahl, and L. Feltz, "Wind tunnel Performance Data for Two- and Three-Bucket Savonius Rotors," *Journal of Energy*, vol. 2, no. 3, pp. 160–164, 1978, ISSN: 0146-0412.

[48] K. Park, T. Asim, and R. Mishra, "Effect of Blade Faults on the Performance Characteristics of a Vertical Axis Wind Turbine," presented at the 26th International Congress of Condition Monitoring and Diagnostic Engineering Management, COMADEM, Helsinki, Finland, Jun. 11, 2013.

[49] K. Park, T. Asim, and R. Mishra, "Effect of Blade Angles of a Vertical Axis Wind Turbine on its Performance Output," *International Journal of COMADEM*, pp. 3–10, 2015, ISSN: 1363-7681.

[50] S. Seung-Ho, O. Jeong-Hun, and G. Venkataramanan, "Emulation of Output Characteristics of Rotor Blades Using a Hardware-In-Loop Wind Turbine Simulator," presented at the Twentieth Annual IEEE Applied Power Electronics Conference and Exposition, IEEE, vol. 3, Austin Texas USA, Mar. 6, 2005, pp. 1791–1796.

[51] M. Monfared, H. Kojabadi, and H. Rastegar, "Static and dynamic wind turbine simulator using a converter controlled dc motor," *Renewable Energy*, vol. 33, pp. 906–913, 2008.

[52] B. Gong and D. Xu, "Real Time Simulator for Wind Energy Conversion System," presented at the Power Electronics Specialists Conference, IEEE, Rhodes, Greece, Jun. 8, 2008. DOI: 10.1109/PESC.2008.4592078.

[53] H. Guo, B.Zhou, L. J, F. Cheng, and L Zhang, "Real-Time Simulation of BLDC-based Wind Turbine Emulator Using RT-LAB," presented at the International Conference on Electrical Machines and Systems, IEEE, Tokyo, Japan, Nov. 15, 2009. DOI: 10.1109/ICEMS.2009.5382776.

[54] A. Luiz, J. Lhuillier, A. Mukherjee, and M. Khokhar, "A Wind Turbine Emulator that Represents the Dynamics of the Wind Turbine Rotor and Drive Train," presented at the Power Electronics Specialists Conference, IEEE, Recife, Brazil, Jun. 16, 2005. DOI: 10.1109/PESC.2005.1581921.

[55] D. Dolan and P. Lehn, "Real-Time Wind Turbine Emulator Suitable for Power Quality and Dynamic Control Studies," presented at the International Conference on Power Systems Transients, Montreal, Canada, Jun. 19, 2005.

[56] U.Sancar, A. Onol, A.Ohnat, and S. Yesilyurt, "Hardware-in-the-Loop Simulations and Control design for a Small Vertical Axis Wind Turbine," presented at the XXV International Conference on Information, Communication and Automation Technologies, ICAT, Sarajevo, Bosnia and Herzegovina, Oct. 29, 2015. DOI: 10.1109/ICAT.2015.7340497.

[57] A. Alaimo, A. Esposito, A. Messineo, C. Orlando, and D. Tumino, "3D CFD Analysis of a Vertical Axis Wind Turbine," *Energies*, vol. 8, pp. 3013–3033, 2015. DOI: 10.3390/en8043013.

[58] F. Balduzzi, A. Bianchini, R.Maleci, and G Ferrara, "Critical issues in the CFD simulation of Darrieus wind turbines," *Renewable Energy*, vol. 85, pp. 419–435, 2016.

[59] M. Bhargav, V. Kishore, and V. Laxman, "Influence of fluctuating wind conditions on vertical axis wind turbine using a three dimensional CFD model," *Journal of Wind Engineering and Industrial Aerodynamics*, vol. 158, pp. 98–108, 2016.

[60] P. Tavner, L. Ran, J. Penman, and H. Sedding, *Condition Monitoring of Rotating Electrical Machines*. IET, 2008, ch. 1, pp. 4–5, ISBN: 9780863417412.

[61] B. S. Dhillon, "Human error in maintenance: An investigative study for the factories of the future," *IOP Conference Series: Materials Science and Engineering*, vol. 65, no. 1, p. 012 031, 2014.

[62] R. B. Randall, *Vibration-based Condition Monitoring*. Wiley, 2011, ch. 1, pp. 2–3, ISBN: 9780470747858.

[63] P. Tavner, L. Ran, J. Penman, and H. Sedding, *Condition Monitoring of Rotating Electrical Machines*. IET, 2008, ch. 4, pp. 79–80, ISBN: 9780863417412.

[64] W. Qiao and D. Lu, "A Survey on Wind Turbine Condition Monitoring and Fault Diagnosis-Part 11: Signals and Signal Processing Methods," *IEEE Transaction on Industrial Electronics*, vol. 62, no. 10, pp. 6546–6557, 2015.

[65] W. Yang, P.Tavner, C. Crabtree, Y.Feng, and Y.Qiu, "Wind turbine condition monitoring: Technical and commercial challenges.," *Wind Energy*, vol. 17, no. 5, pp. 673–693, 2014.

[66] B. Lu, Y. Li, X.Wu, and Z.Yang, "A Review of Recent Advances in Wind Turbine Condition Monitoring and Fault Diagnosis," presented at the IEEE Power Electronics and Machines in Wind Applications, IEEE, Lincoln, USA, Jun. 24, 2009. DOI: 10.1109/PEMWA.2009.5208325.

[67] P. Tchakoua, R. Wamkeue, M. Ouhrouche, F. Slaoui-Hasnaoui, T. A. Tameghe, and G. Ekemb, "Wind turbine condition monitoring: State-of-the-art review, new trends, and future challenges," *Energies*, vol. 7, no. 4, pp. 2595–2630, 2014, ISSN: 1996-1073.

[68] F. Marquez, A.Tobias, J. Perez, and M. Papaelias, "Condition Monitoring of Wind Turbines: Techniques and Methods," *Renewable Energy*, vol. 46, pp. 160–178, 2012.

[69] E. Al-Ahmar, M. Benbouzid, and S. Turrie, "Wind Energy Conversion Systems Fault Diagnosis Using Wavelet Analysis," *International Review of Electrical Engineering*, vol. 3, no. 4, pp. 646–652, 2008.

[70] K. Park, T. Asim, R. Mishra, and S. Pradhan, "Condition Based Monitoring of Vertical Axis Wind Turbines using Computational Fluid Dynamics," presented at the Proceedings of the Thirty Ninth Conference on Fluid Mechanics and Fluid Power, SVNIT, Surat, Gujarat, India, Dec. 13, 2012.

[71] W. Li, M. Yin, Z. Chen, and Y. Zou, "Inertia Compensation Scheme for Wind Turbine Simulator Based Deviation Mitigation," *Journal of Modern Power Systems and Clean Energy 5(2)*, pp. 228–238, 2017.

[72] *NI DIAdem, Data Mining, Analysis and Report Generation.* 373082M-01, NATIONAL INSTRUMENTS, 7–2014.

[73] *Technical Data Unimotor fm and hd, High Performance AC brushless servo motors.* 0702-0007-04, EMERSON Industrial Automation, 3–2011.

[74] *DAQ M Series, M Series User Manual.* 371022K-01, NATIONAL INSTRUMENTS, 7–2008.

[75] *Advanced User Guide Unidrive SP, Universal Variable Speed AC Drive for induction and servo motors.* 0471-0002-09, EMERSON Industrial Automation, 6–2009.

[76] Lynch Motor Company. (Nov. 2015). Datasheet Motors LEM-200, LMC Ltd, [Online]. Available: http://lynchmotors.co.uk/pdfs/lmc-lem-200.pdf (visited on 08/03/2015).

[77] IXYS Corporation, *PolarHV HiPerFET Power MOSFET, IXFN 100N50P*, Datasheet, version DS99497E(01/06), 2006.

[78] A. Sattar and V. Tsukanov. (2006). Linear Power MOSFETS Basic and Applications, IXYS Corporation, [Online]. Available: http://www.ixys.com/Documents/AppNotes/IXAN0068.pdf (visited on 08/05/2016).

[79] *Power Supply HMP Serie User Manual*, HAMEG Instruments GmbH, 4–2014.

[80] Siliconix. (1997). FETs as Voltage Controlled Resistors, Siliconix, [Online]. Available: https://www.vishay.com/docs/70598/70598.pdf (visited on 04/03/2017).